



**HAL**  
open science

# Plasmonic Nanostructures for Enhanced Raman Spectroscopy Applications

Guili Zhao

► **To cite this version:**

Guili Zhao. Plasmonic Nanostructures for Enhanced Raman Spectroscopy Applications. Material chemistry. Institut Polytechnique de Paris, 2022. English. NNT : 2022IPPAX102 . tel-04416283

**HAL Id: tel-04416283**

**<https://theses.hal.science/tel-04416283>**

Submitted on 25 Jan 2024

**HAL** is a multi-disciplinary open access archive for the deposit and dissemination of scientific research documents, whether they are published or not. The documents may come from teaching and research institutions in France or abroad, or from public or private research centers.

L'archive ouverte pluridisciplinaire **HAL**, est destinée au dépôt et à la diffusion de documents scientifiques de niveau recherche, publiés ou non, émanant des établissements d'enseignement et de recherche français ou étrangers, des laboratoires publics ou privés.

# Plasmonic Nanostructures for Enhanced Raman Spectroscopy Applications

Thèse de doctorat de l'Institut Polytechnique de Paris  
préparée à l'École Polytechnique

École doctorale n°626 Ecole Doctorale de l'Institut Polytechnique de  
Paris (ED IP Paris)

Spécialité de doctorat: Chimie

Thèse présentée et soutenue à Palaiseau, le 27 Octobre 2022, par

**Guili ZHAO**  
贵丽 赵

Composition du Jury :

Marc Lamy de la Chapelle Professor, IMMM (– Institut des Molécules et Matériaux du Mans)	Président
Nathalie Lidgi-Guigui Assistant Professor, LSPM (– Université Sorbonne Paris Nord)	Rapporteur
Carolina Vericat Assistant Professor, INIFTA (– National University of La Plata)	Rapporteur
Robert Lazenby Assistant Professor, Department of Chemistry & Biochemistry (– Florida State University)	Examineur
Aleix Güell Professeur Charge de Cours, LPICM (– École Polytechnique)	Directeur de thèse
Razvigor Ossikovski Professor, LPICM (– École Polytechnique)	Co-Directeur de thèse
Jongwook Kim Assistant Professor, LPMC (– École Polytechnique)	Invité



To my dear family and the time I spent in France.

A ma chère famille et au temps que j'ai passé en France.

致我亲爱的家人和我在法国度过的时光。



# Abstract

Gold nanostructures have drawn considerable attention in recent decades due to their outstanding properties arising from the localized surface plasmonic resonances, which are the coherent oscillations of free electrons confined in nanostructures. Under the illumination of incoming light, they exhibit large absorption and scattering cross-sections and large near-field enhancement. More attractively, these extraordinary properties are strongly correlated with the size, morphology, and composition of the nanostructures as well as the dielectric function of the medium surrounding them, which enables gold nanocrystals to be applied in a wide range of fields, such as plasmonic sensing and Raman spectroscopy.

This thesis is an effort for expanding the use of gold nanostructures in analytical sciences in general and in the field of scanning probe microscopy (SPM) in particular, developing a facile and fast method to prepare nanometric gold trisoctahedrons as well as creating new plasmonic probes to combine Raman spectroscopy with scanning ion conductance microscopy (SICM).

The investigations on the preparation of gold trisoctahedrons with high-index facets and their plasmonic performances are presented, describing a method that highlights the high control achieved over the high uniformity of the products and the properties of the final nanoparticles. With the ability to tune the size of gold trisoctahedrons, it is possible to tailor their dipolar plasmon resonance wavelength ranging from visible to near-infrared region. Furthermore, the exposed facets of the gold trisoctahedrons can be tuned by growing the nanostructures at different temperatures. Moreover, the obtained gold nanostructures with well-defined tips and edges were assessed for analytical applications exhibiting high plasmonic sensitivities and excellent surface-enhanced Raman scattering (SERS) performance.

Combing plasmonic nanostructures with SICM probes is an interesting approach to bestow SPM techniques with additional SERS analytical possibilities. Towards this goal, the preparation and characterization of pipettes decorated with gold nanoparticles are presented, employing bifunctional molecules to anchor gold nanostructures on the outer surface of the nanopipettes (including borosilicate and quartz) in a very robust fashion. A set of different gold nanostructures, namely nanorods, nanospheres, trisoctahedrons, and nanobipyramids, have been used to

produce SERS active SICM nanopipettes (SERS-SICM probes). The capabilities of the SERS-SICM probes are demonstrated by being used in experiments of imaging and penetrating living cells.

Finally, the preparation of SPM probes for enhanced Raman spectroscopy is taken to the limit by fixing one single nanoparticle at the tip end of an SICM nanopipette. This design has the potential to be used in tip-enhanced Raman scattering (TERS) in liquids, with evident applicability in biology fields, such as living cells. Two different methods of preparing TERS active SICM nanopipettes (TERS-SICM probes) are presented, employing strategies of in-situ synthesis as well as post-functionalization of the nanopipettes. The probes are assessed based on their abilities for SICM imaging.

# Résumé

Les nanostructures d'or ont attiré une attention considérable au cours des dernières décennies en raison de leurs propriétés exceptionnelles résultant des résonances plasmoniques de surface localisées, que sont les modes d'oscillation cohérente d'électrons libres confinés dans des nanostructures. Sous l'effet de la lumière incidente, elles présentent de grandes sections efficaces d'absorption et de diffusion, de même qu'une forte exaltation du champ proche. Plus attrayant, ces propriétés extraordinaires sont fortement corrélées à la taille, à la morphologie et à la composition des nanostructures ainsi, qu'à la fonction diélectrique du milieu qui les entoure, ce qui permet aux nanocristaux d'or d'être appliqués dans un large éventail de domaines tels que la détection plasmonique et la spectroscopie Raman.

Cette thèse constitue un effort pour étendre l'utilisation des nanostructures d'or dans les techniques d'analyse en général et dans le domaine de la microscopie à sonde locale ou microscopie en champ proche (SPM) en particulier, en développant une méthode simple et rapide de fabrication de trioctaèdres d'or nanométriques, ainsi qu'en créant de nouvelles sondes plasmoniques permettant de combiner la spectroscopie Raman avec la microscopie à conductance ionique (SICM).

Les recherches sur la fabrication de trioctaèdres d'or à facettes à haut indice et sur leurs performances plasmoniques sont présentées, décrivant une méthode qui met en évidence la bonne maîtrise obtenue sur la grande uniformité des produits et les propriétés des nanoparticule finales. Avec la possibilité d'ajuster la taille des trioctaèdres d'or, il est possible d'adapter leur longueur d'onde de résonance plasmonique dipolaire allant du visible au proche infrarouge. De plus, les facettes exposées des trioctaèdres d'or peuvent être ajustées en faisant croître les nanostructures à différentes températures. Enfin, les nanostructures d'or obtenues avec des pointes et des bords bien définis ont été évaluées pour des applications analytiques présentant des sensibilités plasmoniques élevées et d'excellentes performances de diffusion Raman exaltée de surface (DRES) ou SERS (en anglais).

Combiner des nanostructures plasmoniques avec des sondes SICM est une approche intéressante pour conférer aux techniques SPM des capacités SERS supplémentaires. Dans ce but, la préparation et la caractérisation de pipettes décorées avec des nanoparticules d'or sont présentées, en utilisant des molécules

bifonctionnelles pour ancrer des nanostructures d'or sur la surface externe des nanopipettes (en borosilicate et en quartz) de manière très robuste. Un ensemble de différentes nanostructures d'or, à savoir des nanotiges, des nanosphères, des trioctaèdres et des nanobipyramides, a été utilisé pour produire des nanopipettes SICM actives dans le SERS (sondes SERS-SICM). Les capacités des sondes SERS-SICM sont démontrées par leur utilisation dans des expériences d'imagerie et de pénétration de cellules vivantes.

Enfin, la préparation de sondes SPM pour la spectroscopie Raman exaltée est poussée à la limite en fixant une seule nanoparticule à l'extrémité d'une nanopipette SICM. Cette conception a le potentiel d'être utilisée pour la spectroscopie Raman exaltée de pointe (TERS) dans les liquides, avec une applicabilité évidente dans les domaines de la biologie tels que les cellules vivantes. Deux méthodes différentes sont présentées, employant des stratégies de synthèse in-situ ainsi que la post-fonctionnalisation des nanopipettes. Les sondes sont évaluées en fonction de leurs capacités pour l'imagerie SICM.

# Acknowledgment

Time flies, it has been almost three years since I came to France. During the past three years, I have not only finished my PhD thesis but also obtained changes and growth. Although both the academic and personal lives are not easy during these years, especially the lockdown time because of covid-19, I still think it is an unforgettable experience with happiness in my life. I am deeply indebted to many people who have given me a lot of help and stood around me with selfless support. Without them, I could not finish this thesis. It is my great honor to take this opportunity to express my deepest appreciation to all of them.

First of all, I wish to express my sincere gratitude to my supervisors, Dr. Aleix Güell and Dr. Razvigor Ossikovski, for providing me with the unique opportunity to study here and this study opportunity changed the rest of my life. I not only broadened my knowledge horizons but also enjoyed European life, which is significantly different from that of China. Throughout my three-year period study, their incomparable enthusiasm for work, rigorous attitude towards scientific research, expert guidance and useful suggestions have always been a great inspiration to me. I truly appreciate their time, great patience and unconditional support.

Besides my supervisors, I would like to thank Dr. Ileana Florea and Dr. Eric Larquet, who taught me how to use TEM technique and helped me acquire HRTEM images. I am also grateful to Dr. Alexandre Baron and Mr. Florian Lochon for kindly providing the simulation data, which is very important to confirm my experimental results. Special thanks also go to the juries of my mid-term defense, Dr. Jongwook Kim and Dr. Robert Lazenby, who gave me a lot of valuable suggestions, and thank them to be my thesis assessment committee members as well. My heartfelt appreciation also must go to Dr. Marc Lamy de la Chapelle, Dr. Nathalie Lidgi-Guigui, and Dr. Carolina Vericat for being my thesis assessment committee members.

Furthermore, I would like to express my sincere gratitude to all the members, including the present and previous ones, in PICM for their kind help. They have helped me a lot not only in my research work but also in my daily life. Everything was too difficult for me at the beginning when I came to France. Luckily, the colleagues in my office (Dr. Daniel Funes-Hernando, Dr. Monalisa Ghosh, and Mr. Junha Park) are so kind that they helped me solve all the problems and took special

attention to take care of me. Dr. Daniel Funes-Hernando also taught me the basic experimental techniques, such as how to use laser puller and SEM. I would also like to thank Dr. Marta San Juan Mucientes, Miss Martina Papa, Mr. Christian Julio Murga Cotrina, Dr. Simon Delacroix, Dr. Ghewa Akiki, Dr. Qiqiao Lin, Dr. Tinghui Zhang, Dr. Shiwei Ren, and Mr. Shenming Wang and Dr. Xinlei Yao for their kind assistance when I encounter difficulties both in experiments and daily life. Miss Martina Papa also kindly helped me do the experiments with living cells and made me acquire some biological knowledge. My great appreciation should also to Dr. Denis Tondelier, Dr. Pavel Bulkin, Dr. Eric Johnson, Dr. Yvan Bonnassieux, and Dr. Pere Roca for providing insightful comments and suggestions to my experiments during the monthly SID meeting. Mrs. Laurence Gerot and Mrs. Gabriela Medina gave me much help with the paper works and purchases. Dr. Jean-Charles Vanel, Mr. Cyril Jadaud, and Mr. Eric Paillassa are so kind help me to solve many technique problems. I must thank their kindness and efficient help. PICM is a warm and joyful laboratory, and I always feel exceptionally lucky and honored to be one of the PICM members.

Moreover, I would like to thank my friends. Dr. Xiaolu Zhuo, Dr. Han Zhang, Dr. Yanzhen Guo, Dr. Ximin Cui, Dr. Caihong Fang, and Miss Dan Wang not only gave me spiritual support but also helped me solve problems in my experiments. They sometimes even made video calls to patiently explain the answers to my questions. Miss Mengyu Gao and Miss Yao Pei gave me a warm companion and moral support during the past three years. Mrs. Tingting Ji, Mrs. Yehui Zhang, Mrs. Hexia Shi, Miss Zijun Zhang, Mrs. Qiaozhen Fang, Mrs. Yan Huang, Mr. Wenhai Wang, and Mrs. Mingyue Wang gave me a lot of help and selfless support.

Last but not least, I would like to express my greatest gratitude to my family for their unconditional love and support as well as encouragement. They always say that I am the pride of them. For me, having them as my family is the most precious asset in my life. My hard-working parents did their best to provide me with a comfortable growth environment. I feel sorry that I have never been back home to accompany them during my PhD study. Thank my sisters, brother, sister-in-law, and brothers-in-law that spent a lot of time taking care of my parents, allowing me to focus on my work. Every success in my life contains the dedication of my family. I am forever grateful and love my family.

# Contents

<b>Abstract</b> .....	<b>I</b>
<b>Résumé</b> .....	<b>III</b>
<b>Acknowledgment</b> .....	<b>V</b>
<b>Contents</b> .....	<b>VII</b>
<b>List of Figures</b> .....	<b>X</b>
<b>List of Tables</b> .....	<b>XV</b>
<b>List of Abbreviations and Acronyms</b> .....	<b>XVI</b>
<b>Chapter 1 Introduction</b> .....	<b>1</b>
1.1 Localized Surface Plasmon Resonance .....	2
1.2 Factors Influencing Localized Surface Plasmon Resonance .....	8
1.2.1 Shape of nanostructure.....	9
1.2.2 Size of nanostructure.....	10
1.2.3 Composition of nanostructure.....	13
1.3 Methods for Preparing Noble Metal Nanostructures .....	14
1.3.1 Seed-mediated method.....	15
1.3.2 Overgrowth .....	19
1.3.3 Oxidation.....	20
1.4 Applications of Plasmonic Nanostructures .....	22
1.4.1 Plasmonic sensing.....	23
1.4.2 Raman spectroscopy .....	27
1.4.2.1 Surface-enhanced Raman spectroscopy.....	30
1.4.2.2 Tip-enhanced Raman spectroscopy .....	34
1.5 Outline of This Thesis.....	40
References.....	41
<b>Chapter 2 Synthesis and Techniques</b> .....	<b>51</b>
2.1 Growth of Gold Nanostructures .....	52
2.1.1 Preparation of gold trisoctahedrons .....	52
2.1.2 Synthesis of gold nanospheres .....	53
2.1.3 Growth of gold nanorods .....	54

2.1.4 Growth of gold nanobipyramids .....	55
2.2 Characterization Techniques.....	55
2.2.1 UV/Vis/NIR spectrophotometry .....	56
2.2.2 Scanning electron microscopy .....	58
2.2.3 Transmission electron microscopy .....	60
2.3 Scanning Ion Conductance Microscopy .....	62
2.3.1 Fabrication of glass nanopipettes.....	64
2.3.2 Scanning ion conductance microscopy imaging.....	66
References.....	67
<b>Chapter 3 A Facile and Fast Method for Synthesizing Gold Trisoctahedrons ....</b>	<b>70</b>
3.1 Preparation of the Gold Trisoctahedrons .....	72
3.1.1 Growth of gold trisoctahedrons with tunable sizes.....	72
3.1.2 The factors for influencing the final morphology of nanostructure.....	78
3.2 Outstanding Properties of Gold Trisoctahedrons.....	88
3.2.1 Refractive index sensitivity.....	88
3.2.2 Surface-enhanced Raman spectroscopy .....	92
3.3 Summary .....	95
References.....	95
<b>Chapter 4 A Strategy for Preparing SERS-SICM Probes .....</b>	<b>98</b>
4.1 Preparation and Characterization of SERS-SICM Probes .....	101
4.1.1 Single-barrel borosilicate nanopipettes coated with gold nanorods .....	101
4.1.2 Single-barrel borosilicate nanopipettes coated with gold nanostructures of varying sizes and morphologies.....	105
4.1.3 Double-barrel quartz nanopipettes coated with gold nanostructures of varying morphologies. ....	110
4.2 SERS Performance of the SERS-SICM Probes.....	112
4.3 Evaluating the Clean Aperture of the Probe and the Anchoring Stability of Gold Nanostructures with SICM Technique .....	116
4.4 Summary .....	120
References.....	120
<b>Chapter 5 The Design of TERS-SICM Probes.....</b>	<b>123</b>
5.1 Anchoring Plasmonic Nanostructures at the Pipette Apex .....	125

5.1.1 Synthesizing gold nanoparticles at the pipette end .....	125
5.1.2 Attaching as-prepared gold nanoparticles on nanopipette by a linker .....	129
5.2 Stability .....	133
5.3 Summary .....	135
References .....	135
<b>Chapter 6 Conclusion and Outlook.....</b>	<b>137</b>
<b>Résumé de la thèse .....</b>	<b>140</b>

# List of Figures

1.1 Schematics of surface plasmon resonance and localized surface plasmon resonance.....	3
1.2 Typical examples of the plasmonic nanostructures .....	4
1.3 Extinction spectra of gold nanostructures of varying sizes .....	5
1.4 Extinction cross-sections of different types of optical species .....	6
1.5 Contours of electronic field intensity enhancements around different gold nanocrystals.....	7
1.6 Photoexcitation and relaxation in metallic nanostructures .....	8
1.7 The extinction spectrum of gold nanobipyramid changes with its sharpness changing .....	10
1.8 The extinction, absorption, and scattering spectra of gold nanospheres with different sizes .....	12
1.9 The variations of the extinction spectra of gold octahedrons with their size increasing .....	13
1.10 Schematic of preparing methods (top-down and bottom-up) for obtaining nanostructures.....	15
1.11 Schematic illustration of the seed-mediated approach for synthesizing gold nanorod.....	16
1.12 Schematic representation of various shapes synthesized by seed-mediated methods using different seeds .....	17
1.13 Schematics illustrating the variation of nanostructures with different growth conditions .....	18
1.14 Schematic displaying three possible deposition modes of atoms on the seed surface .....	19
1.15 Examples of selective oxidation .....	21
1.16 Schematic illustrating the applications of plasmonic nanostructures .....	22
1.17 The variations of extinction spectra of gold nanorods with increasing the refractive index of the surrounding medium.....	23
1.18 The example of using single gold nanorod as sensor .....	26
1.19 Gold nanorod@polyaniline core/shell nanostructure sample for pH detecting sensor.....	27

1.20 Energy diagram illustrating Rayleigh and Raman scattering .....	28
1.21 The principles of Raman spectroscopy .....	29
1.22 Schematics showing the two-step electromagnetic enhancement mechanism ....	31
1.23 Schematic illustrating the typical configuration of TERS technique.....	35
1.24 Schematics of TERS techniques based on different SPM feedbacks .....	37
1.25 Schematics illustrating the optical designs of applying TERS techniques in liquid .....	39
2.1 Schematic of preparing gold trisoctahedron (TOH) .....	53
2.2 Schematic of preparing gold nanosphere (NS) .....	54
2.3 Schematic of preparing gold nanorod (NR).....	55
2.4 Schematic of preparing gold nanobipyramid (NBP) .....	55
2.5 Principles and equipment of UV/Vis/NIR spectrophotometry .....	58
2.6 Principles and equipment of SEM setup.....	60
2.7 Principles and equipment of TEM setup.....	62
2.8 Principles of SICM setup .....	64
2.9 SEM images of single- and double-barrel nanopipettes .....	65
2.10 SICM imaging for different samples .....	67
3.1 Gold trisoctahedron sample .....	73
3.2 Characterization of the gold trisoctahedrons .....	75
3.3 SEM and TEM images of four sizes of gold trisoctahedron samples.....	76
3.4 The variations of the products in colloid color, extinction spectra, and size with increasing the seed volume in the growth solution .....	78
3.5 The influence of growth temperature on the final products.....	80
3.6 SEM and TEM images of nanostructures obtained at 95 °C .....	81
3.7 The product variations with varying amounts of reduction agent in the growth solution.....	82
3.8 The effect of the surfactants in the growth solution on the final products .....	84
3.9 The effect of introducing H <sub>2</sub> PtCl <sub>6</sub> in the growth solution on the final morphology of the products.....	85
3.10 The nanostructures prepared with seed solutions of varying reaction times .....	87
3.11 The variations of gold trisoctahedrons as the reaction time prolonging.....	88
3.12 Extinction spectra and SEM images of three trisoctahedron samples for measuring the refractive index sensitivities .....	89

3.13 Refractive index sensitivities of different gold trisoctahedrons in water-glycerol mixtures.....	90
3.14 The comparison of the refractive index sensitivities between gold nanospheres and gold trisoctahedrons in water-glycerol mixtures .....	91
3.15 The calculated electric field enhancement contours of an individual gold trisoctahedron and a single gold nanosphere by finite element method .....	92
3.16 Extinction spectra of different concentrations of three gold trisoctahedron samples adsorbed with 2-NaT molecules for SERS measurements.....	93
3.17 Raman spectra of different concentrations of three gold trisoctahedron samples adsorbed with 2-NaT molecules.....	94
3.18 The plots of the integrated area of Raman peak as a function of the extinction intensity for three trisoctahedron samples.....	95
4.1 The schematic exhibiting the detailed steps for coating gold nanostructures on the outer surface of a glass nanopipette .....	102
4.2 The representation of SERS-SICM probe.....	103
4.3 The probes obtained without airflow .....	104
4.4 The SERS-SICM probes obtained at different immersing time .....	105
4.5 Gold nanorod samples of varying sizes .....	106
4.6 SEM images of the SERS-SICM probes decorating with gold nanorods of varying sizes .....	107
4.7 The side view SEM images of nanopipettes decorated with gold nanorods of varying sizes about 5 $\mu\text{m}$ and 3 $\mu\text{m}$ away from the end of the corresponding nanopipettes.....	107
4.8 The extinction spectra, SEM images, and TEM images of gold nanospheres, gold trisoctahedrons, and gold nanobipyramids.....	108
4.9 SEM images of nanopipettes fixed with gold nanospheres, gold trisoctahedrons, and gold nanobipyramids, respectively, from side view and top view .....	109
4.10 SEM images of nanopipettes fixed with gold nanospheres, gold trisoctahedrons, and gold nanobipyramids, respectively, at the positions of about 5 $\mu\text{m}$ and 3 $\mu\text{m}$ away from the end of the nanopipettes.....	110
4.11 SEM images of double-barrel quartz nanopipettes fixed with different nanostructures.....	111

4.12 SEM images of quartz nanopipettes fixed with different nanostructures at the positions of about 5 $\mu\text{m}$ and 3 $\mu\text{m}$ away from the end of the nanopipettes .....	111
4.13 SEM images of SERS-SICM probes for SERS measurement.....	112
4.14 The optical micrographs of SERS-SICM probes with 633 nm laser focusing on the tip.....	113
4.15 The Raman spectra of the SERS-SICM probes adsorbed with detection molecules measured from the tips.....	114
4.16 The Raman spectra of the SERS-SICM probes adsorbed with detection molecules measured from the positions of around 5 $\mu\text{m}$ away from the tips .....	115
4.17 The Raman spectra of the bare borosilicate nanopipettes and quartz nanopipettes coated with Raman-active molecules.....	116
4.18 SEM images of the SERS-SICM probe before and after doing SICM imaging, and the SICM map of a living cell .....	117
4.19 The living cell penetration with a SERS-SICM probe.....	118
4.20 SEM images of the SERS-SICM probe before and after inserting into a cell...	119
5.1 Schematic illustrating the proposed design system for doing bottom illumination TERS in a SICM configuration.....	124
5.2 The preparation schematic and SEM images of TERS-SICM probes via in-situ synthesis at nanopipette apex .....	126
5.3 SEM images of the obtained nanopipettes with gold nanostructures, which were prepared through injecting the mixture of seed solution and growth solution without AA into one barrel of the pipette and then immersing the pipette into AA solution.....	127
5.4 SEM images of obtained nanopipettes with gold structures, which were prepared via injecting AA into one barrel of the pipette and then immersing the pipette into the mixture of seed solution and growth solution without AA .....	128
5.5 The representative TERS-SICM probe obtained using MPMS molecules as linkers .....	130
5.6 The extinction spectrum and SEM image of gold nanobipyramids.....	131
5.7 SEM images of obtained TERS-SICM probes with varying gold nanostructures .....	132
5.8 SEM images of TERS-SICM probes with nanoparticles at random positions, obtained using bifunctional molecules as linkers to fix prepared nanoparticles...	133

5.9 SICM imaging using TERS-SICM probe ..... 134

# List of Tables

1.1 The morphologies, sizes, plasmon wavelengths, index sensitivities, and figure of merits for different gold nanoparticles .....	24
4.1 The assignment of the Raman signals for the detected three types of Raman-active molecules (R6G, 4-MBT, and 2-NaT) .....	114

# List of Abbreviations and Acronyms

AA	ascorbic acid
AC	alternating current
AFM	atomic force microscopy
AgNO <sub>3</sub>	silver nitrate
CCD	charge coupled device
CTAB	cetyltrimethylammonium bromide
CTAC	cetyltrimethylammonium chloride
DC	direct current
DMEM	Dulbecco's modified eagle medium
EF	enhancement factor
FDTD	finite-difference time-domain
FOM	figure of merit
FWHM	full width at half maximum
HAuCl <sub>4</sub>	chloroauric acid
HCl	hydrochloric acid
HEPES	N-2-hydroxyethylpiperazine-N'-2-ethane sulfonic acid
HRTEM	high-resolution transmission electron microscopy
H <sub>2</sub> PtCl <sub>6</sub>	chloroplatinic acid
LSPR	localized surface plasmon resonance
MDCK	Madin-Darby Canine Kidney
MPMS	(3-mercaptopropyl) trimethoxysilane
NaBH <sub>4</sub>	sodium borohydride
NIR	near infrared
QRCEs	quasi-reference counter electrodes
R6G	rhodamine 6G
SEM	scanning electron microscopy
SERS	surface-enhanced Raman spectroscopy
SFM	shear force microscopy
SICM	scanning ion conductance microscopy
SPM	scanning probe microscopy
SPR	surface plasmon resonance

## List of Abbreviations and Acronyms

---

STM	scanning tunneling microscopy
TEM	transmission electron microscopy
TERS	tip-enhanced Raman spectroscopy
UPD	underpotential deposition
UV	ultraviolet
Vis	visible
2-NaT	2-naphthalenethiol
4-MBT	4-methylbenzenethiol

# Chapter 1

## Introduction

1.1 Localized Surface Plasmon Resonance .....	2
1.2 Factors Influencing Localized Surface Plasmon Resonance .....	8
1.2.1 Shape of nanostructure.....	9
1.2.2 Size of nanostructure.....	10
1.2.3 Composition of nanostructure.....	13
1.3 Methods for Preparing Noble Metal Nanostructures .....	14
1.3.1 Seed-mediated method.....	15
1.3.2 Overgrowth .....	19
1.3.3 Oxidation.....	20
1.4 Applications of Plasmonic Nanostructures .....	22
1.4.1 Plasmonic sensing .....	23
1.4.2 Raman spectroscopy .....	27
1.4.2.1 Surface-enhanced Raman spectroscopy.....	30
1.4.2.2 Tip-enhanced Raman spectroscopy .....	34
1.5 Outline of This Thesis.....	40
References.....	41

Plasmonic nanostructures with localized surface plasmon resonance (LSPR) properties are able to confine incident light into the near-field nanoscale field, which leads to super strong local electromagnetic field and very large optical absorption/scattering cross-sections. These outstanding advantages of plasmonic nanostructures attract considerable attention and cause tremendous advance in science and technology. Although a big achievement has been obtained in plasmonic research areas and plasmonic applications and even in practical applications, new plasmonic nanostructures with outstanding performances and novel applications are still the research hotspots and continuously being reported almost every day.

I would like to start my thesis with a general overview of the development of plasmonic nanostructures, with the highlights on the basic concepts, variables affecting their properties, preparation methods, and applications. In this chapter, I will firstly introduce what the LSPR is and the intriguing properties of noble metal nanostructures endowed by LSPR (Section 1.1). In Section 1.2, I will give a detailed description on the factors which influence the LSPR properties of noble metal nanostructures. In Section 1.3, I will introduce several types of synthesis methods for plasmonic nanostructures that are highly related to this thesis. I will further introduce the applications of noble metal nanostructures possessed with LSPR properties in Section 1.4, particularly emphasising on the applications in plasmonic sensing and enhanced Raman spectroscopy as the research of my thesis mainly concentrates on these two applications. Lastly, a brief outline of my thesis will be given at the end of this chapter (Section 1.5).

### **1.1 Localized Surface Plasmon Resonance**

Materials endowed with a negative real dielectric constant and a small positive imaginary dielectric constant are able to support a surface plasmon resonance (SPR). The SPR is the coherent oscillation of free electrons in the conduction band between metal and dielectric under external electromagnetic field radiation (Figure 1.1a).<sup>[1-3]</sup> When this SPR is localized in a metal nanostructure with a size which is smaller than the wavelength of light, the free electrons of this nanostructure take part in the collective oscillation, and this is so called localized surface plasmon resonance (LSPR).<sup>[4-5]</sup> Figure 1.1b is a representative schematic of the LSPR supported by a metallic nanosphere, the LSPR phenomenon occurs when the frequency of the

incident light matches with that of the free electron oscillation.<sup>[1]</sup> There are two important effects when the LSPR occurs.<sup>[4,6]</sup> Firstly, the electromagnetic fields around the surface of the nanostructure are considerably enhanced. Secondly, the scattering and absorption of light are greatly enhanced at the resonance wavelength.

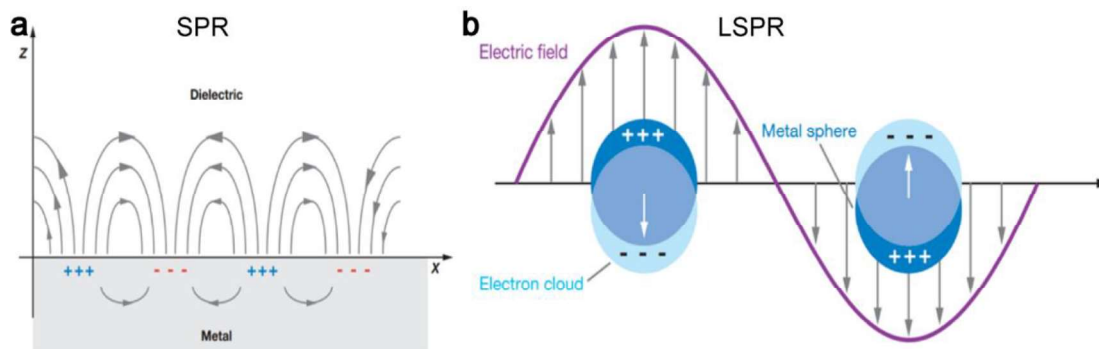


**Figure 1.1** Schematics of surface plasmon resonance (a), and localized surface plasmon resonance (b).<sup>[1]</sup>

Noble metal nanocrystals have chemical stability and high electric conductivity which are good candidates to support LSPRs. Among them, gold and silver nanoparticles, long-investigated nanostructures, can be traced back to the 4<sup>th</sup> century.<sup>[7-8]</sup> Artists and workers used gold and silver nanoparticles as pigments to fabricate fascinating artworks, including cups and beautiful windows. The famous Lycurgus cup is a typical example of this application (Figure 1.2a).<sup>[9]</sup> The cup was made by embedding a tiny amount of gold and silver nanoparticles into the glass and these nanoparticles are able to absorb and scatter light at specific wavelengths in visible regions.<sup>[10]</sup> The color of this cup depends on whether the illuminating light is passing through it or not, appearing red when the light shines inside or behind of the cup because of the transmitted light and turning into green if the light illuminates from front of the cup due to reflected light.<sup>[11-12]</sup> Another spectacular example is the amazingly colorful windows of Sainte Chapelle in Paris,<sup>[13]</sup> as appreciated in the photo in Figure 1.2b. During ancient times, this stained technique was widely applied without a scientific understanding of the behind mechanism. The first scientific research on the synthesis of gold nanostructures was performed by Michael Faraday in 1847, which is considered as the pioneer of nanoscience. The red gold colloid (Figure 1.2c) was prepared by reducing chloroaurate with phosphorus in carbon disulfide.<sup>[14]</sup> People were interested in the intense colors and considered the attractive colors were an inherent characteristic of gold nanoparticles. Only until the appearance

of electrodynamic theory in the early twentieth century that people realized the beautiful colors of gold nanoparticles were because of the LSPRs.



**Figure 1.2** Typical examples of the plasmonic nanostructures. (a) The Lycurgus cup.<sup>[12]</sup> (b) The stained windows of Sainte Chapelle in Paris, this photo is provided by my friend, Miss Martina Papa. (c) Gold nanoparticles colloid by Michael Faraday in the museum of the Royal Institution in London.<sup>[15]</sup>

The magic Lycurgus cup and beautiful windows prove that the properties of noble metal nanostructures are significantly different with those of bulk counterparts. LSPR endows noble metal nanostructures with outstanding properties. The first is that the LSPR wavelength of noble metal nanostructures is tunable, which is highly dependent on their compositions, morphologies, sizes, and local dielectric surroundings.<sup>[16–18]</sup> Taking gold nanospheres as an example, Figure 1.3a illustrates the LSPR wavelengths of gold nanospheres.<sup>[19]</sup> Generally, gold nanospheres have one LSPR dipolar mode and the wavelength gradually red shifts with the size of gold nanospheres increasing. However, gold nanorods have two typical LSPR modes, one is longitudinal dipolar mode generated from the electron oscillations along the long axis of the nanorods, the other one is transverse dipolar mode which is excited by light polarized along the short axis of the nanorods.<sup>[20]</sup> In figure 1.3b, it is apparent that the longitudinal LSPR wavelength of gold nanorods can be tuned, the wavelength gradually red shifts with increasing the aspect ratio (ratio between the length and diameter) of gold nanorods.<sup>[21]</sup> As for transverse wavelength, it is less sensitive to the change of aspect ratio.

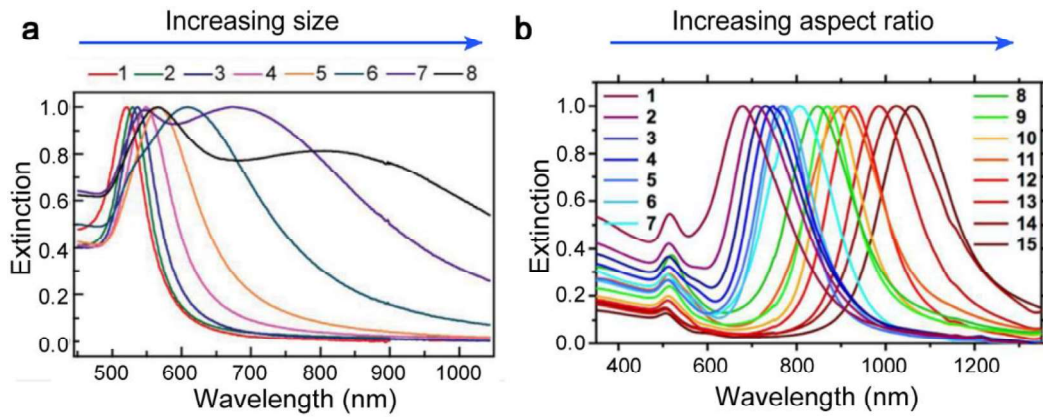


**Figure 1.3** Extinction spectra of gold nanostructures of varying sizes. Extinction spectra of gold nanospheres with increasing size (a),<sup>[19]</sup> and gold nanorods with increasing aspect ratio (b).<sup>[21]</sup>

The second attractive feature of noble metal nanostructures is that their absorption and scattering cross-sections are extremely large at the plasmon resonance frequency. The comparison among different nanoscale optical species is illustrated in Figure 1.4, including plasmonic nanostructures, semiconductor quantum dots, organic fluorophores, and atom/ions.<sup>[22–23]</sup> All of them possess very strong interactions with incoming light and the cross-sections greatly increased when the size of the particles is increasing. Among them, plasmonic nanostructures have much larger cross-sections than the other three types of nanoscale optical species. Furthermore, only plasmonic nanostructures have larger extinction cross-sections than their physical cross-sections. The optical specie with larger extinction cross-section means that this optical specie has higher probability to absorb or scatter incident light. Hence, plasmonic nanocrystals have better absorption and scattering ability compared to other three types of optical species.

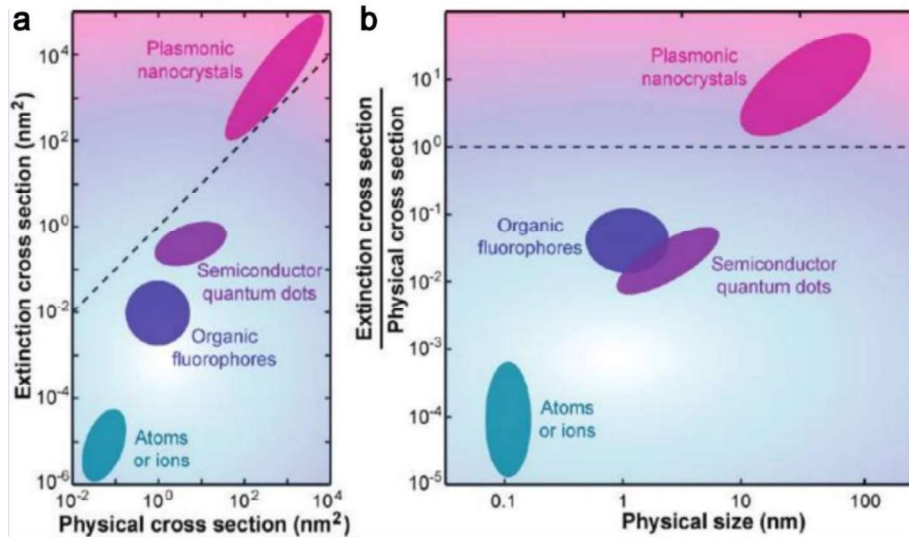


**Figure 1.4** Extinction cross-sections of different types of optical species.<sup>[22]</sup> (a) Comparison among extinction cross-sections of four types of nanoscale optical species. (b) The ratios between extinction cross-sections and physical cross-sections of the optical species versus their physical sizes.

Another exceptional property of noble metal nanostructures is the strong confinement of incident light into nanoscale area surrounding the nanoparticle which has already broken the diffraction limit of the traditional optics.<sup>[24–26]</sup> Therefore, the localized electromagnetic field is highly enhanced by the strongly confined light. This enhancement reaches maximum at the surface and decreases quickly with distance. Moreover, the enhancement can be further improved by increasing the curvature of the plasmonic nanostructures.<sup>[27–28]</sup> Figure 1.5 presents the contours of electromagnetic field enhancements around three different nanocrystals, including gold nanosphere, gold nanorod and gold nanoplate, which are acquired from finite-difference time-domain (FDTD) simulations.<sup>[23]</sup> These three types of nanostructures have the same volume, however, the intensities of the enhancements are considerably different. Gold nanoplate with sharp tips has the strongest electromagnetic field distribution among these three nanostructures. Therefore, it is believed that the sharper a noble metal nanostructure is, the stronger the field it produces.

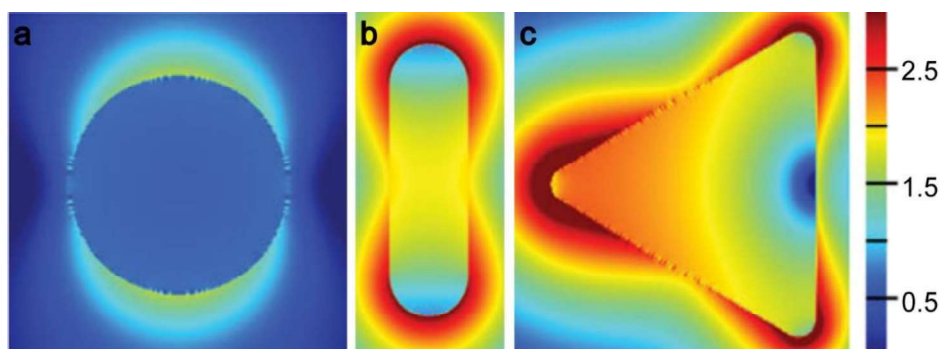


**Figure 1.5** Contours of electronic field intensity enhancements around different gold nanocrystals.<sup>[23]</sup> Gold nanosphere (a), gold nanorod (b), and gold nanoplate (c).

Moreover, noble metal nanostructures with LSPRs are capable of being applied to induce hot carriers, which is beneficial for developing various research areas, such as photocatalysis, solar energy conversion, imaging and so forth.<sup>[29–30]</sup> The development of surface femtochemistry promotes the understanding of the behind mechanism of the hot carrier generation process.<sup>[31]</sup> Figure 1.6 illustrates the process by which plasmon induces hot carriers in metallic nanostructures.<sup>[32]</sup> To absorb a photon is the first step for exciting a carrier (Figure 1.6a), the probability to greatly improve the light absorption of noble metal nanostructures is exciting LSPRs.<sup>[31–32]</sup> After light absorption, the plasmon resonances in metallic nanocrystals can be damped either by a radiative process to re-emit a new photon, or through a non-radiative path to create the electron-hole pairs, only within a timescale ranging from 1 to 100 fs due to the process is a pure quantum mechanism (Figure 1.6b).<sup>[33]</sup> These plasmon excited carriers will relax by the process of electron-electron scattering using around 100 fs to 1 ps. This step will result in the formation of Fermi-Dirac like distribution (Figure 1.6c).<sup>[34]</sup> This charge distribution will further experience via interaction with phonon modes in a few picoseconds which leads to heating the nanostructures. In the final step, the heat will transfer from the nanostructures to their surrounding environment by taking an approximate time from 100 ps to 10 ns (Figure 1.6d). This transfer time is significantly decided by the materials and size of the nanostructures as well as the thermal conduction features of the surrounding environment.<sup>[31]</sup>

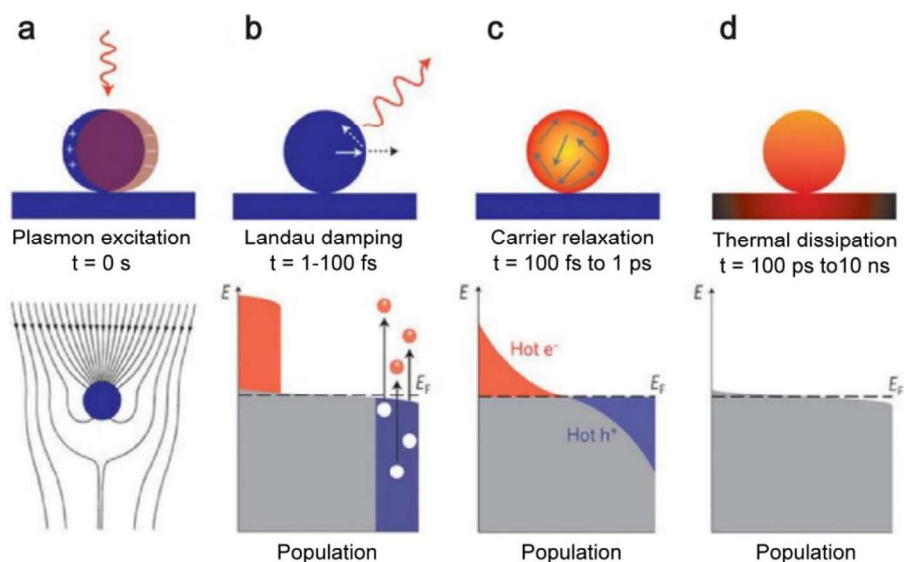


**Figure 1.6** Photoexcitation and relaxation in metallic nanostructures.<sup>[31]</sup> On the top row, it illustrates the process of photoexcitation and relaxation in a nanostructure illuminated with a laser pulse as well as the corresponding timescales. On the bottom row, it shows the excitations of LSPR redirects the flow of light towards and into the nanocrystal (a), and the population of the electronic states (grey), the red and blue areas represent the distributions of hot electrons and hot holes, respectively (b-d).

These outstandingly plasmonic features of noble metal nanostructures make them widely applicable in many areas. In the field of converting solar energy, noble metal nanocrystals are able to enhance light harvesting and the efficiency of solar cells.<sup>[35–36]</sup> In biological sciences, noble metal nanostructures can be used in labelling and imaging cells, sensing, diagnosis and photothermal conversion-based therapy.<sup>[37–39]</sup> Moreover, noble metal nanoparticles can be utilized in storage of optical data,<sup>[40]</sup> electro-photonic circuits,<sup>[41]</sup> etc. The more detailed descriptions of applications of noble metal nanostructures will be provided in Section 1.3.

## 1.2 Factors Influencing Localized Surface Plasmon Resonance

As discussed in Section 1.1, the LSPR properties of noble metal nanoparticles are highly dependent on their sizes, morphologies, and compositions. Understanding this dependence is essential for exploring new devices and applications. In this section, I will introduce the effects of nanoparticle shape on the LSPR property firstly, followed by describing the important role of nanoparticle size. Lastly, I will give a brief introduction to the chemical compositions.

### 1.2.1 Shape of nanostructure

The existing relationship between shape and LSPR in noble metal nanocrystals, including gold, silver, platinum and palladium, is especially noticeable. The number of LSPR peaks, their wavelengths, and the ratio between scattering and absorption are all influenced by the geometric shape of noble metal nanoparticles due to its impact on the distribution of charges surrounding noble metal nanoparticles and the polarization of free electrons.<sup>[42]</sup> Firstly, many research results have demonstrated that the number of LSPR peaks increases when the symmetry of a noble metal nanostructure decreases.<sup>[43]</sup> As mentioned in Section 1.1, the highly symmetrical gold nanosphere generally only possesses one single plasmonic dipolar peak. In comparison, other anisotropic nanostructures, such as gold nanorods or nanobipyramids, exhibit two dipolar modes, as the two different dimensions including length and width make it possible to polarize the oscillations along two different ways.<sup>[20, 44]</sup>

The wavelengths of LSPR peaks are also greatly influenced by the geometrical shapes, especially the sharpness of corners and edges.<sup>[17, 45–46]</sup> Taking gold nanobipyramids with relatively sharp tips as a representative example (Figure 1.7a), it displays a very strong dipole resonance peak in the visible region and this peak is significantly sensitive to the sharpness of the tips. Figure 1.7b and c display that increasing the roundness of the tip leads to the LSPR peak gradually but significantly blue shifting.<sup>[47]</sup> A sharper tip can result in the increase of charge separation and the reduction of restoring force for the dipole electron oscillation, therefore, the sharper the tip, the longer the plasmonic wavelength is.<sup>[43]</sup> Furthermore, the sharpness of a nanostructure is capable of dramatically enhancing the near fields intensity surrounding its surface.<sup>[48–49]</sup> This phenomenon, known as the “lighting rod” effect, is highly dependent on the surface curvature of the nanostructure. For example, gold nanobipyramid exhibit a greater local electronic field enhancement in comparison to gold nanorod.<sup>[44]</sup> Because of the above reasons, gold nanostructures with sharp corners are promising candidates for a number of applications such as surface-enhanced spectroscopies and nonlinear optics.<sup>[50–53]</sup>

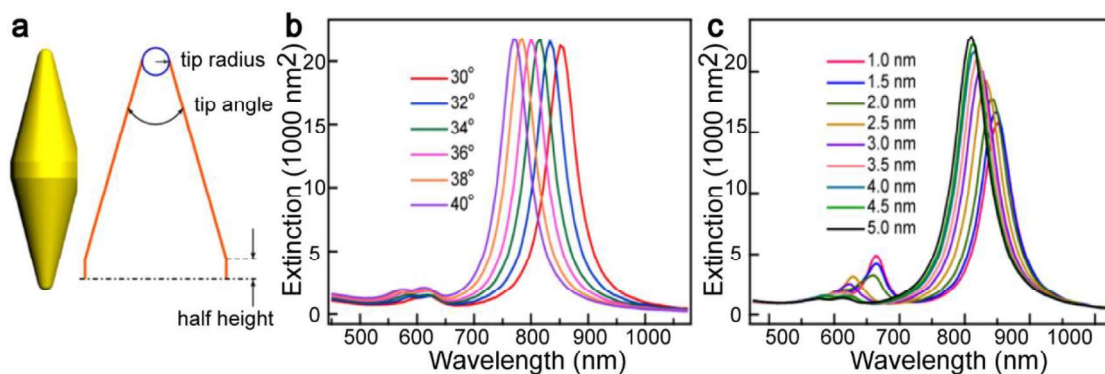


**Figure 1.7** The extinction spectrum of gold nanobipyramid changes with its sharpness changing.<sup>[47]</sup> (a) Schematics are the three-dimensional mode and two-dimensional mode of a gold nanobipyramid. (b) FDTD calculated extinction spectra of gold nanobipyramids as the tip angle increases while the tip radius keeps constant. (c) FDTD simulated extinction spectra of gold nanobipyramids with various of tip radius while the tip angle remains a fixed number.

The scattering and absorption cross-sections of noble metal nanostructures are also affected by their geometrical shapes.<sup>[42, 54]</sup> The nanostructures with highly symmetrical shape are able to form strong dipole which results in strong absorption and scattering. However, nanostructures like triangular plates with lower geometrical symmetry cannot form strong dipole because the corners of the triangular are opposite to a face rather than another corner.<sup>[43]</sup> In addition, the geometrical morphology plays a role in determining the ratio between scattering and absorption as well.<sup>[42, 54]</sup> Noble metal nanostructures like nanorods, nanocages and nanostars with stronger absorption have been widely explored for photothermal therapy.<sup>[55]</sup> On the other hand, the highly scattering dominated polyhedron nanoparticles, such as cuboctahedron and octahedron, are favorable for biological imaging and detection.<sup>[56]</sup> The ratio may be more determined by the size of nanostructures, which will be introduced in detail in next section.

### 1.2.2 Size of nanostructure

Size is another parameter in noble metal nanostructures that influences LSPR properties. The ability to tune nanostructure size can be used to tune the proportion of scattering to absorption, but also can shift the peak position of LSPR and change the number of plasmonic modes.

For noble metal nanostructure whose size is much smaller than the wavelength of incident light, the cross-sections of scattering and absorption are directly proportional to the 6<sup>th</sup> and 3<sup>rd</sup> power of its size, respectively.<sup>[57]</sup> Taking gold nanosphere as a typical example, small particles with radius lower than 30 nm possess very high absorption yet very weak scattering, which makes these small particles very difficult to measure by dark-field microscopy. However, these particles with strong light absorption can convert photon energy into heat rapidly which is beneficial for photothermal therapy to destruct cancer cells.<sup>[58]</sup> For large nanoparticles, scattering dominates over absorption, and particles are seen as very bright in dark field microscopy. Based on the dark field microscopy technique, noble metal nanostructures with outstanding light scattering have been widely exploited in the application of optical imaging, such as imaging gold nanoparticles in biological cells, understanding biological process with real time imaging, detecting biomolecular dynamics and so on.<sup>[59]</sup> For the particles with a radius around 50 nm, scattering and absorption become comparable. Figure 1.8 is the example of the extinction, absorption, and scattering spectra of gold nanospheres dispersed into water which exemplifies all the above-mentioned trends: the extinction of small gold nanospheres is dominated by absorption; the scattering increases significantly when the size increased to about 72 nm, although absorption is still slightly over scattering; and finally for large gold nanospheres (size of approximately 162 nm), the extinction spectrum is almost exclusively composed of scattering.<sup>[60]</sup> It is important to point out that two peaks appeared in the extinction spectrum of large nanospheres, one peak is the dipolar mode and the other peak is because of the appearance of a quadrupole excitation. Therefore, the size of nanostructures is able to affect the number of plasmonic mode. Generally, there are only dipole modes in small nanocrystals while there are multipole modes in large nanocrystals as well in addition to dipole modes.

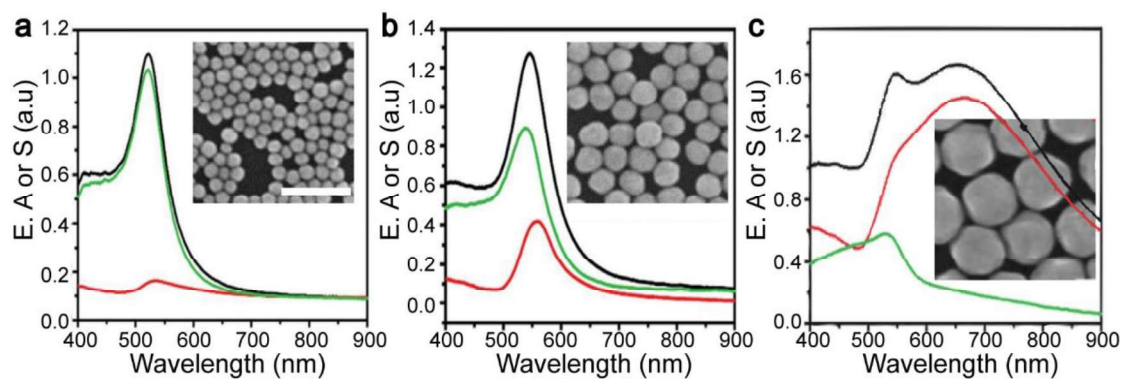


**Figure 1.8** The extinction (black), absorption (green), and scattering (red) spectra of gold nanospheres with different sizes.<sup>[60]</sup> The diameters are  $41 \pm 2$  nm (a),  $72 \pm 3.8$  nm (b), and  $162 \pm 9$  nm (c). The insert images are the corresponding scanning electron microscopy images of gold nanospheres, the scale bar is 200 nm.

Figure 1.8 also demonstrates that the peak position gradually red shifts as the diameter increases. This trend occurs because the charge separation on the nanosphere increases with its size, which results in the frequency of the free electron oscillation decreasing. This trend also happens in nonspherical nanostructures such as nanocubes<sup>[61]</sup> and nanooctahedrons.<sup>[62]</sup> In Figure 1.9, a representative scanning electron microscopy (SEM) image of gold octahedron is presented (Figure 1.9a), together with a set of extinction spectra that clearly shows the main dipole peak gradually red shifts with the edge length increasing (Figure 1.9b). The relationship between dipole plasmonic peaks of the gold octahedrons and the lengths of their edges is approximately linear (Figure 1.9c), which is important towards the synthesis of gold octahedrons with special plasmonic peak. For the elongated nanostructures like nanorods and nanobipyramids, they have two types of dipole modes, longitudinal mode and transverse one. Their longitudinal plasmonic peak slowly red shifts with the aspect ratio increasing.

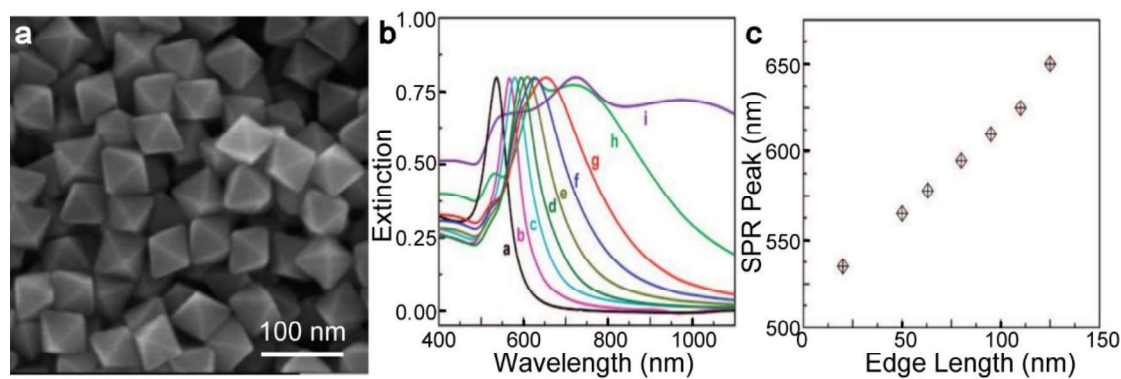


**Figure 1.9** The variations of the extinction spectra of gold octahedrons with their size increasing.<sup>[62]</sup> (a) The SEM image of 50 nm gold octahedrons. (b) The extinction spectra of gold octahedrons with different edge lengths, the edge lengths are 20 nm, 50 nm, 63 nm, 80 nm, 95 nm, 110 nm, 125 nm, 160 nm, and 230 nm, respectively. (c) The relationship between plasmonic peaks and edge lengths.

Apart from above effects, the size of nanostructure can also affect the width of plasmonic peak. Figure 1.8 and 1.9 also show that the dipole peak becomes broader when the size increases. This broadening is attributed to radiative damping for large nanostructures.<sup>[63]</sup>

### 1.2.3 Composition of nanostructure

Noble metals generally include Platinum-group metals (Ru, Rh, Pd, Os, Ir and Pt) and coinage metals (Au and Ag). For the Platinum-group metals, nanoparticles are excellent candidates for catalytic applications but without significant LSPR properties due to the partially occupied d-states result into the probability of low frequency interband transitions and the enhancement of the LSPR relaxation frequency caused by the increase of electron-electron scattering rate.<sup>[64–66]</sup> For the nanostructures of coinage metals, the densities of their free electrons are in the proper range that makes them to have outstandingly tunable plasmonic properties in a broad range of wavelength.<sup>[5, 67]</sup> According to Mie theory, the resonance occurs when the real part of the permittivity of a metal equals twice the negative of the permittivity of its surrounding medium. Due to the surrounding medium being usually water or air with a positive dielectric constant, the real part of the dielectric constant of the metal should be negative. Additionally, the small number of imaginary part is required because it may affect the plasmonic resonance peak. Gold and silver are the two types of metals which can fulfill the conditions.<sup>[17, 49]</sup>

Since the inherent characteristics of a metal is unique with each other, the plasmonic properties of gold and silver nanostructures can be greatly different. For instance, comparing plasmonic sensitivity of single silver nanorod with that of single gold nanorod shows that silver nanorods possess higher sensitivity than gold nanorods at the similar plasmonic resonance wavelengths.<sup>[68]</sup> However, the structural stability of silver is low and silver nanostructures are not suitable for biological applications because of high cytotoxicity.<sup>[69]</sup> These two obstacles hinder the applications of silver nanocrystals. On the other hand, gold nanoparticles with advantages like chemical inertness, oxidation-free, and low toxicity have already made gold nanostructures to be remarkably important nanomaterials in the fields of chemical and biological applications.<sup>[59, 70]</sup>

From above description, it is apparent that the element composition of a nanoparticle plays an essential role in determining its properties and applications. In order to solve the disadvantages of monometallic nanostructures and improve their applications, a lot of research work are devoted into developing alloy nanostructures as well. Various of combinations among different metals shows high flexibility of tuning properties of noble metal nanostructures.

### **1.3 Methods for Preparing Noble Metal Nanostructures**

Since the LSPR properties of noble metal nanostructures are highly dependent on their physical parameters, many different strategies have been developed to prepare nanostructures with various shapes, sizes and compositions for different applications. These strategies can be classified into top-down and bottom-up methods.<sup>[71-74]</sup> Figure 1.10 displays the principles of these two preparing methods. Top-down methods refer to the techniques which involve the milling and comminution of the bulk materials to obtain the desired nanostructures. Electron beam lithography and photolithography are the two commonly employed top-down methods. Oppositely, the bottom-up methods start from reducing the salt precursors to atoms and then gradually assemble the atoms to the desired nanostructures. Although a large number of noble metal nanostructures are fabricated by top-down methods, it is hard to avoid many drawbacks during the process of preparation, including expensive, time-consuming, and wasting materials.<sup>[75-76]</sup> Furthermore, the plasmonic properties of noble metal nanostructures fabricated by these physically top-down methods are largely damped

due to their polycrystalline nature and the adhesive layer.<sup>[77–79]</sup> These shortcomings are the main reasons for limiting the use of top-down approaches in both fundamental research and practical applications. On the other hand, bottom-up methods are generally the inexpensive and simple way with a huge potential for controlling the sizes and shapes of nanostructures.<sup>[39, 80]</sup> The bottom-up methods generally involve wet-chemical synthesis processes, such as chemical, electrochemical, photochemical and sonochemical procedures. There are commonly three key species involved in bottom-up approaches: the metal precursor which is the source for growing nanostructures; the reducing agent or energy for driving reduction or decomposition process; and the capping agent which plays an important role in stabilizing the nanostructures.<sup>[74]</sup> In this section, I will mainly focus on introducing the methods related to my work, including the seed-mediated method, overgrowth and oxidation.

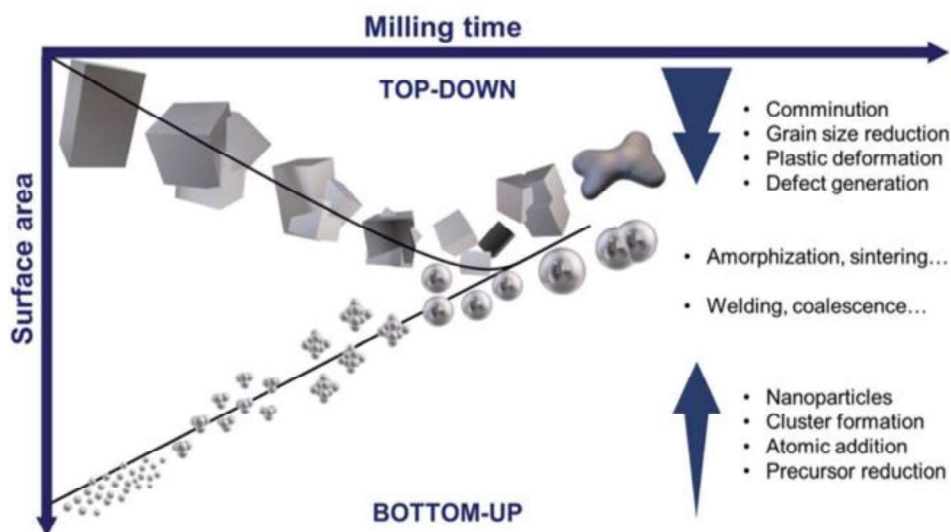


**Figure 1.10** Schematic of preparing methods (top-down and bottom-up) for obtaining nanostructures.<sup>[74]</sup>

### 1.3.1 Seed-mediated method

Seed-mediated method, one of the most popular wet-chemical method for the synthesis of noble metal nanostructures, was proposed by Murphy *et al.* in 2001.<sup>[81–82]</sup> Until now, tremendous success has been achieved in preparing noble metal nanostructures with various of shapes, such as nanocubes, nanorods, nanospheres, nanoplates, nanobipyramids and so on. A typical seed-mediated growth process is generally comprised of two main steps.<sup>[73, 83–85]</sup> The first step is to prepare small particles as seeds. Specifically, a strong reducing agent like sodium borohydride is

used to rapidly reduce salt metal precursor (for example, chloroauric acid) into atoms and then these atoms form into small particles through self-nucleation. This step is crucial for obtaining high-quality nanostructures. The following step is preparing growth solution which includes metal precursors, shape-directing agents, and reducing agents. By adding a certain volume of as-prepared seed particles into growth solution, the noble metal nanostructures can be gradually formed. The reducing ability of reducing agent in growth solution is significantly lower than that in preparing seed particles, therefore, the metal atoms only gradually deposit onto preformed seed particles and are not able to form new particles.<sup>[80]</sup> Importantly, the stabilizing agent must be used in both steps to stabilize the particles. Figure 1.11 shows a well-known example of the synthesis of gold nanorods by seed-mediated method.<sup>[20]</sup> The small seeds are obtained by reducing chloroauric acid ( $\text{HAuCl}_4$ ) using sodium borohydride ( $\text{NaBH}_4$ ). Then injecting gold seeds into the growth solution including  $\text{HAuCl}_4$ , silver nitrate ( $\text{AgNO}_3$ ), ascorbic acid (AA), and cetyltrimethylammonium bromide (CTAB). AA reduces  $\text{Au}^{3+}$  to  $\text{Au}^+$ , and the addition of gold seeds is capable of catalyzing  $\text{Au}^+$  to  $\text{Au}^0$  therefore finally produce gold nanorods.<sup>[20, 86–87]</sup>

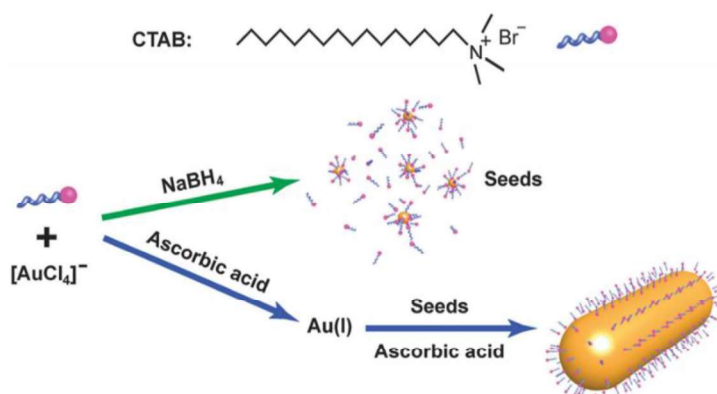


**Figure 1.11** Schematic illustration of the seed-mediated approach for synthesizing gold nanorod.<sup>[20]</sup>

Although seed-mediated methods are a bit more complicated than the traditional one-step protocols for producing noble metal nanocrystals, many advantages can be obtained from the separation of seed nucleation and growth step, that results in achieving sustained and predictable preparation of noble metal nanostructures.

The first advantage is that precisely controlling the size of the final nanostructures becomes possible. In seed-mediated method, nanostructures of different sizes are able to be acquired by simply selecting the ratio between the salt precursor and seeds in the growth solution.<sup>[88]</sup> Generally, the particle size will gradually increase with the ratio

increasing. This control of the size over a large range of dimensions is, however, not possible using a typical one-pot synthesis method, as increasing the concentration of the salt precursor may create more nucleation which probably decreases the driving force for the growth of nanoparticles. In contrast, using seed-mediated method can avoid extra nucleation due to the well-controlled concentration of salt precursors in growth solution, thus the newly reduced atoms can all be grown onto pre-existing seeds leading to continuous growth.

Secondly, the utilization of seed-mediated method allows the design of the shape of nanostructures by thoughtfully choosing the type of seeds.<sup>[43, 89]</sup> Figure 1.12 illustrates that various silver nanostructures can be prepared through using different types of seeds.<sup>[43]</sup> For example, the growth solution with multiply twinned seeds can yield nanostructures with the morphology of quasi-spheres, wires, and rods, while injecting singly twinned seeds into growth solution is able to generate right bipyramids and beams. Single crystalline seeds lead to the formation of spheres, cubes, and octahedrons.

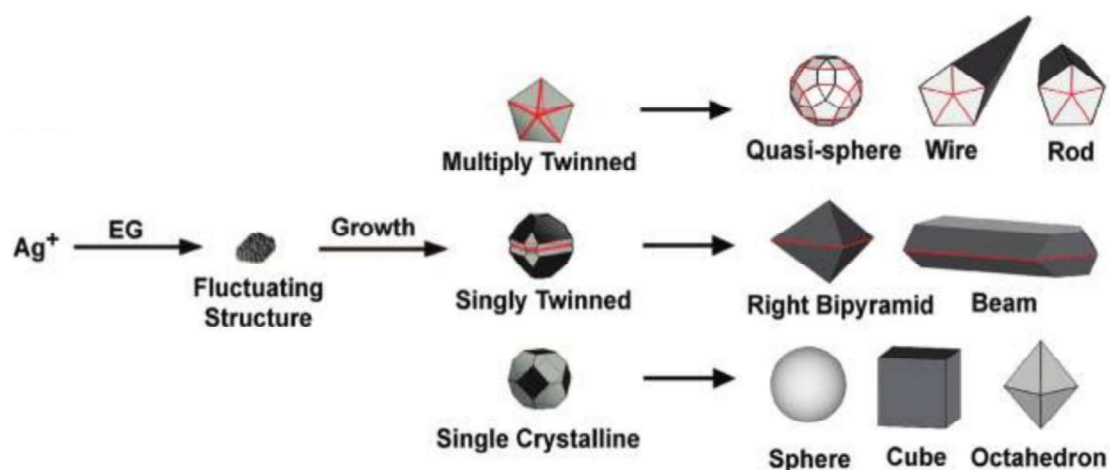


**Figure 1.12** Schematic representation of various shapes synthesized by seed-mediated methods using different seeds.<sup>[43]</sup>

Moreover, special morphology can be synthesized by controlling the growth rates of different crystallographic faces on the seeds. Adding some additives, such as ions, small molecules, polymers, and surfactants, in the growth solution can selectively deposit onto some crystal facets leading to the growth rate on these facets slowing down, therefore determining the terminal shape of nanostructures.<sup>[80, 90]</sup> The facet-blocking approaches have been widely used for obtaining a variety of nanostructures. Among them, employing foreign metal ions as a shape-directing agent is one of the most effective and extensive strategies to block some crystal facets. The main

hypothesis of the growth mechanism assisted with the foreign metal ions involves underpotential deposition (UPD) which is a phenomenon of reducing metal ions onto a solid metal at a potential that is lower than the equilibrium potential applied for reducing these metals.<sup>[91–93]</sup> The UPD phenomenon for foreign metal ions preferably occurs on high-energy facets with abundant kinks, edges, and atomic steps, and then the as-formed monolayer of foreign metal can play a role in blocking the growth of the facets.<sup>[80, 94]</sup> One of the well-known shape-directing agents is silver nitrate, which is broadly used in the formation of many kinds of nanostructures. In 2001, Murphy *et al.* observed that the addition of  $\text{Ag}^+$  ions had a significant effect on the formation of gold nanorods, as  $\text{Ag}^+$  ions selectively bind on the  $\{110\}$  facets with higher surface energy than that of  $\{100\}$  facets. As a result, the growth rate on  $\{110\}$  facets is decreased while the growth rate on  $\{100\}$  facets is very fast. The difference in growing rate on different facets breaks the symmetry of structures, resulting in the production of the anisotropic nanorods.<sup>[82, 95]</sup> Ten years later, Mirkin *et al.* demonstrated that different nanostructures can be obtained by simply altering the ratio between  $\text{Ag}^+$  and  $\text{Au}^{3+}$  in growth solution (Figure 1.13a).<sup>[96]</sup> Increasing the concentration of  $\text{Ag}^+$  ion in the growth solution, the morphology of the obtained nanostructures will change from  $\{110\}$ -faceted rhombic dodecahedra to  $\{310\}$ -faceted truncated ditetragonal prisms and then to nanostructures with higher index facets, such as  $\{720\}$ -faceted concave cubes.

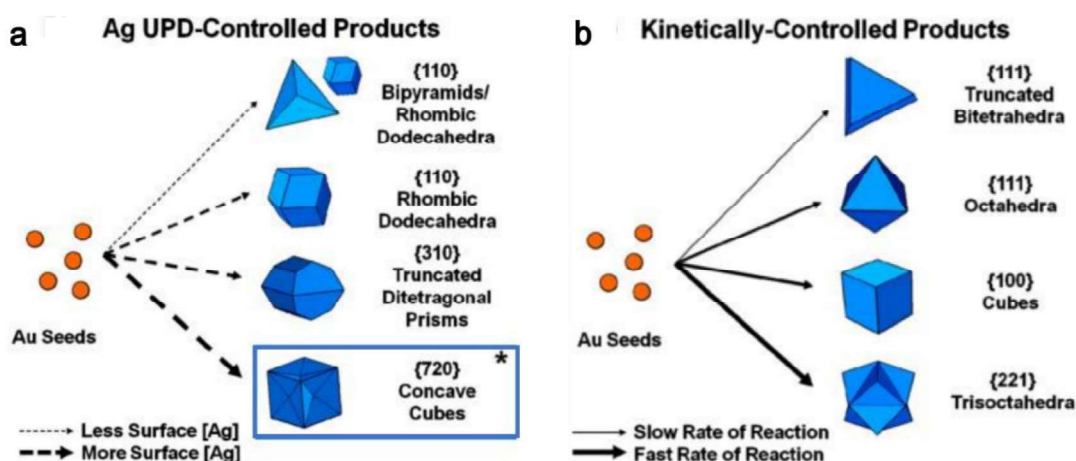


**Figure 1.13** Schematics illustrating the variation of nanostructures with different growth conditions.<sup>[96]</sup> (a) The Schematic illustrates the changes of the final shape of nanostructures with the concentration of silver ion increasing. (b) The schematic of kinetically controlled morphologies without silver ions in the growth solution.

In addition, Mirkin *et al.* investigated that the reaction rate can influence the shape of the products without silver ions as well (Figure 1.13b).<sup>[96]</sup> Nanostructures with higher surface energy can be yielded when the growth rate is higher. Higher reaction temperature, higher concentration of reagents, or surfactants with smaller halides (Cl) can achieve higher reaction rate. Therefore, controlling the reaction kinetics is another powerful and versatile method to synthesize nanostructures with different morphologies.

### 1.3.2 Overgrowth

Overgrowth strategy for preparing nanostructures is developed based on seed-mediated method, which takes as-prepared nanocrystals as seeds and further growing to larger particles by depositing the same or different metals. As mentioned in Section 1.3.1, atoms tend to deposit on the facets with higher surface energy, such as uncapped regions, corners, edges, and vertices, therefore, injecting the as-prepared nanostructures into a new growth solution, the equilibrium shape will be broken leading to continuously growing. Since the difference of lattice constant and the deposit rate of atoms can be altered by changing experimental conditions, three modes of overgrowth have been recognized (Figure 1.14).<sup>[97–98]</sup> When the nanostructures gradually grow in a layer-by-layer fashion, that is so-called Frank-van der Merwe mode. If the difference of the lattice constants between two interfacing materials is very large, the growth is unable to follow the layer-by-layer manner, forming three-dimensional islands on the as-prepared nanostructures, this is Volmer-Weber mode. The third mode is the Stranski-Krastanov which mixed layer-by-layer growth and island growth.

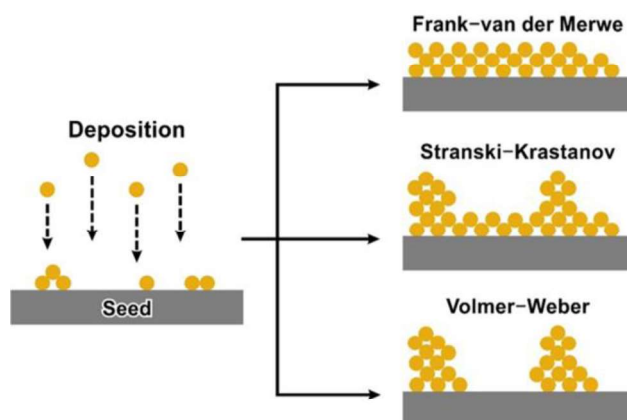


**Figure 1.14** Schematic displaying three possible deposition modes of atoms on the seed surface.<sup>[98]</sup>

A large number of nanostructures have been synthesized by overgrowth approach. For example, Zhuo and coworkers employed gold nanobipyramids as seeds to prepare highly uniform silver nanorods.<sup>[99]</sup> AuPd nanostructure which is composed of a gold nanorod as core and small palladium nanoparticles with sizes of around 2–4 nm surround the core.<sup>[100]</sup> Apart from the bimetallic and multi-metallic nanostructures, overgrowth method is also used to grow larger particles. Taking gold nanosphere as an example, the larger nanospheres are obtained through the overgrowth of 20 nm gold nanospheres.<sup>[19]</sup>

### 1.3.3 Oxidation

Oxidation is another strategy to obtain noble metal nanostructures, which is based on seed-mediated method as well. It is an effective approach to reshape noble metal nanostructures and tailor their plasmon wavelengths. The injection of oxidizing agents, such as hydrogen peroxide, oxygen, and salt precursors, leads to zero-valence atoms becoming ions and desorbing away from the surface of nanostructures, thus reshaping nanostructures and tailoring size can be achieved.<sup>[101–103]</sup> Similar to overgrowth, the oxidation tends to occur at the edges, corners and vertexes which possess high surface energy. The surface chemistry of metal nanoparticles, surfactants, and the covered species like molecules and ions on nanocrystals can influence the oxidizing process. Additionally, reaction temperature, the concentration of the oxidizing agent, and the pH of the reaction solution are able to determine oxidation rate.<sup>[103–105]</sup> These factors thereby provide many opportunities to reshape nanoparticles and reduce their size as well. Interestingly, since the plasmonic peak of extinction spectrum is highly dependent on the size of nanostructure, it is possible to monitor the oxidizing process by following the changes in the extinction spectra of nanostructure colloids with oxidation time.

An interesting example of the applicability of the oxidation in nanostructure growth is the case of gold nanorods, which can obtain a set of gold nanorods with different lengths but similar widths, however, both the length and the width change as changing the amount of seed in the growth solution by the seed-mediated method. Tsung reported the simple oxidation method to selectively shorten the lengths of gold nanorods using oxygen as oxidizing agent.<sup>[101]</sup> Due to the lower densities of surfactants at the two ends of gold nanorod, the selective oxidation gradually happens

at the two ends, resulting in the length is slowly shorten while the width remains unchanged (Figure 1.15a). As the reaction time increases, the longitudinal plasmonic wavelength gradually blue shifts and the intensity of the peak slowly decreases at the same time (Figure 1.15b). The desired gold nanorods can be acquired through centrifuging the reaction colloid when the longitudinal plasmonic peak moves to a required position and then the obtained gold nanorods redisperse into water.

Another example is that the opening and overall size of gold nanobottles can be further tuned through using hydrogen peroxide as oxidizing agent.<sup>[106]</sup> In the presence of hydrogen peroxide, the opening size of the gold nanobottles increases while the overall size decreases with the oxidizing time increasing (Figure 1.15c). Meanwhile, both the axial (electric, short wavelength) and transverse (magnetic, long wavelength) plasmon peaks gradually change (Figure 1.15d). Figure 1.15e shows the typical SEM images of four nanobottle samples acquired at 0, 1.5, 3.5 and 5 h, respectively, emphasizing the anisotropic process of oxidizing gold nanobottles, that takes preferentially at the nanobottle rims with lower density of surfactants and higher surface energy.

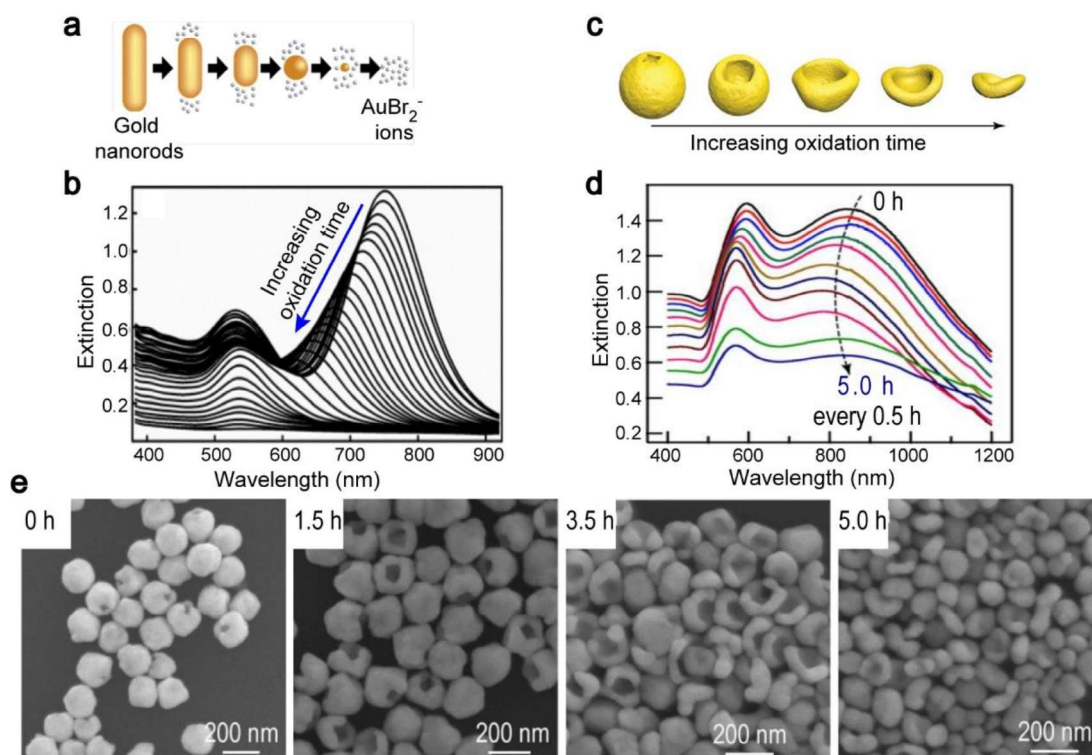


**Figure 1.15** Examples of selective oxidation. (a–b) Selectively oxidizing gold nanorods.<sup>[101]</sup> (a) The schematic illustrates the evolution of gold nanorods with the oxidation time. (b) Extinction spectra of gold nanorods measured every 1 min during oxidation process. (c–e) Selective oxidation of gold nanobottles.<sup>[106]</sup> (c) Schematic for

the oxidation process of gold nanobottles. (d) Extinction spectra of gold nanobottles acquired every 30 min after the injection of hydrogen peroxide. (e) SEM images of gold nanobottles acquired at 0, 1.5, 3.5, and 5 h, respectively.

## 1.4 Applications of Plasmonic Nanostructures

Plasmonic nanostructures possess many outstanding advantages, which have already been proposed and demonstrated by applying in a large number of fields, ranging from biomedical techniques to the development of alternative energy sources, photo-assisted chemical reactions, and information technology.<sup>[49, 107–109]</sup> Figure 1.16 aims to emphasize the broad applications of plasmonic nanostructures based on their different properties.<sup>[49]</sup> The strong light absorption of plasmonic nanostructures enables them to be applied in nanofluidic solar steam generation, photothermal treatment, surface-enhanced fluorescence and so on. On the other hand, the high scattering ability of plasmonic nanostructures opens up opportunities to develop the applications in bioimaging and diagnosis, biosensing, and surface-enhanced Raman spectroscopy (SERS). In this section, I will highlight some important applications that are more related to this thesis.

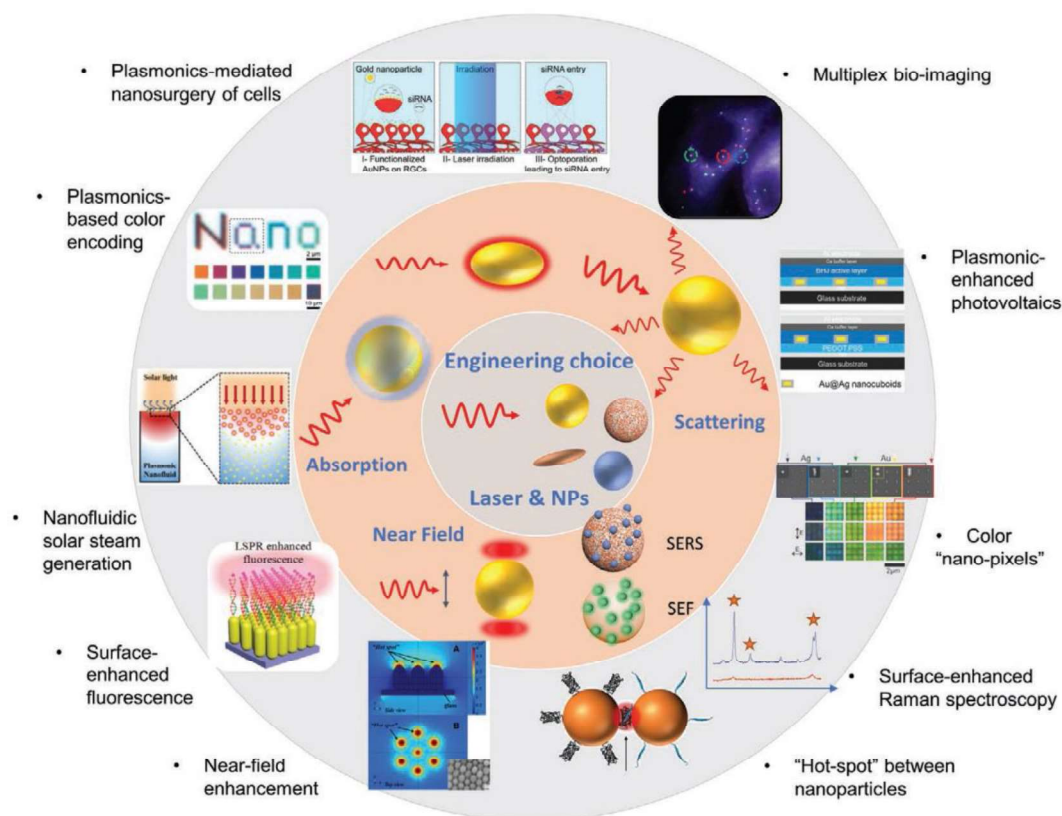


**Figure 1.16** Schematic illustrating the applications of plasmonic nanostructures.<sup>[49]</sup>

### 1.4.1 Plasmonic sensing

The LSPR of noble metal nanostructures is not only determined by shape, size, and composition but also highly sensitive to the refractive index of the environment.<sup>[110–112]</sup> Generally, the plasmonic peak gradually redshifts with the refractive index of the environment increases. The alteration can be easily detected by monitoring the extinction spectra using a UV/Vis/NIR spectrophotometer or scattering spectra employing a dark-field spectrometer. Therefore, plasmonic nanostructures are widely exploited for the design of biomedical and chemical sensors in solution or on a substrate.<sup>[107]</sup>

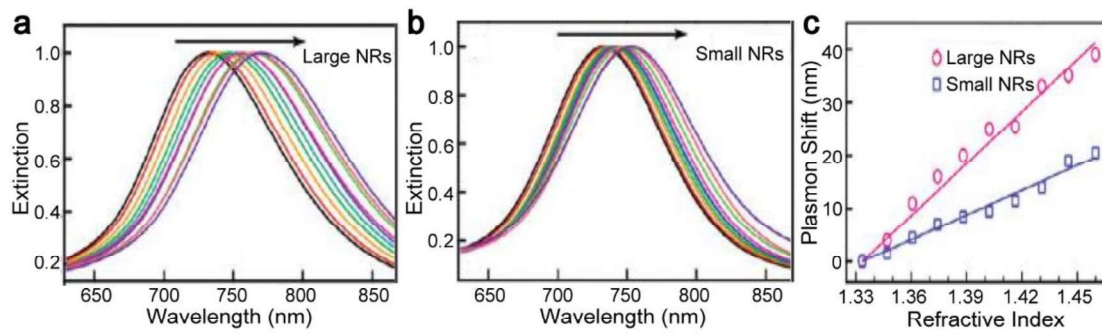


**Figure 1.17** The variations of extinction spectra of gold nanorods with increasing the refractive index of the surrounding medium.<sup>[116]</sup> (a–b) The variations of normalized extinction spectra of large and small gold nanorods with the refractive index increasing, respectively. The change in refractive index is realized by mixing water and glycerol at different ratios. (c) Plotting the longitudinal plasmon shift versus the refractive index of surrounding medium for large and small gold nanorod samples.

Two parameters are commonly utilized to evaluate and compare the performance of plasmonic sensors.<sup>[113]</sup> The first one is the bulk refractive index sensitivity ( $S$ ) reflecting the ability to detect changes in the refractive index. The relationship between the plasmonic peak position and the surrounding refractive index is approximately linear.<sup>[114]</sup> The sensitivity value is thus determined by the following equation<sup>[113–115]</sup>:

$$S = \frac{\Delta\lambda}{\Delta n} \quad (1.1)$$

where  $\Delta\lambda$  is the peak position changes in the extinction/scattering spectra and  $\Delta n$  is the changes in the corresponding refractive index of the environment. Figure 1.17 is the sensing examples of gold nanorods with two different sizes.<sup>[116]</sup> Both of them have

well-linear fitted plots between plasmon shift and refractive index of surrounding medium but the slopes of the two plots are different (Figure 1.17c). The results demonstrated that the refractive index sensitivity of gold nanorods is largely influenced by their size. Besides size, the sensitivity also depends on the morphology of the nanostructure, as shown in the table that the sensing examples of different gold nanostructures with different morphologies (Table 1.1).<sup>[117]</sup> Among these particles, gold nanospheres possess the lowest refractive index sensitivity while gold nanobranches with many sharp tips exhibit the highest refractive index sensitivity due to the sharp tips possess high electromagnetic field enhancement on the surface.<sup>[111]</sup> Therefore, size and morphology are important factors for determining the refractive index sensitivity.

**Table 1.1** The morphologies, sizes, plasmon wavelengths, index sensitivities, and figure of merits for different gold nanoparticles.<sup>[117]</sup>

Au nanoparticles	length <sup>a</sup> (nm)	diameter <sup>b</sup> (nm)	aspect ratio <sup>c</sup>	plasmon wavelength <sup>d</sup> (nm)	index sensitivity <sup>e</sup> (nm/RIU)	figure of merit
nanospheres		15 (1)		527	44 (3)	0.6
nanocubes	44 (2)			538	83 (2)	1.5
nanobranches	80 (14)			1141	703 (19)	0.8
nanorods	40 (6)	17 (2)	2.4 (0.3)	653	195 (7)	2.6
nanorods	55 (7)	16 (2)	3.4 (0.5)	728	224 (4)	2.1
nanorods	74 (6)	17 (2)	4.6 (0.8)	846	288 (8)	1.7
nanobipyramids	27 (4)	19 (7)	1.5 (0.3)	645	150 (5)	1.7
nanobipyramids	50 (6)	18 (1)	2.7 (0.2)	735	212 (6)	2.8
nanobipyramids	103 (7)	26 (2)	3.9 (0.2)	886	392 (7)	4.2
nanobipyramids	189 (9)	40 (2)	4.7 (0.2)	1096	540 (6)	4.5

<sup>a</sup> For nanocubes, the edge length was measured. For nanobranches, the length from the center to the branch tip was measured. The numbers in the parentheses are standard deviations. <sup>b</sup> For nanobipyramids, the diameter at the middle was measured. <sup>c</sup> The ratio between the length and the diameter. <sup>d</sup> Measured when Au nanoparticles are dispersed in aqueous solutions. For nanobranches, it is the longer plasmon wavelength. For nanorods and nanobipyramids, it is the longitudinal plasmon wavelength. <sup>e</sup> For nanobranches, it is the refractive index sensitivity of the longer-wavelength plasmon peak. For nanorods and nanobipyramids, it is the index sensitivity of the longitudinal plasmon resonance peak.

The other important parameter is figure of merit (*FOM*) which is used to compare the precision of the resonance minimum we can measure. The *FOM* is defined as normalizing refractive index sensitivity by the full width at half maximum (*FWHM*). The value of *FOM* is thereby calculated as<sup>[110, 113–115]</sup>:

$$FOM = \frac{S}{FWHM} \quad (1.2)$$

Generally, a good sensor not only needs to have high sensitivity, but also needs to have a large value of *FOM*. In table 1.1, although nanobranches show very high sensitivity, the value of *FOM* is very low due to the wide LSPR peak caused by the larger number of sharp tips.<sup>[118]</sup> Additionally, although larger nanostructures usually have higher sensitivities, their plasmonic peaks are broader due to the radiative damping and multipolar excitations which finally results in a lower *FOM* value.<sup>[114]</sup>

Understanding the two parameters for characterizing the performance of plasmonic sensors facilitates the development of a wide range of sensors. In 2002, Nath and coworkers developed a gold nanosphere based sensor to detect the quantification of biomolecular interaction.<sup>[119]</sup> In their work, they first evaluated the sensing capability of gold nanospheres by monitoring the LSPR peak shift when the refractive index of the surrounding solution changes with the help of UV/Vis/NIR spectrophotometer. The result gives a sensitivity of 76.4 nm/RIU (refractive index unit) which encouraged the authors to immobilize gold nanospheres on a glass to detect streptavidin-biotin as a function of time and a dramatically time-dependent increase was found. Similar plasmonic sensor configuration was prepared by Marinakos and coworkers,<sup>[120]</sup> they immobilized gold nanorods onto a mercaptosilane-modified glass substrate as the sensor and exhibited higher sensitivity (252 nm/RIU).

Single-particle based plasmonic sensor was achieved by employing a dark-field optical microscopy system. The single-particle based sensor has many advantages, such as lower detection limit, higher sensitivity, and less volume of samples, in comparison with other types of nanoparticle based sensors.<sup>[121–123]</sup> The potential of the single-particle sensors can be exemplified with the work of Lambertz and coworkers where they utilized single gold nanorod as sensor to monitor the local concentration of MinDE protein in real time.<sup>[124]</sup> The individual gold nanorod covered by lipid bilayer are visible under the dark field microscopy, shown as red dots in Figure 1.18a. This allows the scattering spectrum of the single gold nanorod below the lipid bilayer to be obtained and hence it is possible to observe how the peak position in the scattering spectrum red/blue shift as the proteins attach/detach on the surface of the single gold nanorod, since the attachment/detachment leads to the refractive index changing. They also showed how the wavelength changes as a function of time (Figure 1.18b), hence it is able to show the dynamics of the biological processes with real time and define different stages of protein attachment (Figure 1.18c).

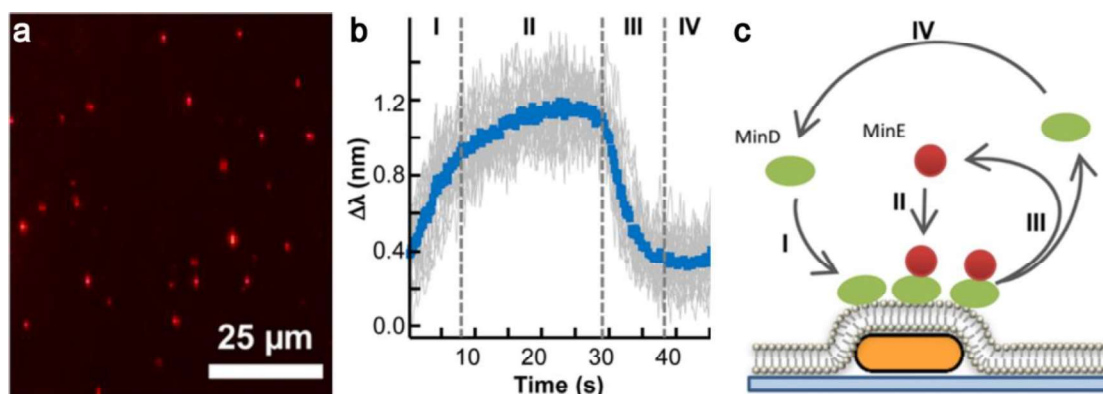


**Figure 1.18** The example of using single gold nanorod as sensor.<sup>[124]</sup> (a) Dark field scattering image of gold nanorods positioned below the lipid bilayer. (b) The wave profile of a single gold nanorod as sensor averaged over 26 individual cycles. The blue line is the average line and the gray lines are the individual cycles. The wave profile displays Langmuir-type characterize and are divides into four stages. (c) The process of MinDE attaching/detaching on Membranes.

The different responses caused by the changes in the refractive index can also be used as chemical sensors, directly or indirectly. For example, Tsukruk group developed a pH-sensitive sensor using gold nanorods covered with polyaniline (Figure 1.19a).<sup>[125]</sup> In this work, it takes advantage of the significant difference in refractive index of polyaniline at different forms changing from emeraldine salt to pernigranline base by increasing the pH of the surrounding medium (Figure 1.19b). The authors specifically chose gold nanorods due to their high refractive index sensitivity and large *FOM*. As shown in Figure 1.19c and d, the longitudinal LSPR peak exhibits a dramatic shift when the pH of surrounding medium is altered. It is worth emphasizing that the significant LSPR redshift is reversible ensuring the recycling and reproducible ability of the plasmonic sensors for detecting pH change.

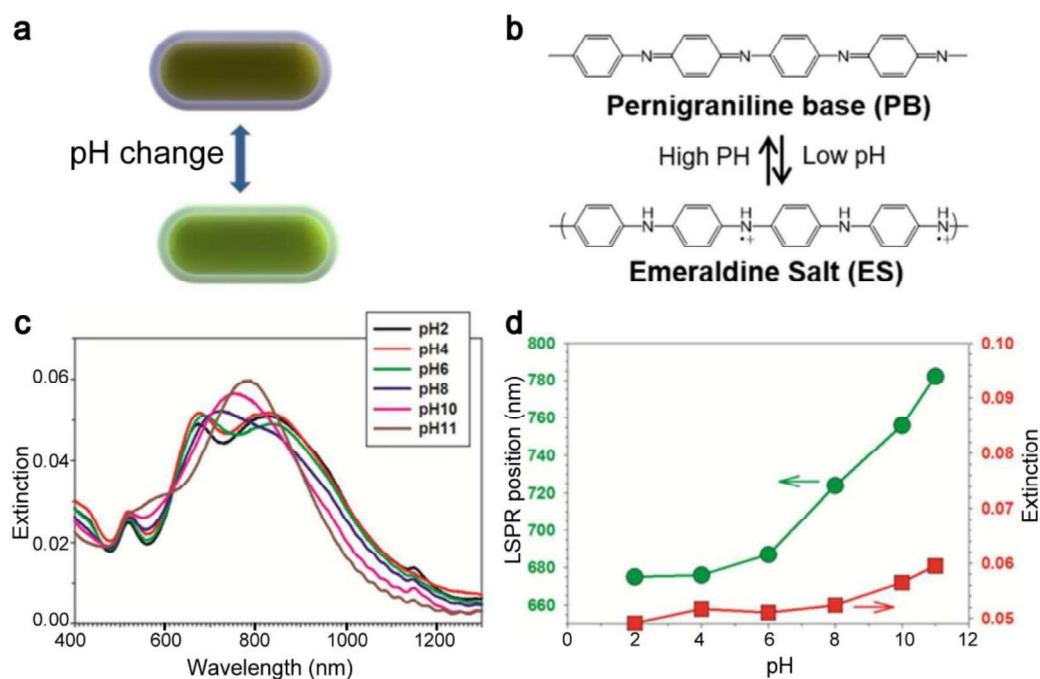


**Figure 1.19** Gold nanorod@polyaniline core/shell nanostructure sample for pH detecting sensor.<sup>[125]</sup> (a) The schematic of gold nanorod@polyaniline core/shell nanostructure for pH detecting sensor with reversible response. (b) Chemical structure of pernigraniline base and emeraldine salt states of polyaniline. (c) The extinction spectra of gold nanorod@polyaniline core/shell nanostructure with an 8 nm shell of polyaniline at a variety of surrounding pH. (d) The plots of LSPR position and extinction intensity as a function of pH, respectively.

These examples are just a few to highlight the achievements of plasmonic sensors and encourage researchers to invest more time and efforts in the development of sensors with higher performance, simpler detecting process and easier preparation method. Among the nanoparticles of interest, gold trioctahedrons are particularly exceptional nanostructures with high refractive index sensitivities, and this thesis will focus on the synthesis, structural characterization and their sensing performance in Chapter 3.

### 1.4.2 Raman spectroscopy

Raman spectroscopy is an analytical technique based on Raman scattering, the inelastic scattering of light, which was initially predicted by an Austrian physicist named Adolf Smekal in 1923 and demonstrated by an Indian physicist named Chandrashekhara Venkata Raman in 1928, from whom the technique is named

after.<sup>[126]</sup> Specifically, when a photon of incident light interacts with a molecule, a scattered photon whose energy equals either the difference or the sum of the energy of the incident photon and that of a molecular energy level is generated.<sup>[126–128]</sup> As illustrated in Figure 1.20, when the interaction takes place between the incoming photon and a molecule in its vibrational ground state ( $v = 0$ ), the molecule is first excited to a higher or virtual energy state and then relaxes back to the first vibrational state ( $v = 1$ ) by radiating a scattered photon of lower energy. This process is an inelastic scattering known as Stokes Raman scattering. On the other hand, anti-Stokes Raman scattering occurs when the molecule is excited from the first vibrational state ( $v = 1$ ) and relaxes back to the vibrational ground state ( $v = 0$ ). The energies of the Stokes and anti-Stokes Raman scattering processes are symmetric with respect to the energy of the elastic scattering known as Rayleigh scattering, which takes place when the molecule is excited from the vibrational ground state and relaxes back to the same ground state without any energy change, and hence this phenomenon does not provide any information about the molecule for investigation. On the contrary, both Stokes and anti-Stokes Raman scattering processes can provide detailed chemical and structural information on the molecule through the energy changes in the scattered photons. Consequently, Raman spectroscopy is widely applied in many research fields ranging from analytical chemistry to the characterization of various structures and materials such as biomolecules, minerals and food.<sup>[129–130]</sup>

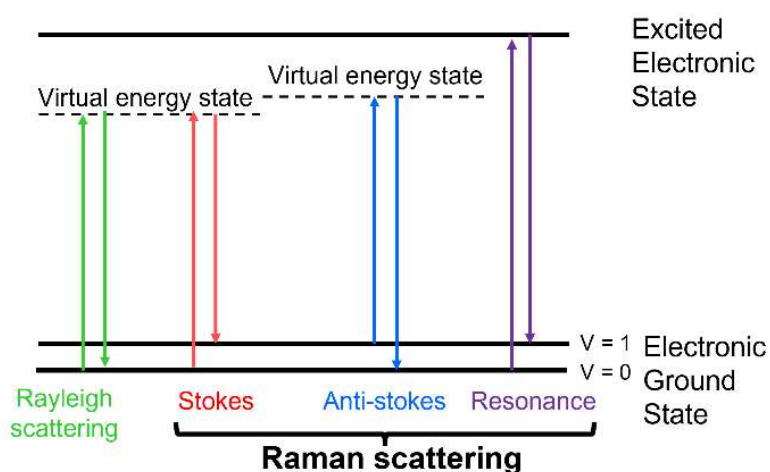


**Figure 1.20** Energy diagram illustrating Rayleigh and Raman scattering.

The instrumentation for carrying out Raman spectroscopy typically includes a light source (laser), monochromator, sample holder, and CCD detector (Figure 1.21a).<sup>[127, 131]</sup> The laser illuminates the sample and then the interaction between the laser and the

sample results in scattered light with energy different from that of the incident laser light. The scattered light is analyzed by a spectrometer and recorded by a CCD camera, providing the Raman spectrum (Figure 1.21b). The  $x$  axis of the spectrum shows the wavenumber ( $\bar{\nu}$ ), which is proportional to the energy difference between the incident photon and scattered photon known as Raman shift. The Raman shift is thereby calculated by the following expression<sup>[132]</sup>:

$$\bar{\nu} = \frac{1}{\lambda_L} - \frac{1}{\lambda_S} \quad (1.3)$$

where  $\lambda_L$  and  $\lambda_S$  are the wavelengths of the incoming photons and scattered photons, respectively. The position of Raman peak is determined by the nature of the molecule bond, for example, heavier atoms involved lower frequency of vibrations lead to lower Raman shift.<sup>[132–134]</sup> Since molecules may possess many molecular bonds, such as C=C, C-C, C-H, O-H, and these bonds can be all excited, giving as a result that the Raman spectrum of each molecule is unique, like fingerprint.<sup>[131]</sup> The  $y$  axis of Raman spectrum shows the intensities of Raman peaks which depend on the type and concentration of the molecular bonds involved in vibration as well as the property of the scattering materials.<sup>[132]</sup>

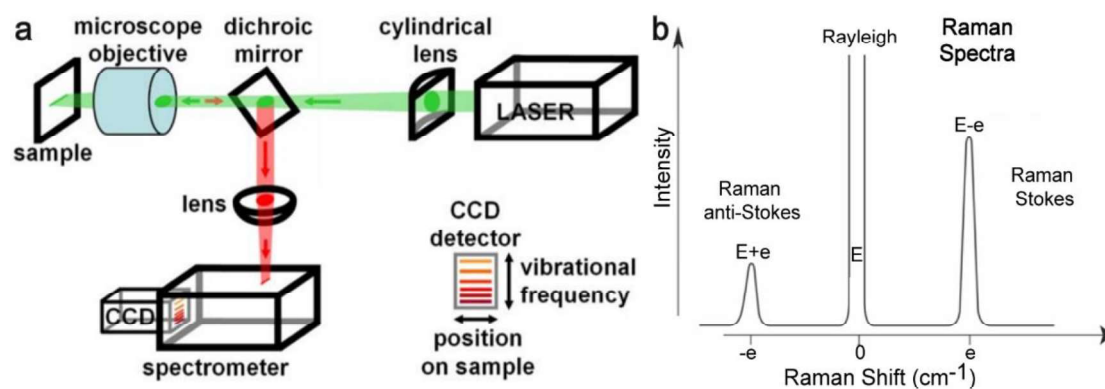


**Figure 1.21** The principles of Raman spectroscopy. (a) The schematic of Raman spectroscopy.<sup>[131]</sup> (b) Schematic illustrating the Raman spectrum. The peak at  $0 \text{ cm}^{-1}$  is Rayleigh scattering, the right and left peaks are Stokes Raman scattering and anti-Stokes Raman scattering, respectively.<sup>[132]</sup>

The Raman peaks and intensities can be used for both quantitative and qualitative analysis. However, the intensity of Raman peak is very low because of the low efficiency of the Raman scattering process, typically, only one Raman scattered photon in  $10^8$ – $10^{10}$  incoming photons.<sup>[131]</sup> In order to amplify the Raman response and thereby open the possibility of detecting molecules at a trace level, many efforts have

been dedicated to improving the Raman signal by combining Raman spectroscopy with other analytical techniques such as microchromatography, high-performance liquid chromatography and scanning probe microscopy (SPM) as well as by using plasmonic nanostructures.<sup>[127]</sup> Among them, a simple and straightforward method is using plasmonic nanostructures. In the following part, I will focus on introducing SERS and tip-enhanced Raman spectroscopy (TERS) which are highly related with the objectives of this thesis.

#### **1.4.2.1 Surface-enhanced Raman spectroscopy**

The phenomenon of SERS was firstly reported in 1974: an unexpected increase of the Raman signal was observed when Fleischmann and coworkers put a layer of pyridine on the surface of a rough silver electrode.<sup>[135]</sup> The million-fold enhancement was originally attributed to the greater number of pyridine molecules adsorbed on the surface, but later studies showed that the enhancement arose from the rough surface with surface plasmon excitation.<sup>[136–137]</sup> These pioneer research works played an important role in the development of analytical technology for detecting a few numbers of or even single molecule(s). As a matter of fact, these works offered a route to overcome the disadvantage of low efficiency of traditional Raman spectroscopy. In addition, Raman spectroscopy has fingerprint, label-free and non-destructive features. These significant advantages have drawn extensive attention in different research fields, which in turn gave rise to the fast development of SERS.

In the following part, I will briefly introduce the two widely accepted SERS mechanisms: chemical enhancement and electromagnetic enhancement, then I will provide a description of the factor for evaluating SERS performance, I will finally discuss the variables influencing SERS performance.

#### ***SERS mechanisms***

Since the discovery of SERS phenomenon, the research on enhancement mechanisms has never stopped. Chemical enhancement and electromagnetic enhancement are the two widely accepted mechanisms. The chemical enhancement mechanism is related to the chemical interactions between the adsorbed molecules and metal surface.<sup>[138–141]</sup> Firstly, compared with the free state molecules, the formation of chemical complexation between adsorbed molecule and the metal generally changes the spatial orientation, the Raman polarizability, and the symmetry of the molecule.

These changes contribute to the enhancement of certain vibrational modes. Secondly, the Raman scattering cross-section of the molecule changes since the occurrence of charge transfer between molecule and metal leads to a change in the polarizability of the molecule. In addition, if the laser wavelength matches with the electronic transitions of the formed molecule-metal complex, charge transfer resonance will happen and result in the enhancement of the Raman scattering, this is so called resonance Raman scattering (Figure 1.20). However, the enhancement contributed by chemical enhancement is generally lower than a factor of  $10^3$ .

In contrast, the electromagnetic enhancement usually has a large contribution to overall enhancement of SERS. The process of electromagnetic enhancement is commonly divided into two steps, corresponding to the local field enhancement and the radiation enhancement, respectively (Figure 1.22).<sup>[141–143]</sup> As discussed in Section 1.1, the LSPR occurs when the incident light interacts with a noble metal nanostructure. The confined light can greatly enhance the local electromagnetic field. A small change in the local electromagnetic field can induce a considerable variation in the SERS enhancement because the overall enhancement caused by electromagnetic field ( $G_{ex}$ ) is proportional to the second power of the local electromagnetic field enhancement:

$$G_{ex} = \frac{|E_{Loc}(\omega_0)|^2}{|E_0(\omega_0)|^2} \quad (1.4)$$

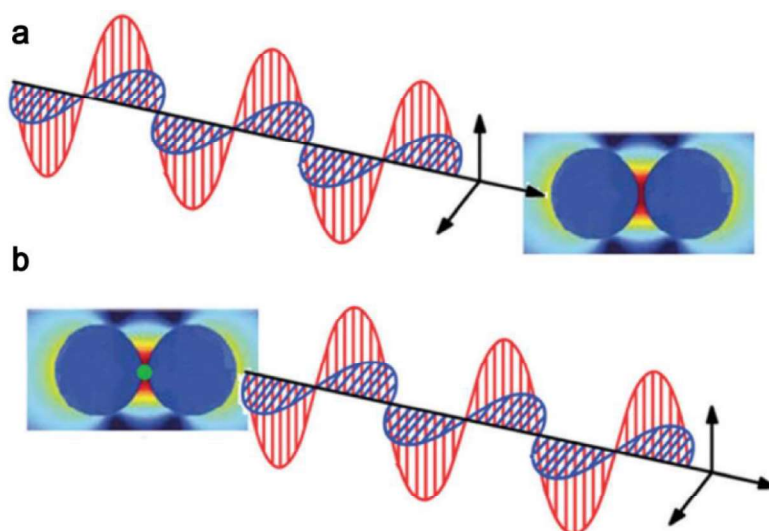


**Figure 1.22** Schematics showing the two-step electromagnetic enhancement mechanism.<sup>[142]</sup> (a) Local field enhancement. (b) Radiation enhancement.

Moreover, the power emission of an oscillating dipole is largely influenced by its surrounding environment. For example, a molecule displays a different radiation pattern when excited in vacuum in comparison with excited at the interface among various materials. Similarly, when the molecules interact with noble metal nanostructures, the Raman polarizability of molecules are roughly magnified with one or three orders than that of molecules in the free state. The interaction between molecules and noble metal nanostructures therefore results in the mutual excitation of the Raman polarizability by the local electromagnetic field. During this process, the Raman signal is enhanced with a factor ( $G_R$ ) as follows:

$$G_R = \frac{|E_{Loc}(\omega_R)|^2}{|E_0(\omega_R)|^2} \quad (1.5)$$

When the vibrational frequency of a Raman mode ( $\omega_R$ ) is approximately equal to that of incoming light ( $\omega_0$ ), the SERS enhancements arising from local field enhancement and radiation enhancement are comparable. Hence, the overall SERS enhancement produced by the electromagnetic enhancement ( $G$ ) is determined by the fourth power of the electromagnetic field:

$$G = G_{ex} G_R = \frac{|E_{Loc}(\omega_0)|^4}{|E_0(\omega_0)|^4} \quad (1.6)$$

Therefore, the large enhancement of local electromagnetic field leads to the SERS signal enhanced with many orders of magnitude.

### ***SERS enhancement factor***

The SERS enhancement factor ( $EF$ ) is an important parameter which is commonly utilized to evaluate the SERS enhancement ability of a metal nanostructure. It is defined as the ratio between the SERS intensity normalized by the number of molecules and the normal Raman peak intensity of a single free molecule.<sup>[128, 139, 141]</sup> It can be calculated by:

$$EF = \frac{I_{SERS}/N_{SERS}}{I_{RS}/N_{RS}} = \frac{I_{SERS}N_{RS}}{I_{RS}N_{SERS}} \quad (1.7)$$

where  $I_{SERS}$  and  $I_{RS}$  are the intensities of the SERS peak and normal Raman peak, respectively, determined from the Raman spectra. It is worth mentioning that the *FWHM* of a SERS peak is generally broader than that of the normal Raman peak since the states of molecules on the metal surface are more heterogeneous than the free molecules, in addition to the molecules which have strong and complicated

interactions like hydrogen bonding with the surrounding molecules. For the above-mentioned reason, it is more accurate to use the peak area as the intensity value when evaluating SERS performance.  $N_{SERS}$  and  $N_{RS}$  are the numbers of molecules contributing to SERS and normal Raman spectra, respectively.  $N_{SERS}$  can be estimated by knowing the number of nanostructures ( $R$ ), the geometric surface area of the nanostructure ( $A$ ), and the surface area occupied by the molecule ( $\sigma$ ). The relationship among them is:

$$N_{SERS} = R \times \frac{A}{\sigma} \quad (1.8)$$

Since  $I_{RS}$  can be obtained by two different ways, either by directly measuring the solution or detecting solid sample dried from solution, the method for calculating  $N_{RS}$  is different. With regard to the solution sample,  $N_{RS}$  can be determined from the following expression:

$$N_{RS} = C_{RS} \times N_A \times V = C_{RS} \times N_A \times A \times h \quad (1.9)$$

where  $C_{RS}$  is the concentration of the molecules,  $N_A$  is the Avogadro constant ( $6.02 \times 10^{23} \text{ mol}^{-1}$ ),  $A$  represents the illumination area or the size of laser spot, and  $h$  is the thickness of solution layer near the “ideal focal plane” depends on the numerical aperture (NA) and pinhole size of the objective. As for solid sample, it is obtained by drying a drop of solution with a known concentration loading on a substrate.  $N_{RS}$  can be calculated with known the following parameters: the radius of laser spot ( $r$ ), the thickness of the sample layer ( $l$ ), and the sample density ( $\rho$ ). Therefore:

$$N_{RS} = \rho \times \pi r^2 l \quad (1.10)$$

### ***Factors influencing the SERS enhancement***

As above discussed, SERS enhancement is largely determined by the electromagnetic field, therefore, the variables affecting LSPR properties, such as the morphology, size, and composition of noble metal nanostructures, obviously influence the SERS enhancement as well. Except for these factors, the SERS enhancement can be further improved by forming gap modes. When two noble metal nanostructures are very close (normally less than 10 nm), these two particles can form dipole-dipole coupling which induces a strongly enhanced electromagnetic field between them.<sup>[144]</sup> This coupling effect is significantly dependent on the distance, for example, the value of  $EF$  can be dramatically decreased from about  $10^{10}$ – $10^{11}$  to around  $10^7$ – $10^8$  by increasing the distance between two silver particles from 1 nm to 5.5 nm.<sup>[145]</sup>

Similarly, the distance between the molecule and substrate also greatly affects the enhancement of Raman signal. Many works have been devoted to the study of the distance-dependence enhancement by coating polymers, metal oxide, or long chain thiols on the metal nanostructures to tune the separate distance between detected molecules and the nanostructures.<sup>[146–148]</sup> Furthermore, inducing aggregation of nanostructure colloid can increase the SERS signal as well.<sup>[149–151]</sup> For example, adding a certain amount of salt (i.e., NaCl, KCl, MgSO<sub>4</sub>, etc.) into colloid can induce aggregation and then enhanced the Raman signal.<sup>[148, 152–153]</sup> However, it is hard to control the aggregation process and difficult to reproduce the results.

Consequently, SERS is a powerful technique with high sensitivity, fingerprint, label free and non-destructive advantages in many research areas like chemistry, biology and biomedicine, and so on. However, the development of current scientific research requires SERS techniques to be capable of analyzing even more complicated systems. Many efforts are still needed to continuously develop high performance SERS technique for complex applications, from understanding the fundamental mechanism and optimizing nanostructure to improving sensitivity and stability. Improving the enhancement ability and stability of SERS substrates by simple and costless preparing methods are still the essential objectives for further enhancing SERS. During my PhD research work, I mainly focus on improving these two factors.

#### 1.4.2.2 Tip-enhanced Raman spectroscopy

SERS technique solved the low sensitivity drawback of Raman spectroscopy, but it cannot solve the low spatial resolution problem. The spatial resolution of traditional optical microscopy is restricted by the optical diffraction-limit. According to Heisenberg's uncertainty principle, the spatial resolution ( $\Delta x$ ) is the smallest distance for unambiguously distinguishing two sources in an optical observation. Abbe proposed that the resolution is related with the wavelength of incoming light and the  $NA$  value of the objective.<sup>[154–156]</sup> As follows:

$$\Delta x = \frac{0.61\lambda}{NA} \quad (1.11)$$

Under the best practical conditions, it turns out that the value of spatial resolution is close to half of the incident light wavelength. Hence, the highest resolution is about 200 nm for visible light, a value insufficient for most of the nanoscience applications. To overcome the low spatial resolution issue limited by the optical diffraction, new

techniques were invented. In 2000, four research groups independently developed the tip-enhanced Raman scattering (TERS) techniques which combine Raman spectroscopy with the SPM techniques to provide Raman spectroscopy with the high spatial resolution.<sup>[157–160]</sup> Figure 1.23 shows the schematic of the typical configuration of TERS technique.

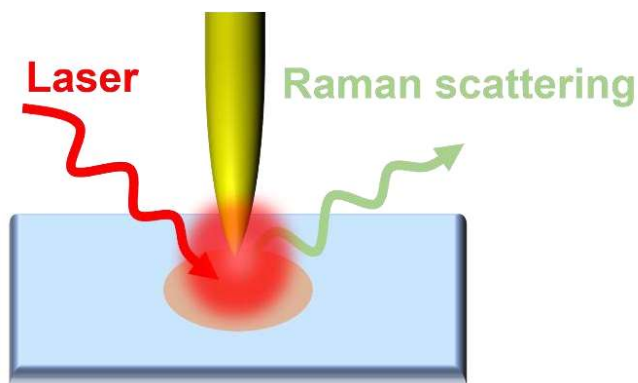


**Figure 1.23** Schematic illustrating the typical configuration of TERS technique.

In the following part, I will give a detailed description on TERS technologies, including the mechanisms for the great enhancement and high spatial resolution in TERS techniques, the probes used in TERS technologies and the applications of liquid TERS systems.

### ***TERS mechanisms***

The mechanism of TERS enhancement is similar to that of SERS enhancement, including chemical enhancement and electromagnetic enhancement. TERS is based on the use of a very sharp tip (the apex size is around 10–50 nm) which plays three different essential roles in the local field enhancement.<sup>[161–162]</sup> The first one is the “lighting rod” effect, which is an essentially non-resonant process. As for a conductive and sharp nanotip under illumination, the surface charges can be concentrated at the tip. This process is mainly determined by the electrical conductivity of the tip materials at the frequency of applied light during experiment. The second contribution arises from the excitation of LSPR in noble metal nanostructures. Thirdly, when the length of optical antenna (an optical antenna is referred to an object which can convert the freely propagating optical radiation into localized energy and vice versa) is equal to a multiple of one-half of the light wavelength, length-related antenna resonances will be generated.

Furthermore, the distance between the tip apex and substrate is able to be accurately controlled down to a few nanometers or even subnanometer by using an SPM feedback system, thus resulting in significantly electromagnetic field coupling between the tip and metal substrate, this is so called gap mode effect. This gap mode can further enhance the intensity and confinement of the electromagnetic field.<sup>[128, 154]</sup> It should be noted that the Raman responses originate only from the molecules located directly beneath the apex of the tip as the electromagnetic field is confined to this narrow area. The spatial resolution of TERS thereby can approach (sub)nanometers.<sup>[163]</sup> Moreover, self-interaction can happen when the distance between tip apex and molecule is very small and comparable to the molecular size. This small gap size causes super strong inelastic scattering of the molecule, so the contributions from molecular responses to both Raman scattered field and excitation must be considered.<sup>[164]</sup> Consequently, the Raman responses, including the intensity of Raman signal and spatial resolution, can be strongly affected by the self-interaction process.<sup>[128, 161]</sup>

However, until today, the mechanism of subnanometer spatial resolution in the TERS technique is still under discussion.

### ***The tips used in TERS technique***

In a TERS setup, tip plays an essential role in determining both the enhancement and the spatial resolution. Additionally, the quality and repeatability of TERS measurements are enormously related with the efficiency and stability of tip. In order to further develop and apply TERS, it is critical to fabricate tips with high stability and large TERS enhancement. As mentioned in Section 1.2, the composition, size and morphology of nanostructures highly influence the LSPR properties. Hence, these factors, considered as parameters of the TERS tips, strongly affect the  $EF$  and spatial resolution in TERS measurements. A metal or metal-coated tip is generally applied in TERS and the metal is mainly gold or silver since their LSPR wavelength can match with the wavelength of incident light.<sup>[162]</sup> At present, three types of SPM tips are widely used in TERS system, which are atomic force microscopy (AFM) tip, shear force microscopy (SFM) tip, and scanning tunneling microscopy (STM) tip (Figure 1.24).<sup>[165]</sup>

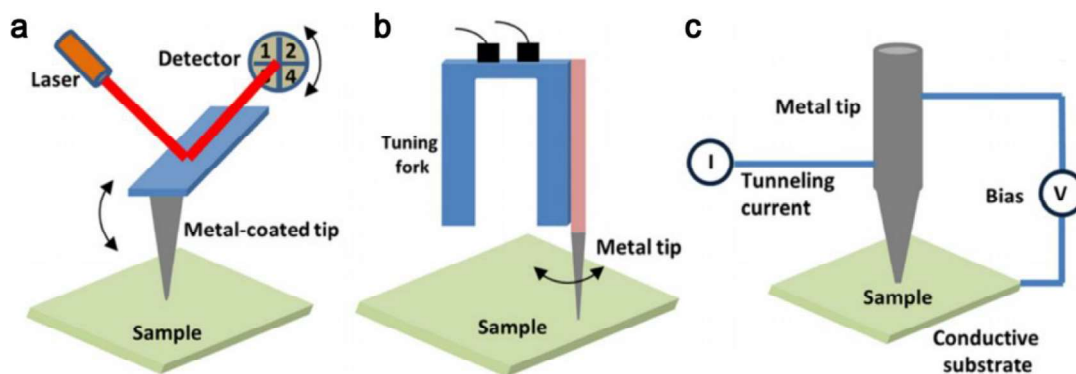


**Figure 1.24** Schematics of TERS techniques based on different SPM feedbacks.<sup>[165]</sup> (a) AFM-based TERS system. (b) SFM-based TERS system. (c) STM-based TERS system.

In AFM systems, a commercially standard semiconductor cantilever probe (Si or Si<sub>3</sub>N<sub>4</sub>) with an apex diameter of approximately 5 nm or less is employed for obtaining information. Such type of tip can be used in AFM-based TERS technique after coating with high purity gold or silver layers. The thermal evaporation in a high vacuum environment and electroless plating techniques are the two main methods to deposit metallic films on the tip.<sup>[155, 166]</sup> The thickness of the covered layers can be controlled during coating. Generally, the thickness of the coated layer is controlled at several tens of nanometers and the apex diameter of the metal-coated tip is controlled at around 20–50 nm.<sup>[154]</sup>

In STM techniques, a solid gold probe with smooth surface is commonly used as the tip for measurement. The simplest and most reproducible way for fabricating STM tips is electrochemical etching of gold wires.<sup>[167]</sup> During the etching process, the parameters like voltage, temperature and cut-off current determine the apex size. Normally, the apex size is around 20–40 nm. A gold substrate is applied in STM system as well, which can create the gap mode effect when the gold tip approaches to the substrate, resulting in a strong hot spot within the nanogap.<sup>[155]</sup> Other methods, like a focused ion beam, can be successfully used to fabricate TERS tips as well, however, these methods are typically time-consuming, too expensive or with very poor reproducibility, which are not suitable for the fabrication of large quantities of tips.<sup>[154, 162, 166]</sup> In addition, the electrochemical etching method can be used to produce silver tips with high TERS performance as well, but it is susceptible to oxidation in air.

Although SFM is a distinct type of AFM technique, almost all types of probes can be utilized in SFM based TERS setup.<sup>[162, 168]</sup> Thus, the solid gold or silver tips obtained by electrochemically etching gold or silver wires are suitable for the SFM-

based TERS techniques.<sup>[155]</sup> Furthermore, the etched tungsten probes covered with gold or silver are applied in SFM-based TERS as well.<sup>[169–170]</sup> Moreover, coating a layer of metal on glass fibers or attaching metal nanoparticles to the apexes are also suitable tips for SFM-based TERS techniques.<sup>[171–172]</sup>

### ***TERS in liquid***

In the recent twenty years, tremendous progress has been made in the development of TERS technology. The majority of TERS technologies have been performed in ambient air or ultrahigh vacuum environment. However, it is difficult to apply the TERS techniques in liquid and thus these TERS techniques are not suitable for most biological and electrochemical samples since the samples should be kept in liquid environments, such as biological cells and tissues must be remained in aqueous buffers. It is therefore necessary to develop liquid TERS techniques for obtaining information from biological samples while maintaining them in alive state as well as keeping their physiological activities at the same time.<sup>[173]</sup>

The first challenge for implementing TERS in liquid is the distortion of the optical path when the incident laser passes from air to solution due to the difference in refractive index.<sup>[166]</sup> In order to improve the excitation and thereby enhance the detection sensitivity, minimizing the degree of optical distortion is necessary. There are mainly three different illumination geometries for focusing incoming laser to the apex of a TERS tip in the liquid environment, which are bottom illumination, side illumination and top illumination (Figure 1.25a–c). Among these three illumination methods, the most convenient one is the bottom illumination geometry. The optical distortion is able to be avoided in this bottom illumination geometry since the irradiation light passes from the bottom side and focuses into the gap between sample and tip without passing through the thick liquid layer. By using this geometry, the first solid/liquid TERS measurement was reported by Zenobi's group in 2009. The schematic of their setup is illustrated in Figure 1.25d, a monolayer of thiophenol on a thin transparent gold substrate was efficiently detected.<sup>[173]</sup>

However, the bottom illumination method is limited in measuring the samples with transparent substrates. The limited choice of transparent substrates consequently narrows the application range of bottom illuminated TERS. The side and top illumination geometries are suitable for characterizing samples with opaque substrates, which make the applications of these two kinds of illuminations based TERS

techniques more versatile without considering the substrate material and thickness. However, it must be noted that the optical path suffers severe distortion as the incident laser must pass through air to liquid. In addition, the formation of a meniscus liquid layer caused by the capillary force can further distort the optical path. In 2016, the research group of Domke reported a liquid TERS setup with side illumination configuration, they managed to control the thickness of the liquid layer to only several millimeters for minimizing the optical distortion (Figure 1.25e).<sup>[174]</sup> In the same year, Ozaki and coworkers put a drop of liquid with a volume of 5–10  $\mu\text{L}$  on the surface of the sample to control the liquid layer thickness in a top illumination based TERS system (Figure 1.25f).<sup>[175]</sup>

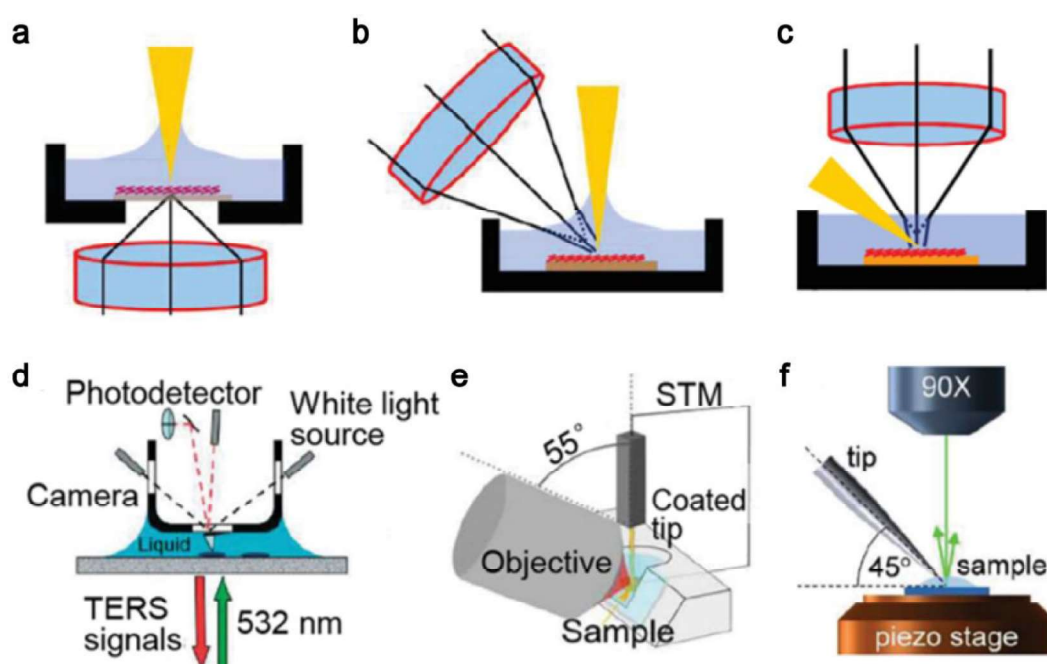


**Figure 1.25** Schematics illustrating the optical designs of applying TERS techniques in liquid.<sup>[166]</sup> (a–c) Schematics of TERS setups with bottom illumination geometry, side illumination geometry and top illumination geometry, respectively. (d) Schematic showing the AFM-TERS system in a liquid environment with a bottom illumination geometry. (e) Schematic displaying the STM-TERS system in solution based on side illumination geometry. (f) Schematic exhibiting the AFM-TERS setup in liquid on the basis of top illumination geometry.

The second challenge for carrying out TERS in liquid is to fabricate tips with high enhancement of Raman signal and high stability. In a liquid TERS setup, the tips must be immersed into the liquid which will make them suffer contamination and degradation.<sup>[175–176]</sup> In Zenobi's work, a 20 nm layer of  $\text{SiO}_x$  was coated on the silver

surface of the AFM-TERS probe as a protective layer to improve the stability.<sup>[173]</sup> Unfortunately, an additional monolayer of ethanethiolate was necessary to prevent the analytical molecules from adsorbing onto the probe, which leads to a large decrease of the Raman enhancement with a factor of five. Similarly, Foster and coworker utilized an adhesive layer of alumina to protect TiN<sub>x</sub> probes.<sup>[177]</sup> Furthermore, the research group of Wain developed a probe with a multilayer metal coating structure.<sup>[178]</sup>

Another issue is about the feedback used to control the distance between sample and tip.<sup>[166, 175, 179]</sup> In the AFM-TERS system, the liquid affects the feedback because of the resist force of the liquid. In the STM-TERS setup, it must be pointed out that avoiding Faraday current on the tip when measuring in liquid is very important as that can interfere with the tunneling current and thereby influence the gap control between sample and tip.

Obviously, the application of TERS techniques in liquid is still in its early stages with variety of challenges. More efforts are still needed in the development of TERS in liquid for widely applying TERS techniques in biological and chemical areas. These efforts include exploration of novel setup configurations, fabricating robust probes, measuring more analytes to prove that TERS techniques can address a wide range of chemical systems and problems. These are the main motivations for one of my research works, namely placing a single plasmonic particle at the end of the probe of scanning ion conductance microscopy (SICM, a type of SPM technique which will be described in detail in Chapter 2). We will try to use this kind of plasmonic nanostructure as a tip for the TERS technique.

## 1.5 Outline of This Thesis

Plasmonic nanostructures have been widely applied in many areas, however, there is still the need to further develop simple and rapid synthesis methods for obtaining plasmonic nanostructures at low costs. In this thesis, I developed a new method to synthesize gold trioctahedrons with high-index facets and explored their applications in plasmonic sensing and SERS. In addition, I also contributed to solving the aggregation and toxic problems of nanostructure by fixing nanostructures on the glass nanopipettes. Moreover, I focused on preparing new plasmonic probes for TERS system. The detailed contents of this thesis are organized as follows.

In Chapter 2, I will firstly describe the experimental growth of noble metal nanostructures which is the basis of my thesis. The characterization techniques including UV/Vis/NIR spectrophotometry, scanning electron microscopy, and transmission electron microscopy will be introduced as well. In the last section of this chapter, a detailed description of scanning ion conductance microscopy will be given.

Chapter 3 presents a simple and fast method for preparing highly uniform gold trioctahedrons with broadly tunable sizes. The variables of growth conditions influencing the final morphologies are studied in detail. The applications in plasmonic sensing and SERS are investigated as well.

Since aggregation occurs in applying nanostructures, I developed a method to fix the nanostructures, including gold nanorods, gold nanobipyramids, gold nanospheres, and gold trioctahedrons, onto a glass nanopipette, the details will be presented in Chapter 4. The SERS properties also demonstrated by measuring three different analytes, which are rhodamine 6G (R6G), 4-methylbenzethiol (4-MBT), and 2-naphthalenethiol (2-NaT).

In Chapter 5, I will introduce the methods of realizing only a single nanoparticle modified at the end of one barrel of a double barrel nanopipette for TERS system. Finally, I will make a conclusion and give a brief outlook in Chapter 6.

## References

- [1] K. A. Willets, R. P. V. Duyne, *Annu. Rev. Phys. Chem.* **2007**, *58*, 267–97.
- [2] Y. Chen, H. Ming, *Photonics Sens.* **2012**, *2*, 37–49.
- [3] H. Malekzad, P. S. Zangabad, H. Mohammadi, M. Sadroddini, Z. Jafari, N. Mahlooji, S. Abbaspour, S. Gholami, M. G. Houshangi, R. Pashazadeh, A. Beyzavi, M. Karimi, M. R. Hamblin, *TrAC Trends Anal. Chem.* **2018**, *100*, 116–135.
- [4] K. M. Mayer, J. H. Hafner, *Chem. Rev.* **2011**, *111*, 3828–3857.
- [5] E. Petryayeva, U. J. Krull, *Anal Chim Acta*, **2011**, *706*, 8–24.
- [6] E. Hutter, J. H. Fendler, *Adv. Mater.* **2004**, *16*, 1685–1706.
- [7] H. W. Tan, J. An, C. K. Chua, T. Tran, *Adv. Electron. Mater.* **2019**, *5*, 1800831.
- [8] B. Tang, J. L. Li, X. L. Hou, T. Afrin, L. Sun, X. A. Wang, *Ind. Eng. Chem. Res.* **2013**, *52*, 4556–4563.
- [9] R. R. Arvizo, S. Bhattacharyya, R. A. Kudgus, K. Giri, R. Bhattacharya, P. Mukherjee, *Chem. Soc. Rev.* **2012**, *41*, 2943–2970.

- [10] S. Unser, I. Bruzas, J. He, L. Sagle, *Sensors* **2015**, *15*, 15684–15716.
- [11] Wikipedia, [https://en.wikipedia.org/wiki/Lycurgus\\_Cup](https://en.wikipedia.org/wiki/Lycurgus_Cup) (accessed on August 17, 2022).
- [12] I. Freestone, N. Meeks, M. Sax, C. Higgitt, *Gold Bull.* **2007**, *40*, 270–277.
- [13] M. O. J. Y. Hunault, F. Bauchau, K. Boulanger, M. Herold, G. Calas, Q. Lemasson, L. Pichon, C. Pacheco, C. Loiel, *J. Archaeolog. Sci.: Rep.* **2021**, *35*, 102753.
- [14] M. Faraday, *Phil. Trans. R. Soc. Lond.* **1857**, *147*, 145–181.
- [15] J. Jellinek, *Faraday Discuss.* **2008**, *138*, 11–35.
- [16] X. H. Huang, S. Neretina, M. A. El-Sayed, *Adv. Mater.* **2009**, *21*, 4880–4910.
- [17] T. K. Sau, A. L. Rogach, F. Jackel, T. A. Klar, J. Feldmann, *Adv. Mater.* **2010**, *22*, 1805–1825.
- [18] M. B. Cortie, A. M. McDonagh, *Chem. Rev.* **2011**, *111*, 3713–3735.
- [19] Q. F. Ruan, L. Shao, Y. W. Shu, J. F. Wang, H. K. Wu, *Adv. Optical Mater.* **2014**, *2*, 65–73.
- [20] H. J. Chen, L. Shao, Q. Li, J. F. Wang, *Chem. Soc. Rev.* **2013**, *42*, 2679–2724.
- [21] M. Tebbe, C. Kuttner, M. Mannel, A. Fery, M. Chanana, *ACS Appl. Mater. Interfaces* **2015**, *7*, 5984–5991.
- [22] T. Ming, H. J. Chen, R. B. Jiang, Q. Li, J. F. Wang, *J. Phys. Chem. Lett.* **2012**, *3*, 191–202.
- [23] R. B. Jiang, B. X. Li, C. H. Fang, J. F. Wang, *Adv. Mater.* **2014**, *26*, 5274–5309.
- [24] K. Kumar, H. G. Duan, R. S. Hegde, S. C. W. Koh, J. N. Wei, J. K. W. Yang, *Nature Nanotech.* **2012**, *7*, 557–561.
- [25] A. Kristensen, J. K. W. Yang, S. I. Bozhevolnyi, S. Link, P. Nordlander, N. J. Halas, N. A. Mortensen, *Nat. Rev. Mater.* **2017**, *2*, 16088.
- [26] X. M. Cui, X. L. Zhu, L. Shao, J. F. Wang, A. Kristensen, *Adv. Optical Mater.* **2020**, *8*, 1901605.
- [27] X. S. Kou, W. H. Ni, C. -K. Tsung, K. Chan, H. -Q. Lin, G. D. Stucky, J. F. Wang, *Small* **2007**, *3*, 2103–2113.
- [28] S. Dodson, M. Haggui, R. Bachelot, J. Plain, S. Z. Li, Q. H. Xiong, *J. Phys. Chem. Lett.* **2013**, *4*, 496–501.
- [29] A. Manjavacas, J. G. Liu, V. Kulkarni, P. Nordlander, *ACS Nano* **2014**, *8*, 7630–7638.
- [30] S. D. Forno, L. Ranno, J. Lischner, *J. Phys. Chem. C* **2018**, *122*, 8517–8527.

- [31] M. L. Brongersma, N. J. Halas, P. Nordlander, *Nature Nanotech.* **2015**, *10*, 25–34.
- [32] M. Ahlawat, D. Mittal, V. G. Rao, *Commun. Mater.* **2021**, *2*, 114.
- [33] C. C. Jia, X. X. Li, N. Xin, Y. Gong, J. X. Guan, L. N. Meng, S. Meng, X. F. Guo, *Adv. Energy Mater.* **2016**, *6*, 1600431.
- [34] C. Boerigter, U. Aslam. S. Linic, *ACS Nano* **2016**, *10*, 6108–6115.
- [35] X. Q. Liu, J. Iocozzia, Y. Wang, X. Cui, Y. H. Chen, S. Q. Zhao, Z. Li, Z. Q. Lin, *Energy Environ. Sci.* **2017**, *10*, 402–434.
- [36] A. Kumar, P. Choudhary, A. Kumar, P. H. C. Camargo, V. Krishnan, *Small* **2022**, *18*, 2101638.
- [37] P. K. Jain, X. H. Huang, I. H. El-Sayed, M. A. El-Sayed, *Acc. Chem. Res.* **2008**, *41*, 1578–1586.
- [38] G. Doria, J. Conde, B. Veigas, L. Giestas, C. Almeida, M. Assuncao, J. Rosa, P. V. Baptista, *Sensors* **2012**, *12*, 1657–1687.
- [39] M. Azharuddin, G. H. Zhu, D. Das, E. Ozgur, L. Uzun, A. P. F. Turner, H. K. Patra, *Chem. Commun.* **2019**, *55*, 6964–6996.
- [40] M. Gu, Q. M. Zhang, S. Lamon, *Nat. Rev. Mater.* **2016**, *1*, 16070.
- [41] E. Ozbay, *Science* **2006**, *311*, 189–193.
- [42] Y. N. Xia, X. H. Xia, H. -C. Peng, *J. Am. Chem. Soc.* **2015**, *137*, 7947–7966.
- [43] M. Rycenga, C. M. Cobley, J. Zeng, W. Y. Li, C. H. Moran, Q. Zhang, D. Qin, Y. N. Xia, *Chem. Rev.* **2011**, *111*, 3669–3712.
- [44] T. H. Chow, N. N. Li, X. P. Bai, X. L. Zhuo, L. Shao, J. F. Wang, *Acc. Chem. Res.* **2019**, *52*, 2136–2146.
- [45] J. E. Millstone, S. H. Park, K. L. Shuford, L. D. Qin, G. C. Schatz, C. A. Mirkin, *J. Am. Chem. Soc.* **2005**, *127*, 5312–5313.
- [46] J. Zeng, S. Roberts, Y. N. Xia, *Chem. Eur. J.* **2010**, *16*, 12559–12563.
- [47] Q. Li, X. L. Zhuo, S. Li, Q. F. Ruan, Q. -H. Xu, J. F. Wang, *Adv. Optical Mater.* **2015**, *3*, 801–812.
- [48] Z. Xi, H. H. Ye, X. H. Xia, *Chem. Mater.* **2018**, *30*, 8391–8414.
- [49] L. Wang, M. H. Kafshgari, M. Meunier, *Adv. Funct. Mater.* **2020**, *30*, 2005400.
- [50] A. Kinkhabwala, Z. F. Yu, S. H. Fan, Y. Avlasevich, K. Mullen, W. E. Moerner, *Nature Photon.* **2009**, *3*, 654–657.
- [51] M. J. Mulvihill, X. Y. Ling, J. Henzie, P. D. Yang, *J. Am. Chem. Soc.* **2010**, *132*, 268–274.

- [52] H. Wei, H. X. Xu, *Nanoscale* **2013**, *5*, 10794–10805.
- [53] Y. Q. Cao, J. W. Zhang, Y. Yang, Z. R. Huang, N. V. Long, C. L. Fu, *Appl. Spectro. Rev.* **2015**, *50*, 499–525.
- [54] M. Meng, Z. C. Fang, C. Zhang, H. Y. Su, R. He, R. P. Zhang, H. L. Li, Z. -Y. Li, X. J. Wu, C. Ma, J. Zeng, *Nano Lett.* **2016**, *16*, 3036–3041.
- [55] M. Chen, S. H. Tang, Z. D. Guo, X. Y. Wang, S. G. Mo, X. Q. Huang, G. Liu, N. F. Zheng, *Adv. Chem.* **2014**, *26*, 8210–8216.
- [56] A. Tao, P. Sinsermsuksakul, P. D. Yang, *Angew. Chem. Int. Ed.* **2006**, *45*, 4597–4601.
- [57] M. A. V. Dijk, A. L. Tchebotareva, M. Orrit, M. Lippitz, S. Berciaud, D. Lasne, L. Cognet, B. Lounis, *Phys. Chem. Chem. Phys.* **2006**, *8*, 3486–3495.
- [58] M. R. K. Ali, Y. Wu, M. A. El-Sayed, *J. Phys. Chem. C* **2019**, *123*, 15375–15393.
- [59] Y. Wu, M. R. K. Ali, K. C. Chen, N. Fang, M. A. El-Sayed, *Nano Today* **2019**, *24*, 120–140.
- [60] B. -J. Liu, K. -Q. Lin, S. Hu, X. Wang, Z. -C. Lei, H. -X. Lin, B. Ren, *Anal. Chem.* **2015**, *87*, 1058–1065.
- [61] T. T. Song, Z. X. Chen, W. B. Zhang, L. M. Lin, Y. J. Bao, L. Wu, Z. -K. Zhou, *Nanomaterials* **2019**, *9*, 564.
- [62] C. C. Li, K. L. Shuford, M. H. Chen, E. J. Lee, S. O. Cho, *ACS Nano* **2008**, *2*, 1760–1769.
- [63] M. Hu, J. Y. Chen, Z. -Y. Li, L. Au, G. V. Hartland, X. D. Li, M. Marquez, Y. N. Xia, *Chem. Soc. Rev.* **2006**, *35*, 1084–1094.
- [64] M. Chen, B. H. Wu, J. Yang, N. F. Zheng, *Adv. Mater.* **2012**, *24*, 862–879.
- [65] V. Amendola, R. Pilot, M. Frasconi, O. M. Marago, M. A. Iati, *J. Phys.: Condens Matter* **2017**, *29*, 203002.
- [66] M. G. Blaber, M. D. Arnold, M. J. Ford, *J. Phys.: Condens. Matter* **2010**, *22*, 143201.
- [67] Y. N. Xia, N. J. Halas, G. Editors, *MRS Bulletin* **2005**, *30*, 338–348.
- [68] A. Jakab, C. Rosman, Y. Khalavka, J. Becker, A. Trugler, U. Hohenester, C. Sonnichsen, *ACS Nano* **2011**, *5*, 6880–6885.
- [69] X. L. Zhuo, M. Henriksen-Lacey, D. J. D. Aberasturi, A. Sanchez-Iglesias, L. M. Liz-Marzan, *Chem. Mater.* **2020**, *32*, 5879–5889.
- [70] H. Kang, J. T. Buchman, R. S. Rodriguez, H. L. Ring, J. Y. He, K. C. Bantz, C. L. Haynes, *Chem. Rev.* **2019**, *119*, 664–699.

- [71] R. Herizchi, E. Abbasi, M. Milani, A. Akbarzadeh, *Artif. Cells Nanomed. Biotechnol.* **2016**, *44*, 596–602.
- [72] M. Shah, V. Badwaik, Y. Kherde, H. K. Waghvani, T. Modi, Z. P. Aguilar, H. Rodgers, W. Hamilton, T. Marutharaj, C. Webb, M. B. Lawrenz, R. Dakshinamurthy, *Front Biosci.* **2014**, *19*, 1320–1344.
- [73] S. Eustis, M. A. El-Sayed, *Chem. Soc. Rev.* **2006**, *35*, 209–217.
- [74] P. F. M. D. Oliveira, R. M. Torresi, F. Emmerling, P. H. C. Camargo, *J. Mater. Chem. A* **2020**, *8*, 16114–16141.
- [75] L. Shao, Y. T. Tao, Q. F. Ruan, J. F. Wang, H. -Q. Lin, *Phys. Chem. Chem. Phys.* **2015**, *17*, 10861–10870.
- [76] X. M. Cui, F. Qin, Q. F. Ruan, X. L. Zhuo, J. F. Wang, *Adv. Funct. Mater.* **2018**, *28*, 1705516.
- [77] T. Siegfried, Y. Ekinci, O. J. F. Martin, H. Sigg, *ACS Nano* **2013**, *7*, 2751–2757.
- [78] M. Bosman, L. Zhang, H. G. Duan, S. F. Tan, C. A. Nijhuis, C. -W. Qiu, J. K. W. Yang, *Sci. Rep.* **2014**, *4*, 5537.
- [79] N. N. Jiang, X. L. Zhuo, J. F. Wang, *Chem. Rev.* **2018**, *118*, 3054–3099.
- [80] W. X. Niu, L. Zhang, G. B. Xu, *Nanoscale* **2013**, *5*, 3172–3181.
- [81] N. R. Jana, L. Gearheart, C. J. Murphy, *Chem. Commun.* **2001**, 617–618.
- [82] N. R. Jana, L. Gearheart, C. J. Murphy, *J. Phys. Chem. B* **2001**, *105*, 4065–4067.
- [83] C. B. Gao, J. Goebel, Y. D. Yin, *J. Mater. Chem. C* **2013**, *1*, 3898–3909.
- [84] Y. Wang, D. H. Wan, S. F. Xie, X. H. Xia, C. Z. Huang, Y. N. Xia, *ACS Nano* **2013**, *7*, 4586–4594.
- [85] W. Ahmed, A. S. Bhatti, J. M. V. Ruitenbeek, *J. Nanopart Res.* **2017**, *19*, 115.
- [86] B. Nikoobakht, M. A. El-Sayed, *Chem. Mater.* **2003**, *15*, 1957–1962.
- [87] A. Gole, C. J. Murphy, *Chem. Mater.* **2004**, *16*, 3633–3640.
- [88] H. L. Jia, C. H. Fang, X. -M. Zhuo, Q. F. Ruan, Y. -X. J. Wang, J. F. Wang, *Langmuir* **2015**, *31*, 7418–7426.
- [89] Y. N. Xia, K. D. Gilroy, H. -C. Peng, X. H. Xia, *Angew. Chem. Int. Ed.* **2017**, *56*, 60–95.
- [90] G. Paramasivam, N. Kayambu, A. M. Rabel, A. K. Sundramoorthy, A. Sundaramurthy, *Acta Biomaterialia* **2017**, *49*, 45–65.
- [91] M. Grzelczak, J. Peres-Juste, P. Mulvaney, L. M. Lis-Marzan, *Chem. Soc. Rev.* **2008**, *37*, 1783–1791.

- [92] M. L. Personick, M. R. Langille, J. Zhang, C. A. Mirkin, *Nano Lett.* **2011**, *11*, 3394–3398.
- [93] L. Zhang, W. X. Niu, G. B. Xu, *Nano Today* **2012**, *7*, 586–605.
- [94] Z. W. Quan, Y. X. Wang, J. Y. Fang, *Acc. Chem. Res.* **2013**, *46*, 191–202.
- [95] D. K. Smith, N. R. Miller, B. A. Korgel, *Langmuir* **2009**, *25*, 9518–9524.
- [96] M. R. Langille, M. L. Personick, J. Zhang, C. A. Mirkin, *J. Am. Chem. Soc.* **2012**, *134*, 14542–14554.
- [97] S. Hou, X. N. Hu, T. Wen, W. Q. Liu, X. C. Wu, *Adv. Mater.* **2013**, *25*, 3857–3862.
- [98] K. D. Gilroy, A. Ruditskiy, H. -C. Peng, D. Qin, Y. N. Xia, *Chem. Rev.* **2016**, *116*, 10414–10472.
- [99] X. L. Zhuo, X. Z. Zhu, Q. Li, Z. Yang, J. F. Wang, *ACS Nano* **2015**, *9*, 7523–7535.
- [100] J. H. Song, F. Kim, D. Kim, P. D. Yang, *Chem. Eur. J.* **2005**, *11*, 910–916.
- [101] C. -K. Tsung, X. S. Kou, Q. H. Shi, J. P. Zhang, M. H. Yeung, J. F. Wang, G. D. Stucky, *J. Am. Chem. Soc.* **2006**, *128*, 5352–5353.
- [102] W. H. Ni, X. S. Kou, Z. Yang, J. F. Wang, *ACS Nano* **2008**, *2*, 677–686.
- [103] R. Long, S. Zhou, B. J. Wiley, Y. J. Xiong, *Chem. Soc. Rev.* **2014**, *43*, 6288–6310.
- [104] J. -H. Lee, K. J. Gibson, G. Chen, Y. Weizmann, *Nat. Commun.* **2015**, *6*, 7571.
- [105] J. G. Hinman, J. R. Eller, W. Lin, J. Li, J. H. Li, C. J. Murphy, *J. Am. Chem. Soc.* **2017**, *139*, 9851–9854.
- [106] H. Zhang, J. L. Chen, N. N. Li, R. B. Jiang, X. -M. Zhu, J. F. Wang, *ACS Appl. Mater. Interfaces* **2019**, *11*, 5353–5363.
- [107] J. Langer, S. M. Novikov, L. M. Liz-Marzan, *Nanotechnology* **2015**, *26*, 322001.
- [108] D. J. D. Aberasturi, A. B. Serrano-Montes, L. M. Liz-Marzan, *Adv. Optical Mater.* **2015**, *3*, 602–617.
- [109] S. W. Li, P. Miao, Y. Y. Zhang, J. Wu, B. Zhang, Y. C. Du, X. J. Han, J. M. Sun, P. Xu, *Adv. Mater.* **2020**, 2000086.
- [110] C. M. Coble, S. E. Skrabalak, D. J. Campbell, Y. N. Xia, *Plasmonics* **2009**, *4*, 171–179.
- [111] L. B. Sagle, L. K. Ruvuna, J. A. Ruemmele, R. P. V. Duyne, *Nanomedicine* **2011**, *6*, 1447–1462.

- [112] M. Mesch, B. Metzger, M. Hentschel, H. Giessen, *Nano Lett.* **2016**, *16*, 3155–3159.
- [113] Y. Xu, P. Bai, X. D. Zhou, Y. Akimov, C. E. Png, L. -K. Ang, W. Knoll, L. Wu, *Adv. Optical Mater.* **2019**, *7*, 1801433.
- [114] K. M. Mayer, J. H. Hafner, *Chem. Rev.* **2011**, *111*, 3828–3857.
- [115] N. L. Kazanskiy, S. N. Khonina, M. A. Butt, *Physica E* **2020**, *117*, 113798.
- [116] H. J. Chen, L. Shao, K. C. Woo, T. Ming, H. -Q. Lin, J. F. Wang, *J. Phys. Chem. C* **2009**, *113*, 17691–17697.
- [117] H. J. Chen, X. S. Kou, Z. Yang, W. H. Ni, J. F. Wang, *Langmuir* **2008**, *24*, 5233–5237.
- [118] S. Barbosa, A. Agrawal, L. Rodriguez-Lorenzo, I. Pastoriza-Santos, R. A. Alvarez-Puebla, A. Kornowski, H. Weller, L. M. Liz-Marzan, *Langmuir* **2010**, *26*, 14943–14950.
- [119] N. Nath, A. Chilkoti, *Anal Chem.* **2002**, *74*, 504–509.
- [120] S. M. Marinakos, S. H. Chen, A. Chilkoti, *Anal. Chem.* **2007**, *79*, 5278–5283.
- [121] J. N. Anker, W. P. Hall, O. Lyandres, N. C. Shah, J. Zhao, R. P. V. Duyne, *Nat. Mater.* **2008**, *7*, 442–453.
- [122] T. Sannomiya, J. Voros, *Trends Biotech.* **2011**, *29*, 343–351.
- [123] S. Alekseeva, I. I. Nedrygailov, C. Langhammer, *ACS Photonics* **2019**, *6*, 1319–1330.
- [124] C. Lambertz, A. Martos, A. Henkel, A. Neiser, T. -T. Kliesch, A. Janshoff, P. Schwille, C. Sonnichsen, *Nano Lett.* **2016**, *16*, 3540–3544.
- [125] J. -W. Jeon, J. Zhou, J. A. Geldmeier, J. F. P. Jr, M. A. Mahmoud, M. El-Sayed, J. R. Reynolds, V. V. Tsukruk, *Chem. Mater.* **2016**, *28*, 7551–7563.
- [126] K. J. I. Ember, M. A. Hoeve, S. L. McAughtrie, M. S. Bergholt, B. J. Dwyer, M. M. Stevens, K. Faulds, S. J. Forbes, C. J. Campbell, *npj Regen Med.* **2017**, *2*, 12.
- [127] R. S. Das, Y. K. Agrawal, *Vibrational Spectroscopy* **2011**, *57*, 163–176.
- [128] A. B. Zrimsek, N. H. Chiang, M. Mattei, S. Zaleski, M. O. McAnally, C. T. Chapman, A. -I. Henry, G. C. Schatz, R. P. V. Duyne, *Chem. Rev.* **2017**, *117*, 7583–7613.
- [129] X. Wang, S. -C. Huang, S. Hu, S. Yan, B. Ren, *Nat. Rev. Phys.* **2020**, *2*, 253–271.
- [130] J. Neng, Q. Zhang, P. L. Sun, *Biosens. Bioelectron.* **2020**, *167*, 112480.
- [131] A. Downes, A. Elfick, *Sensors* **2010**, *10*, 1871–1889.

- [132] D. Neuville, M. Cicconi, W. Blanc, M. Lancry, *Fiberglass Science and Technology: Materials Chemistry Characterizations, Processes, Modeling, Applications, and Sustainability*, **2021**, hal-03408691.
- [133] M. H. Brooker, O. F. Nielsen, E. Praestgaard, *J. Raman Spectrosc.* **1988**, *19*, 71–78.
- [134] J. D. Pasteris, O. Beyssac, *Elements* **2020**, *16*, 87–92.
- [135] M. Fleischmann, P. J. Hendra, A. J. McQuillan, *Chem. Phys. Lett.* **1974**, *26*, 163–166.
- [136] D. L. Jeanmaire, R. P. V. Duyne, *J. Electroanal. Chem.* **1977**, *84*, 1–20.
- [137] M. Moskovits, *J. Chem. Phys.* **1978**, *69*, 4159–4161.
- [138] M. Moskovits, *J. Raman Spectrosc.* **2005**, *36*, 485–496.
- [139] X.-M. Lin, Y. Cui, Y. -H. Xu, B. Ren, Z. -Q. Tian, *Anal. Bioanal. Chem.* **2009**, *394*, 1729–1745.
- [140] S. Schlucker, *Angew. Chem. Int. Ed.* **2014**, *53*, 4756–4795.
- [141] A. I. Perez-Jimenez, D. Lyu, Z. X. Lu, G. K. Liu, B. Ren, *Chem. Sci.* **2020**, *11*, 4563–4577.
- [142] S. -Y. Ding, E. -M. You, Z. -Q. Tian, M. Moskovits, *Chem. Soc. Rev.* **2017**, *46*, 4042–4076.
- [143] R. Pilot, R. Signorini, C. Durante, L. Orian, M. Bhamidipati, L. Fabris, *Biosensors* **2019**, *9*, 57.
- [144] W. A. Murray, W. L. Barnes, *Adv. Mater.* **2007**, *19*, 3771–3782.
- [145] H. X. Xu, J. Aizpurua, M. Kall, P. Apell, *Phys. Rev. E* **2000**, *62*, 4318–4324.
- [146] B. J. Kennedy, S. Spaeth, M. Dickey, K. T. Carron, *J. Phys. Chem. B* **1999**, *103*, 3640–3646.
- [147] N. E. Marotta, K. R. Beavers, L. A. Bottomley, *Anal. Chem.* **2013**, *85*, 1440–1446.
- [148] S. S. Masango, R. A. Hackler, N. Large, A. -I. Henry, M. O. McAnally, G. C. Schatz, P. C. Stair, R. P. V. Duyne, *Nano Lett.* **2016**, *16*, 4251–4259.
- [149] M. Meyer, E. C. L. Ru, P. G. Etchegoin, *J. Phys. Chem. B* **2006**, *110*, 6040–6047.
- [150] D. Graham, D. G. Thompson, W. E. Smith, K. Faulds, *Nature Nanotech.* **2008**, *3*, 548–551.

- [151] A. Foti, C. D'Andrea, V. Villari, N. Micali, M. G. Donato, B. Fazio, O. M. Marago, R. Gillibert, M. L. D. L. Chapelle, P. G. Gucciardi, *Materials* **2018**, *11*, 440.
- [152] S. E. J. Bell, M. R. McCourt, *Phys. Chem. Chem. Phys.* **2009**, *11*, 7455–7462.
- [153] P. Li, Y. J. Teng, Y. H. Nie, W. H. Liu, *Food Anal. Methods* **2018**, *11*, 69–76.
- [154] Z. L. Zhang, S. X. Sheng, R. M. Wang, M. T. Sun, *Anal. Chem.* **2016**, *88*, 9328–9346.
- [155] P. Verma, *Chem. Rev.* **2017**, *117*, 6447–6466.
- [156] Y. Cao, M. T. Sun, *Rev. Phys.* **2022**, *8*, 100067.
- [157] M. S. Anderson, *Appl. Phys. Lett.* **2000**, *76*, 3130–3132.
- [158] R. M. Stockle, Y. D. Suh, V. Deckert, R. Zenobi, *Chem. Phys. Lett.* **2000**, *318*, 131–136.
- [159] B. Pettinger, G. Picardi, R. Schuster, G. Ertl, *Electrochem.* **2000**, *68*, 942–949.
- [160] N. Hayazawa, Y. Inouye, Z. Sekkat, S. Kawata, *Opt. Commun.* **2000**, *183*, 333–336.
- [161] X. Shi, N. Coca-Lopez, J. Janik, A. Hartschuh, *Chem. Rev.* **2017**, *117*, 4945–4960.
- [162] F. Shao, R. Zenobi, *Anal. Bioanal. Chem.* **2019**, *411*, 37–61.
- [163] T. Deckert-Gaudig, A. Taguchi, S. Kawata, V. Deckert, *Chem. Soc. Rev.* **2017**, *46*, 4077–4110.
- [164] C. Zhang, B. Q. Chen, Z. -Y. Li, *J. Phys. Chem. C* **2015**, *119*, 11858–11871.
- [165] N. Kumar, S. Mignuzzi, W. T. Su, D. Roy, *EPJ Tech. Instrum.* **2015**, *2*, 9.
- [166] X. Wang, S. -C. Huang, T. -X. Huang, H. -S. Su, J. -H. Zhong, Z. -C. Zeng, M. -H. Li, B. Ren, *Chem. Soc. Rev.* **2017**, *46*, 4020–4041.
- [167] B. Ren, G. Picardi, B. Pettinger, *Rev. Sci. Instrum.* **2004**, *75*, 837–841.
- [168] T. -X. Huang, S. -C. Huang, M. -H. Li, Z. -C. Zeng, X. Wang, B. Ren, *Anal. Bioanal. Chem.* **2015**, *407*, 8177–8195.
- [169] P. Pienpinijtham, X. X. Han, T. Suzuki, C. Thammacharoen, S. Ekgasit, Y. Ozaki, *Phys. Chem. Chem. Phys.* **2012**, *14*, 9636–9641.
- [170] D. Mehtani, N. Lee, R. D. Hartschuh, A. Kisliuk, M. D. Foster, A. P. Sokolov, F. Cajko, I. Tsukerman, *J. Opt. A: Pure Appl. Opt.* **2006**, *8*, S183–S190.
- [171] P. Anger, P. Bharadwaj, L. Novotny, *Phys. Rev. Lett.* **2006**, *96*, 113002.
- [172] J. Stadler, T. Schmid, R. Zenobi, *Nanoscale* **2012**, *4*, 1856–1870.

- [173] T. Schmid, B. -S. Yeo, G. Leong, J. Stadler, R. Zenobi, *J. Raman Spectrosc.* **2009**, *40*, 1392–1399.
- [174] N. M. Sabanes, L. Driessen, K. F. Domke, *Anal. Chem.* **2016**, *88*, 7108–7114.
- [175] P. Pienpinijtham, S. Vantasin, Y. Kitahama, S. Ekgasit, Y. Ozaki, *J. Phys. Chem. C* **2016**, *120*, 14663–14668.
- [176] N. Kumar, C. S. Wondergem, A. J. Wain, B. M. Weckhuysen, *J. Phys. Chem. Lett.* **2019**, *10*, 1669–1675.
- [177] J. D. Scherger, M. D. Foster, *Langmuir* **2017**, *33*, 7818–7825.
- [178] N. Kumar, W. T. Su, M. Vesely, B. M. Weckhuysen, A. J. Pollard, A. J. Wain, *Nanoscale* **2018**, *10*, 1815–1824.
- [179] A. B. Britz-Grell, M. Saumer, A. Tarasov, *J. Phys. Chem. C* **2021**, *125*, 21321–21340.

# Chapter 2

## Synthesis and Techniques

2.1 Growth of Gold Nanostructures .....	52
2.1.1 Preparation of gold trisoctahedrons .....	52
2.1.2 Synthesis of gold nanospheres .....	53
2.1.3 Growth of gold nanorods .....	54
2.1.4 Growth of gold nanobipyramids .....	55
2.2 Characterization Techniques.....	55
2.2.1 UV/Vis/NIR spectrophotometry .....	56
2.2.2 Scanning electron microscopy .....	58
2.2.3 Transmission electron microscopy .....	60
2.3 Scanning Ion Conductance Microscopy .....	62
2.3.1 Fabrication of glass nanopipettes.....	64
2.3.2 Scanning ion conductance microscopy imaging.....	66
References.....	67

In this thesis, four different types of gold nanostructures are employed, namely gold trisoctahedrons, gold nanospheres, gold nanorods and gold nanobipyramids, covering a broad range of shapes and sizes. These gold nanostructures were synthesized by seed-mediated wet-chemistry methods, details given in Section 2.1. The nanostructures were subsequently characterized with different techniques to determine their plasmonic properties as well as define their structures (shapes and sizes). In Section 2.2, the description of the employed instruments and their fundamentals will be given, including UV/Vis/NIR spectrophotometry, SEM and transmission electron microscopy (TEM). Within the techniques employed, special relevance has been given to SICM, that plays an important role in the work of Chapter 4 and Chapter 5 in this thesis, where the gold nanostructures are decorated on the outer surface or the tip of a glass nanopipette, a key component of SICM system. In the present chapter, SICM will be described in Section 2.3, including what the SICM is, the working mechanisms, and some of my experimental results using this technique in sample characterization.

### **2.1 Growth of Gold Nanostructures**

One of the most intriguing features of gold nanostructures is the LSPR, which is highly dependent on their sizes and morphologies. Consequently, a significant effort has been invested to develop an extended list of methods to synthesize gold nanostructures with exquisite control of various shapes and sizes. Among them, seed-mediated method is a distinctive way which divides into two separate steps including preparation of seed and a subsequent growth.<sup>[1]</sup> This method is usually simple and can normally be carried out at room temperature without any special equipment. In this basis, I used seed-mediated methods to synthesize different gold nanostructures employed in this thesis.

#### **2.1.1 Preparation of gold trisoctahedrons**

The sharp apexes and edges of gold nanoparticles exhibit remarkable electromagnetic field enhancement,<sup>[2-3]</sup> hence, the design and preparation of gold nanoparticles with sharp corners are beneficial to enhance the Raman signal. Trisoctahedron is a type of high-index polyhedrons with 14 corners and 24 edges

which I successfully synthesized by a facile and fast seed-mediated method. Figure 2.1 is the schematic of synthesizing gold trisectahedron. The first step is to prepare the seed solution that is injecting freshly prepared ice-cold  $\text{NaBH}_4$  solution (0.01 M, 900  $\mu\text{L}$ ) into a mixture of CTAB solution (0.1 M, 9.75 mL),  $\text{HAuCl}_4$  solution (0.01 M, 150  $\mu\text{L}$ ) and chloroplatinic acid ( $\text{H}_2\text{PtCl}_6$ ) solution (0.01 M, 100  $\mu\text{L}$ ). This resultant solution can be used immediately, 20  $\mu\text{L}$  of the obtained seed solution was diluted into 10 ml deionized water. A certain amount of the diluted seed solution was added into a mixed solution which contains cetyltrimethylammonium chloride (CTAC) solution (0.1 M, 10 mL),  $\text{HAuCl}_4$  (0.01 M, 500  $\mu\text{L}$ ),  $\text{H}_2\text{PtCl}_6$  (0.01 M, 5  $\mu\text{L}$ ) and AA solution (0.1 M, 250  $\mu\text{L}$ ). The resulting mixture was kept undisturbed for 7 min at 45  $^\circ\text{C}$ .

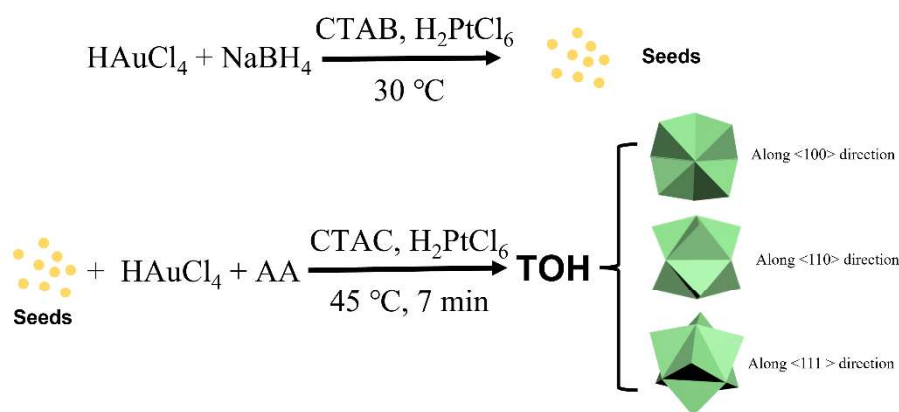


**Figure 2.1** Schematic of preparing gold trisectahedron (TOH).

### 2.1.2 Synthesis of gold nanospheres

Gold nanospheres were grown through seed-mediated method, as previously reported.<sup>[4]</sup> This method is divided into four steps, that are presented in Figure 2.2. Preparing seed solution is the first step, that is injecting the freshly prepared and ice-cold  $\text{NaBH}_4$  (0.01 M, 600  $\mu\text{L}$ ) into a mixed solution of CTAB (0.1 M, 9.75 mL) and  $\text{HAuCl}_4$  (0.01 M, 250  $\mu\text{L}$ ) under strongly stirring. The resultant solution was kept undisturbed at room temperature for 3 h. The second step is making the growth solution for growing gold nanospheres with about 20 nm. In this step, 0.12 mL of as-prepared seed solution was added into mixture solution made of deionized water (190 mL), CTAB (0.1 M, 9.75 mL),  $\text{HAuCl}_4$  (0.01 M, 4 mL), and AA (0.1 M, 15 mL) under slowly stirring. This growth solution was left undisturbed at room temperature. As for growing larger nanospheres, we used the small gold nanospheres as seeds to

grow them into larger polyhedrons firstly and then employed  $\text{HAuCl}_4$  as oxidant to transform the polyhedrons to spheres. Specifically, the small gold nanospheres were firstly centrifuged and redispersed into deionized water for further use, followed by mixing a certain volume of the small gold nanospheres with CTAC (0.025 M, 30 mL),  $\text{HAuCl}_4$  (0.01 M, 1.5 mL) and AA (0.1 M, 0.75 mL). The solution was kept gently stirring in a water bath at 45 °C for 3 h. The obtained polyhedrons were centrifuged and redispersed into 30 mL of CTAB with a concentration of 0.02 M. The oxidation reaction of polyhedrons was kept mildly stirring in 45 °C water-bath for 2 h after injecting  $\text{HAuCl}_4$  (0.01 M, 200  $\mu\text{L}$ ). The obtained gold nanospheres were centrifuged and redispersed into deionized water for storage.

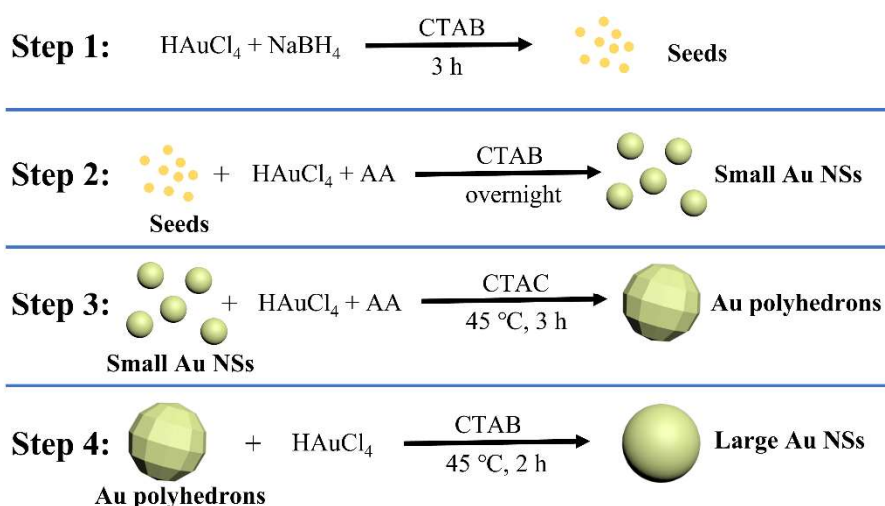


**Figure 2.2** Schematic of preparing gold nanosphere (NS).

### 2.1.3 Growth of gold nanorods

Gold nanorods were synthesized with tunable size through using a seed-mediated method, already reported in the literature.<sup>[5]</sup> The method is summarized in Figure 2.3, the seed solution is the same as that employed in synthesizing gold nanosphere, however, the growth solution is different, which contains shape-directing agent ( $\text{Ag}^+$ ) to control the gold nanorod growth.<sup>[6]</sup> The detail steps for preparing growth solution are mixing CTAB (0.1 M, 40 mL) with  $\text{HAuCl}_4$  (0.01 M, 2 mL),  $\text{AgNO}_3$  (0.01 M, 400  $\mu\text{L}$ ), and hydrochloric acid (HCl, 1 M, 800  $\mu\text{L}$ ), followed by injecting a certain volume of the as-prepared seed solution into the mixture when the solution changed to colorless due to the addition of AA (0.1 M, 320  $\mu\text{L}$ ) into the mixture.

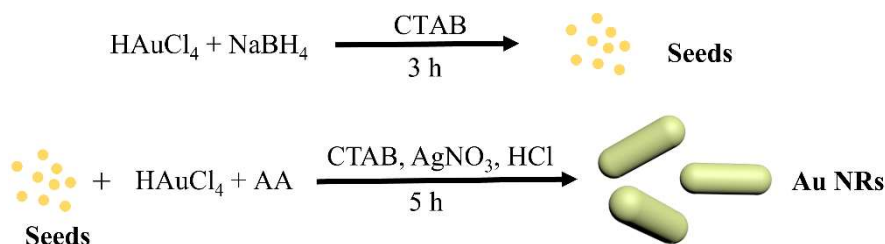


**Figure 2.3** Schematic of preparing gold nanorod (NR).

#### 2.1.4 Growth of gold nanobipyramids

Gold nanobipyramids were synthesized using seed-mediated method according to a reported procedure.<sup>[7]</sup> Typically, the seed solution was prepared by quickly adding ice-cold  $\text{NaBH}_4$  (0.025 M, 250  $\mu\text{L}$ ) in a light yellow mixed aqueous solution including CTAC (0.05 M, 10 mL),  $\text{HAuCl}_4$  (0.01 M, 250  $\mu\text{L}$ ), and citric acid (0.1 M, 500  $\mu\text{L}$ ) under vigorous stirring at room temperature. The color of the mixture gradually changed to brown which demonstrated that the seed formed. After being vigorously stirred for 2 min, the resulting seed solution was kept at 80 °C with gently stirring for 90 min and the color slowly turned to red at the meantime. The growth solution of gold nanobipyramid was made by sequential injection of  $\text{HAuCl}_4$  (0.01 M, 1 mL),  $\text{AgNO}_3$  (0.01 M, 200  $\mu\text{L}$ ), and HCl (1 M, 400  $\mu\text{L}$ ) into CTAB (0.1 M, 20 mL). A certain volume of the as-prepared seed was then added under rapid stirring after adding freshly prepared AA (0.1 M, 160  $\mu\text{L}$ ) into the mixture. The reaction solution was kept undisturbed for 2 h at 30 °C.

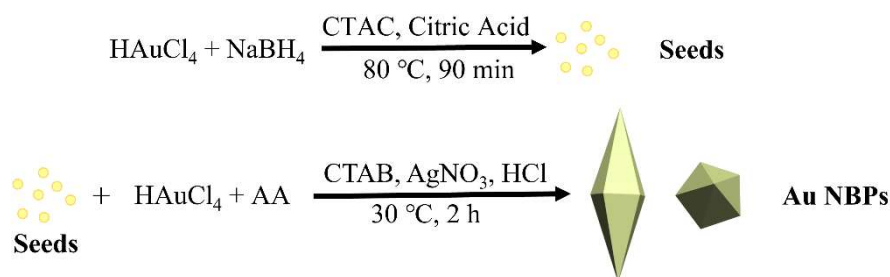


**Figure 2.4** Schematic of preparing gold nanobipyramid (NBP).

## 2.2 Characterization Techniques

A thorough characterization of the synthesized nanoparticles is paramount to confirm their expected shapes and sizes, define dispersity, understand their

performance, and establish function-structure correlations. A set of complementary techniques have been employed, providing optical and structural information at different resolution. The commonly used instrument for measuring the optical properties of gold nanostructures is UV/Vis/NIR spectrophotometer. Electron microscopies, including SEM and TEM, are generally employed to characterize the shapes, sizes and crystalline features of gold nanostructures. In this section, the characterization methods used in this thesis will be introduced.

### 2.2.1 UV/Vis/NIR spectrophotometry

Colloidal suspensions of gold nanostructures exhibit an intense color due to their strong LSPR properties, which leads to photon absorption or scattering.<sup>[8]</sup> Their optical property can be measured by a UV/Vis/NIR spectrophotometer. Figure 2.5a shows the main components of a single beam UV/Vis/NIR spectrophotometer, the collimated light generated from the light source passes through a monochromator and then wavelength selector. After the light transmitting through the sample contained in a cuvette, the final light intensity is recorded by the detectors and converted to absorption or transmission spectrum.<sup>[9-10]</sup> Before measuring samples, a pure solvent used to disperse samples is employed to do the baseline.

Since gold nanoparticles can not only absorb light but also scatter light, the obtained spectrum of colloid gold nanoparticle solution is an extinction spectrum which includes absorption and scattering. To obtain the extinction spectrum, the colloid containing gold nanostructures is placed in the path of the light beam in the spectrophotometer. The detector can record the transmitted light passing through the colloid of nanostructures. Therefore, the extinction ( $E$ ) can be determined by obtained transmissivity ( $T$ ) with the following equation:

$$E = -\text{Log } T = -\text{Log} \left( \frac{I}{I_0} \right) \quad (2.1)$$

where  $I$  is the intensity of transmitted light and  $I_0$  is the intensity of incident light. Since the gold nanostructures possess uniform sizes and morphologies, the transmissivity is generally following the Beer-Lambert Law:

$$T = \exp(-N\sigma_{\text{ext}}l) \quad (2.2)$$

where  $N$  is the particle concentration of the colloid,  $\sigma_{ext}$  is the extinction cross-section of a single nanoparticle, and  $l$  is the length of optical path, that is the cuvette length. Hence, the equation (2.1) can be written as:

$$E = -\text{Log } T = -\frac{\text{Ln } T}{\text{Ln } 10} = \frac{N\sigma_{ext}l}{\text{Ln } 10} \quad (2.3)$$

In equation (2.3), the value of extinction cross-section ( $\sigma_{ext}$ ) can be obtained from simulations or analytical calculations,<sup>[11]</sup> the length of the cuvette I used is 1 cm. I therefore can know the particle concentrations of nanostructures after obtaining extinction spectra.

In addition to the particle concentration, a large amount of other information can be extracted from the extinction spectrum. For example, the rough confirmation of the anisotropic nanostructures due to the presence of two or more plasmon bands in the spectrum.<sup>[12]</sup> Since the peak position in the extinction spectrum is highly dependent on the size or aspect ratio of nanostructures, the approximate size, aspect ratio, degree of size dispersity can be obtained based on the peak positions and *FWHM*.<sup>[12-13]</sup> Moreover, the yield of anisotropic shape purity can be roughly estimated depending on the ratio between peak intensities.<sup>[7]</sup> Additionally, extinction spectra within the UV-Vis range can be obtained in a short time with relatively inexpensive instrumentation and a little amount of sample. Therefore, it is very common to use the UV/Vis/NIR spectrophotometry to acquire optical properties of nanoparticle colloidal solutions.

In Figure 2.5b, a photograph of the spectrophotometer employed in this thesis, Agilent Technologies Cary 60 UV-Vis, is presented. After the growth of gold nanostructures, the original colloids or the colloids diluted several times were put into a quartz cuvette (Hellma Analytics 10 × 10mm) to measure their extinction spectra. There are two reasons for diluting the colloids in my thesis. The first reason is to dilute the original colloid to a detectable concentration by the spectrophotometer. The second reason is to tune the extinction intensity to the value I expected and thus control the particle concentration since the intensity is determined by the particle concentration. The examples of the extinction spectra of gold nanostructures were shown in Figure 2.5c. It is clear that gold nanobipyramid possesses two plasmonic peaks, one is the longitudinal plasmonic mode produced from the oscillation of free electrons along the length axis and the other one is transverse mode which is

perpendicular to the length axis. The small  $FWHM$  value (59 nm) of the longitudinal wavelength proves that the size distribution is very narrow. The intensity ratio between the longitudinal peak and transverse peak is 6.83, which confirms the high yield of gold nanobipyramid. However, gold nanosphere only have one dipolar peak in its extinction spectrum. The given three gold nanosphere samples have different plasmonic peaks due to their different sizes. Therefore, UV/Vis/NIR spectrophotometer is a useful tool for investigating gold nanostructures.

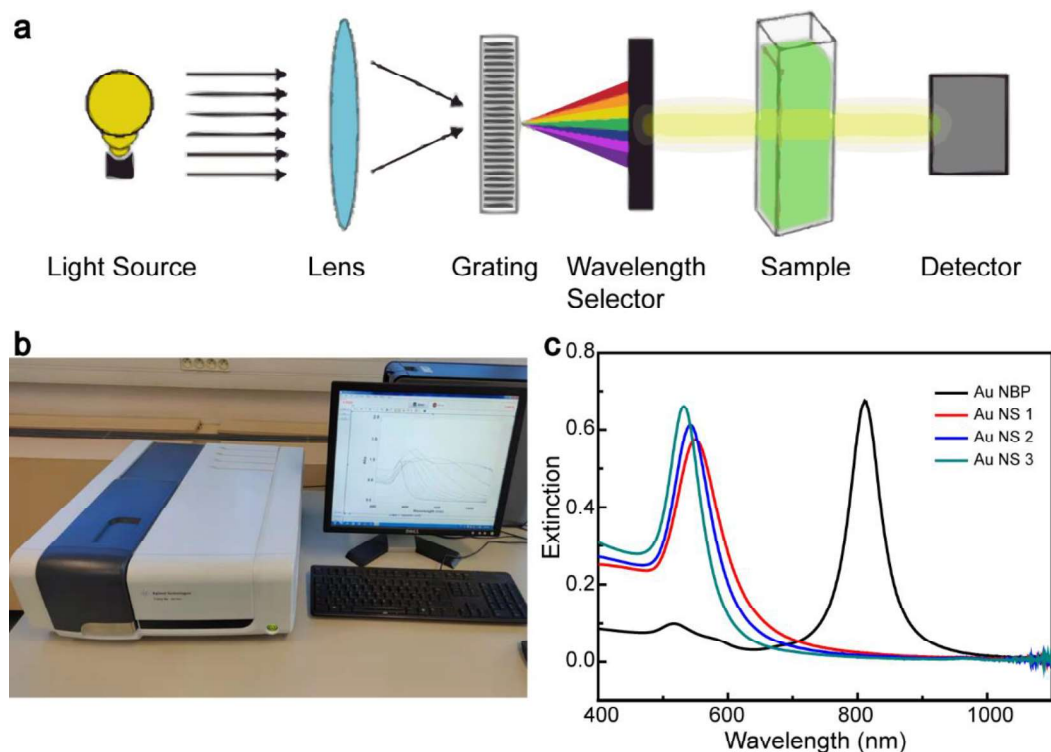


**Figure 2.5** Principles and equipment of UV/Vis/NIR spectrophotometry. (a) Schematic displaying the operation principle of the single beam spectrophotometry.<sup>[10]</sup> (b) Photography of the Agilent Technologies Cary 60 UV-Vis. (c) The examples of extinction spectra of gold nanobipyramids (Au NBPs) and three different gold nanosphere samples (Au NS 1, Au NS 2, and Au NS 3).

### 2.2.2 Scanning electron microscopy

Tools for a routine characterization of samples with nanometer resolution are fundamental in the science and technology research of nanomaterials. Among them, SEM is a widely used technique for imaging the surface of micro- or nanostructures. The versatility of SEM resides in the relatively simple sample preparation, the large area of the sample that can be interrogated, and the extended range of resolution (from hundreds of microns to a few nanometers).

Briefly, the working mechanism of SEM is that an electron beam is collimated and focused by means of magnetic lenses over a sample and rasterized over the sample while the different responses are collected. The data is instantaneously processed to obtain an image representative of the surface structure, electronic properties, and conductivity of the sample. Figure 2.6a illustrates the schematic of the key components of an SEM instrument.<sup>[14]</sup> At the top of the microscope, there is an electron gun (field emission) to generate an electron beam, which is attracted and accelerated by the positively charged anode and then travels through the electromagnetic fields and lenses along a vertical path that is used to focus the beam down onto the sample.<sup>[14-16]</sup> There are variety of signals that can be produced when the electron beam with high-energy hits the sample, such as secondary electrons, back-scattered electrons, X-rays and so on (Figure 2.6b).<sup>[17]</sup> Among them, secondary electrons and back-scattered electrons are the two types of electrons for imaging in SEM. The secondary electrons come from the surface regions of a sample, so collecting the secondary electrons to the detector provides more detailed surface information. In contrast, the back-scattered electrons originate from deeper regions which can be used to distinguish different elements. The heavier elements (larger atomic number) scatter electrons more strongly, hence, they appear brighter in the image.

In my thesis, the SEM imaging was performed on Hitachi S-4800 (Figure 2.6c) for observing the surface nanostructures of synthesized nanoparticles as well as the fabricated SICM probes. In order to obtain good images with high resolution, it is important to carefully prepare the samples for SEM imaging. For the case of gold nanoparticles, 1 mL of the synthesized gold nanoparticle colloid was centrifuged and redispersed into 1 mL of deionized water for centrifuging again, the nanoparticles were finally diluted into 100  $\mu\text{L}$  of deionized water for SEM imaging. Using deionized water to clean the nanoparticles can remove most of the surfactants around the nanoparticles and clearly observe nanostructures. However, the nanoparticles cannot be washed more times because they tend to aggregate after washing more times. A little amount (around 5  $\mu\text{L}$ ) of the above-prepared sample was dropped onto a silicon wafer and let dry at room temperature. For the characterization of SICM probes, the images were very challenging due to the non-conductive nature of the glass nanopipettes, either borosilicate glass or quartz. Due to the limitations of the SEM imaging chamber, the SICM probes have to be cut to approximately length of 2

cm using a diamond-pen. The probes were then loaded on a SEM sample holder by means of a carbon tape. It is necessary to cover the other layer of carbon tape on the top of the probes as well for anchoring the probes stably and acquiring better images.

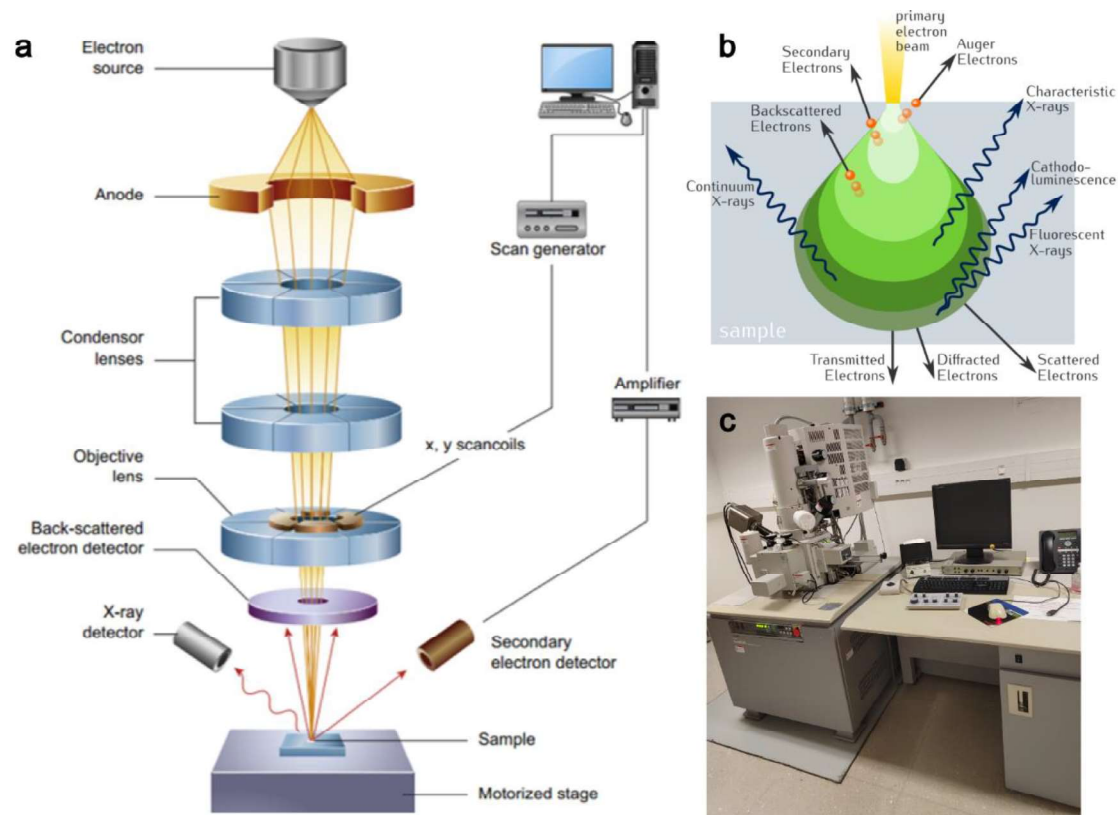


**Figure 2.6** Principles and equipment of SEM setup. (a) Schematic of a typical SEM system.<sup>[14]</sup> (b) Various signals emitted from a sample in SEM microscope.<sup>[16]</sup> (c) Photograph of Hitachi S-4800 microscope.

### 2.2.3 Transmission electron microscopy

Being able to obtain the detail of the structure (shape and size) with high resolution is necessary due to the strong dependence of plasmonic response to slight changes in size, apex radius, or aspect ratio in some anisotropic structures. TEM is a powerful technique widely used in materials science that enables the observation of crystal structures at atomic resolution, revealing grain boundaries and dislocations, investigating the growth of layers and their compositions, and analyzing the qualities, sizes, morphologies, and densities of quantum dots, wells, and wires.<sup>[14, 17]</sup>

The components of a typical TEM microscope are similar with that of SEM microscope, including an electron gun for emitting electron beam towards a specimen, electron apertures and lenses to control electron beam and obtain images (Figure

2.7a).<sup>[14]</sup> In this particular case, the electrons must pass through the sample (transmitted electrons) to form images and thus the type of samples that can be detected are limited to the very thin materials (nanometer range).

There are multiple TEM imaging modes used to capture the maximum amount of information from the specimen, including bright field imaging, electron diffraction, high-resolution TEM (HRTEM), scanning TEM, and high angle annular dark field.<sup>[18]</sup> Even in the conventional TEM images, there are a great number of fundamentally different ways to generate contrast.<sup>[19]</sup> The contrast in TEM images is defined as the intensity difference of collected signals at different positions on the specimen.<sup>[14]</sup> The first one is mass-thickness contrast which comes from the differences of thickness or density in different positions. The second one named Z contrast which arises from the differences of atomic number. The specimen with a thicker thickness or higher atomic number leads to more electrons loss due to absorption or scattering and thus the image is darker. The third one is called crystallographic contrast or diffraction contrast because of crystal structure or orientation. The electron beam will undergo Bragg scattering when it encounters a crystalline sample. When the crystal sample orients to a direction that satisfies the Bragg condition, a strong scattered beam can be generated and focused by the post specimen lenses to form an electron diffraction pattern. By carefully analyzing the diffraction pattern, a lot of structural information can be obtained, including lattice type, lattice parameter, point group, and local crystal orientation. Fourthly, an individual atom passes through the electrons is capable of producing slight quantum-mechanical phase and creating phase contrast, which is the base for doing HRTEM. For the above reasons, TEM technique is an important tool to provide exceptional nanometer or even atomic resolution information for nanoscience in materials and biological fields.

In this thesis, the low magnification TEM imaging was carried out on JEOL 2010 F at 200 kV (Figure 2.7b). The HRTEM images were acquired on FEI Titan Themis 300 (Figure 2.7c). Specimen have to be very thin to ensure the transmission of electrons is possible. For the characterization of nanoparticles, copper grids which contain a very thin layer of amorphous carbon were employed as support of the particles. In my case, a pair of inverted tweezers were employed to precisely hold one of these holey-carbon TEM grids and subsequently place a drop of the colloidal solution of interest, the method of preparing the colloidal solution for TEM imaging is the same as that for SEM imaging, as mentioned in Section 2.2.2.

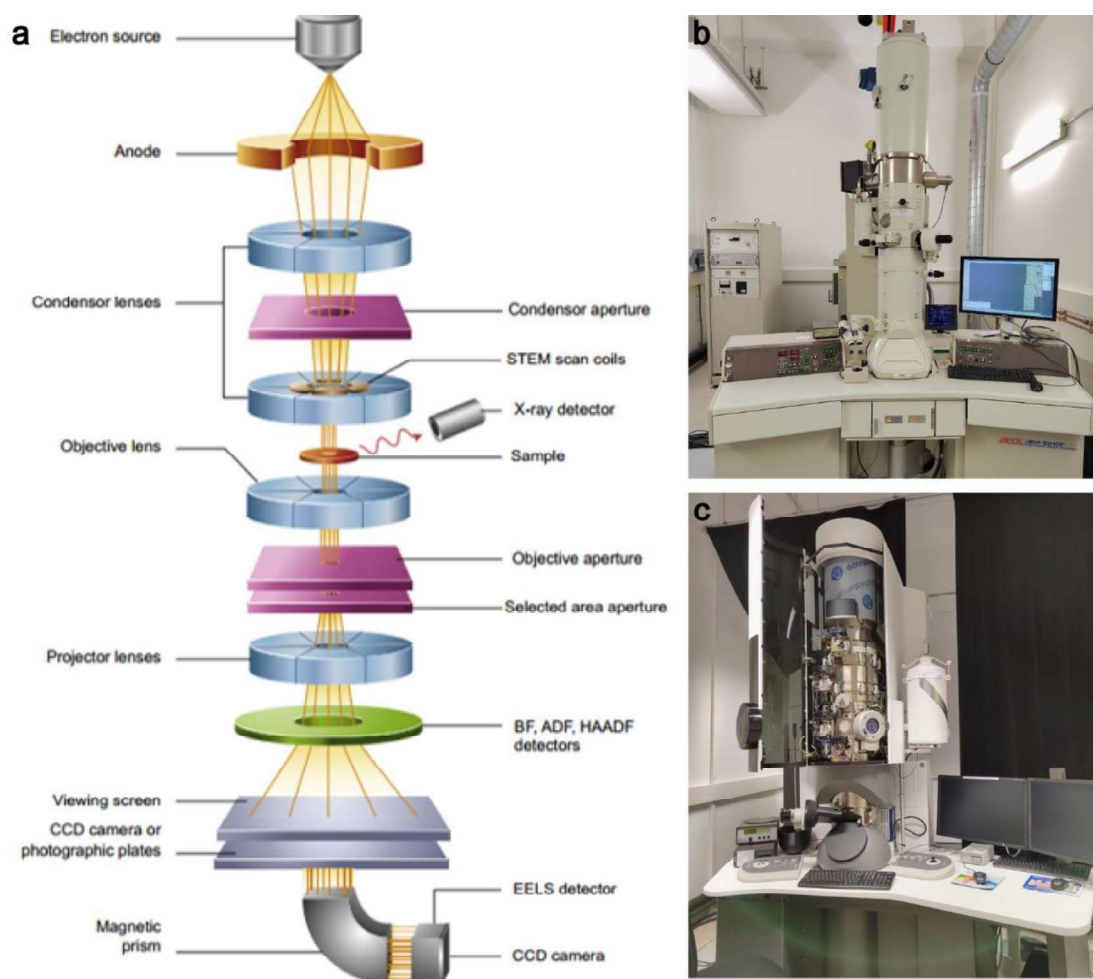


**Figure 2.7** Principles and equipment of TEM setup. (a) Schematic of a typical TEM system.<sup>[14]</sup> (b) Photography of JEOL 2010 F microscope. (c) Photography of FEI Titan Themis 300 microscope.

### 2.3 Scanning Ion Conductance Microscopy

Techniques for surface characterization based on the platform of SPM, such as the popularly employed STM or AFM, are broadly employed within the nanoscience and nanotechnology community, due to its high spatial resolution as well as the minimal invasiveness and little amount of sample requirement. In this thesis, I have contributed to the development of a type of SPM techniques termed SICM, in which the scanning probe is a pulled-pipette.<sup>[20]</sup> The SICM technique employed with a truly non-contact feedback mechanism operates in liquid, being particularly well-suited for the research on biological samples.<sup>[21–22]</sup>

In Figure 2.8a and b, they are three-dimensional and two-dimensional schematics of the SICM setup with obvious similarities to any SPM system: the probe is mounted on

a three-dimensional piezoelectric stage that allows the precise displacement of the pipette probe over the sample. In SICM, the feedback mechanism is based on the ion current resulted by the application of a bias between two quasi-reference counter electrodes (QRCEs), one inserted in the pipette probe and the other immersed in the bath where is the sample. The current is affected by a few variables, such as ion concentration of the solution, bias applied between QRCEs, geometry of the pipette, to name a few. If these parameters are fixed at certain values, the current keeps constant when the pipette is relatively far from the surface. While the pipette approaches the surface to within the diameter of the pipette, the direct current (DC) gradually decreases as the pipette approaches because the decrease of the gap between the pipette and surface leads to fewer ions that can flow through the pipette.<sup>[20]</sup> In Figure 2.8c, a representative approach curve obtained in SICM is presented, clearly showing the decrease in ion current when the pipette approached towards an inert surface. This dependency of the ion current on the tip-sample distance is used as a feedback parameter to ensure the probe can be scanned over the surface without any damage, neither on the pipette nor on the sample, by defining a suitable ion current setpoint value. The extracted information is the map of surface topography, although it exists the possibility to be influenced by local points of ion uptake or release, changing locally the ion concentration of the surface.<sup>[23]</sup> There are two commonly employed scanning modes, one is constant distance mode and the other one is hopping mode. In the constant distance mode, feedback is set to maintain the distance between pipette and surface at a constant value, the z position of pipette changing as the surface features changes. Therefore, we could get the surface topography by recording the position changes of pipette. In case of imaging surfaces featured with tall moieties, such as cells, an alternative imaging mode is defined that avoids the lateral displacement of the probe at the near proximities of the surface, this is so-called hopping mode.<sup>[23]</sup> In this mode, the probe is retracted before moving to a new lateral location and then approaches again at the new position, obtaining a set of multiple individual approaches that represent each pixel of the mapped surface, leading to a topographic image of the surface. It is important to highlight that the stability of the feedback response is susceptible to be lower with changes of the ion current, caused by the changes of bulk solution resistance, partial blockages of the nanopipette, and changes in the polarized electrodes.<sup>[23–24]</sup> In order to improve the stability, a harmonic oscillation to the vertical (z axis) position is introduced to induce

an alternating current (AC) signal on the ion conductance signal.<sup>[25]</sup> The AC signal, detected using a lock-in amplifier at the same frequency as the applied harmonic oscillation, has a dramatic increase as the distance between pipette and surface decreasing (Figure 2.8d). Therefore, using AC component of the ion conductance as the feedback can highly improve the stability and the sensitivity of surface detection as well as reduce the noise.<sup>[25–29]</sup>

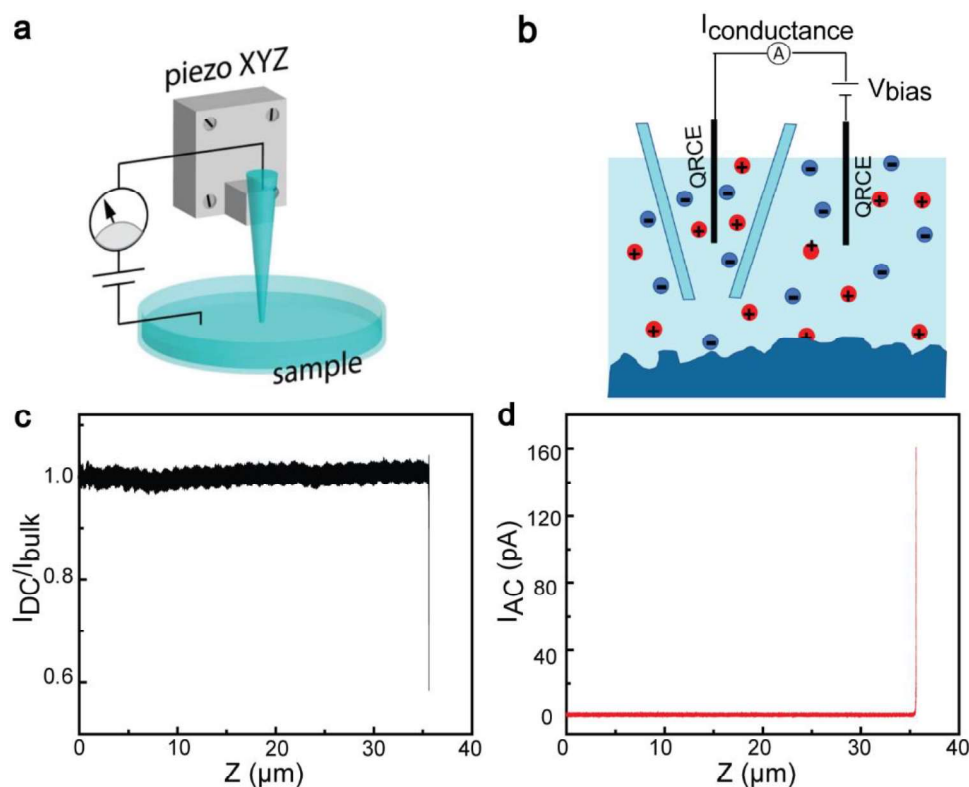


**Figure 2.8** Principles of SICM setup. (a–b) The SICM schematics, with one QRCE in a nanopipette and the second one in the bulk electrolyte. (c–d) DC and AC signal curve during an approach.

### 2.3.1 Fabrication of glass nanopipettes

In SICM, the probes are capillaries that have been pulled precisely to reach apex dimensions in the range from microns down to a few nanometers. One of the advantages of SICM is the extended variety of capillaries suitable for this application, with single-, double- or multi-barrel, conferring the potential multifunctionality of SICM technique. However, this advantage is not easily achievable with other SPM techniques. The process of SICM probe fabrication starts by pulling a hollow borosilicate or quartz glass capillary with a CO<sub>2</sub>-laser-based micropipette puller (Sutter, P-2000). The laser puller offers a set of different pulling parameters that can

be modified to obtain the nanopipettes with desired dimensions of the tips and a high degree of reproducibility. In my experiments, borosilicate pipettes with single barrel and quartz pipettes with double barrel were employed. The obtained single-barrel nanopipettes with the inner dimensions of around 130 nm from pulling borosilicate capillaries (Harvard Apparatus, GC120F-10, 1.2 OD  $\times$  0.69  $\times$  100 L mm) by employing a two-line program with the following parameters, Line 1: HEAT = 410, FIL = 3, VEL = 30, DEL = 180, PUL = -; Line 2: HEAT = 410, FIL = 4, VEL = 40, DEL = 160, and PUL = 120. Double-barrel nanopipettes with inner diameters of approximately 170 nm were obtained through pulling quartz capillaries (Friedrich & Dimmock, WAR-QTF 120-90-100) with a two-line program as well, the pulling parameters are: Line 1: HEAT = 850, FIL = 5, VEL = 45, DEL = 180, PUL = 85; Line 2: HEAT = 750, FIL = 5, VEL = 55, DEL = 160, and PUL = 110. Figure 2.9 shows SEM images of the obtained nanopipettes, where Figure 2.9a and b are an example of a single-barrel pipette and Figure 2.9c and d are the double-barrel pipette.

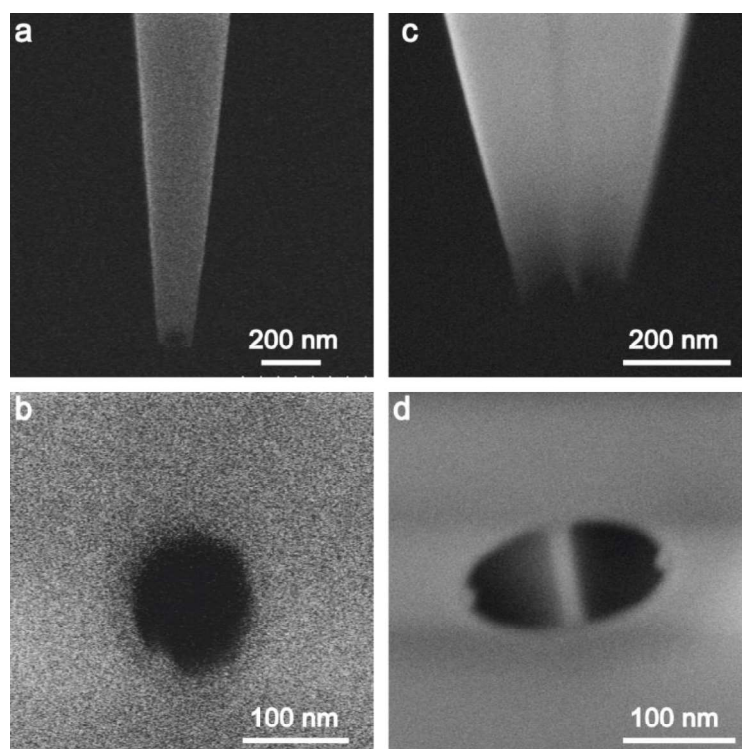


**Figure 2.9** SEM images of single- and double-barrel nanopipettes from side view (a, c), and top view (b, d)

### 2.3.2 Scanning ion conductance microscopy imaging

The laboratory is equipped with a custom-made SICM setup that operates with the WEC-SPM software, kindly provided by WEIG group at University of Warwick (UK). The probe is attached to a piezoelectric nanopositioner (Physik Instrumente, P-616 with 3 axes) for moving the nanopipette, including  $X$  axis,  $Y$  axis and  $Z$  axis. In this setup, two chloridized silver wires were employed as QRCEs. The ion current across the two electrodes is measured with an amplifier (FEMTO DLPCA-200, Germany) and the AC signal is extracted with a lock-in amplifier (Stanford Research Systems, SR 830, USA) that is also acting as wave generator.

I carried out the SICM mapping to different samples that represent different topographic scenarios: flat surfaces, surfaces with steps ( $\sim 140$  nm height), and surfaces with nanoparticles (nanospheres synthesised as described in Section 2.1). I imaged these featured samples using the AC current magnitude as feedback, 0.1 M potassium chloride solution (both in and out of the pipette) as the electrolyte, 0.1 V bias was applied between the two QRCEs, and the oscillating frequency is 285.3 Hz during the scanning process. Figure 2.10a is the obtained SICM topographical image employing constant distance mode for a flat surface of silicon wafer. For this particular image, the image is a  $32 \times 32$  pixels image (32 lines of 32 pixels per line) with a total area of  $3 \mu\text{m} \times 3 \mu\text{m}$ . To demonstrate the capabilities of the instrument to trace surface features, I measured a sample containing a step of about 140 nm in height. Because the height is relatively high with respect the dimension of the probe employed, the hopping mode was used to avoid breaking the pipette. To obtain the topographic map shown in Figure 2.10b, the probe was hopping scanning a  $3 \mu\text{m} \times 3 \mu\text{m}$  surface with a lateral hopping distance of 100 nm, revealing the sharp edge at the interface and the height is about 140 nm. The line profile in Figure 2.10c corresponding to the red line in Figure 2.10b can further confirm that SICM can be used for imaging surface topography with high resolution. I tried the use of SICM to measure gold nanospheres with diameters around 100 nm. Firstly, we did SEM imaging to check the size and the distribution of the particles (Figure 2.10d). Then the SICM map was obtained by a constant distance mode with 64 pixels for each line and 64 lines for the whole map covering an area of  $3 \mu\text{m} \times 3 \mu\text{m}$  (Figure 2.10e). The line profile in Figure 2.10f which corresponds with the red line in Figure 2.10e confirms the height of gold nanosphere is about 100 nm. However, as is typical in SPM, the

lateral distances are misleading and do not represent the real dimension of the particles due to the classic tip convolution effect. Furthermore, some particles form assemblies, that also result in larger features observed in SICM map. Nevertheless, the images prove the possibility of imaging nanoparticles by SICM which is a key achievement for the following experiments.

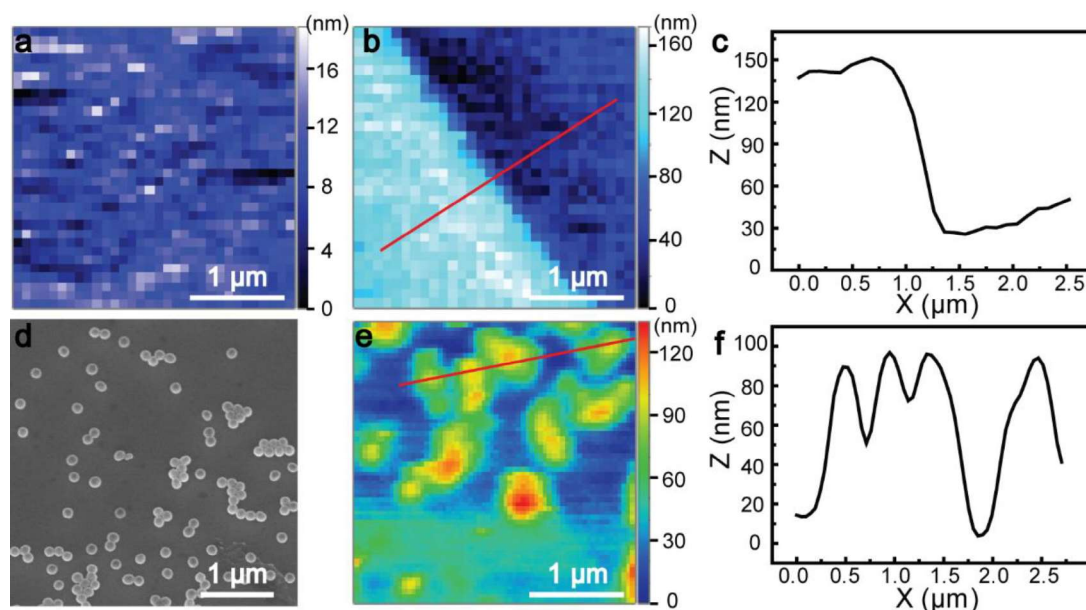


**Figure 2.10** SICM imaging for different samples. (a–b) SICM topographical images of flat surface and surface with steps. (c) The line scan across the surface with steps corresponding with the red line in b. (d–e) SEM and SICM topographical images of gold nanospheres. (f) The line profile of gold nanospheres corresponding with the red line in e.

## References

- [1] N. R. Jana, L. Gearheart, C. J. Murphy, *Adv. Mater.* **2001**, *13*, 1389–1393.
- [2] F. Hao, C. L. Nehl, J. H. Hafner, P. Nordlander, *Nano. Lett.* **2007**, *7*, 729–732.
- [3] S. Tanwar, K. Haldar, T. Sen, *J. Am. Chem. Soc.* **2017**, *139*, 17639–17648.
- [4] Q. Ruan, L. Shao, Y. Shu, J. Wang, H. Wu, *Adv. Optical Mater.* **2014**, *2*, 65–73.
- [5] W. Ni, X. Kou, Z. Yang, J. Wang, *ACS Nano* **2008**, *2*, 677–686.
- [6] H. Chen, L. Shao, Q. Li, J. Wang, *Chem. Soc. Rev.* **2013**, *42*, 2679–2724.
- [7] A. Sanchez-Iglesias, N. Winckelmans, T. Altantzis, S. Bals, M. Grzelczak, L. M. Liz-Marzan, *J. Am. Chem. Soc.* **2017**, *139*, 107–110.

- [8] E. C. Dreaden, A. M. Alkilany, X. H. Huang, C. J. Murphy, *Chem. Soc. Rev.* **2012**, *41*, 2740–2779.
- [9] S. Jena, R. B. Tokas, S. Thakur, N. K. Sahoo, *SMC Bulletin* **2015**, *6*, 1–9.
- [10] Psiberg, <https://psiberg.com/uv-vis-spectroscopy> (accessed on August 20, 2022).
- [11] L. Novotny, B. Hecht, *Principles of Nano-Optics*, **2012**.
- [12] N. Li, P. X. Zhao, D. Astruc, *Angew. Chem. Int. Ed.* **2014**, *53*, 1756–1789.
- [13] S. W. Prescott, P. Mulvaney, *J. Appl. Phys.* **2006**, *99*, 123504.
- [14] B. J. Inkson, *Materials Characterization Using Nondestructive Evaluation (NDE) Methods* **2016**, 17–43.
- [15] Purdue University,  
<https://www.purdue.edu/ehrs/rem/laboratory/equipmentsafety/ResearchEquipment/sem.html> (accessed on August 20, 2022).
- [16] Wikipedia, [https://en.wikipedia.org/wiki/Scanning\\_electron\\_microscope](https://en.wikipedia.org/wiki/Scanning_electron_microscope) (accessed on August 20, 2022).
- [17] W. Sigle, *Annu. Rev. Mater. Res.* **2005**, *35*, 239–314.
- [18] L. Reimer, H. Kohl, *Springer Series in Optical Sciences*, **2008**, 36.
- [19] Wikipedia, [https://en.wikipedia.org/wiki/Transmission\\_electron\\_microscopy](https://en.wikipedia.org/wiki/Transmission_electron_microscopy) (accessed on August 20, 2022).
- [20] P. K. Hansma, B. Drake, O. Marti, S. A. C. Gould, C. B. Prater, *Science* **1989**, *243*, 641–643.
- [21] C. -C. Chen, Y. Zhou, L. A. Baker, *Annu. Rev. Anal. Chem.* **2012**, *5*, 207–228.
- [22] C. Zhu, K. Huang, N. P. Siepser, L. A. Baker, *Chem. Rev.* **2021**, *121*, 11726–11768.
- [23] P. Novak, C. Li, A. J. Shevchuk, R. Stepanyan, M. Caldwell, S. Hughes, T. G. Smart, J. Gorelik, V. P. Ostanin, M. J. Lab, G. W. J. Moss, G. I. Frolenkov, D. Klenerman, Y. E. Korchev, *Nat. Methods* **2009**, *6*, 279–281.
- [24] K. McKelvey, D. Perry, J. C. Byers, A. W. Colburn, P. R. Unwin, *Anal. Chem.* **2014**, *86*, 3639–3646.
- [25] A. I. Shevchuk, J. Gorelik, S. E. Harding, M. J. Lab, D. Klenerman, Y. E. Korchev, *Biophys. J.* **2001**, *81*, 1759–1764.
- [26] K. T. Rodolfa, A. Bruckbauer, D. J. Zhou, Y. E. Korchev, D. Klenerman, *Angew. Chem.* **2005**, *117*, 7014–7019.
- [27] K. T. Rodolfa, A. Bruckbauer, D. J. Zhou, A. I. Schevchuk, Y. E. Korchev, D. Klenerman, *Nano Lett.* **2006**, *6*, 252–257.

- [28] D. Pastre, H. Iwamoto, J. Liu, G. Szabo, Z. Shao, *Ultramicroscopy* **2001**, *90*, 13–19.
- [29] D. Perry, R. A. Botros, D. Momotenko, S. L. Kinnear, P. R. Unwin, *ACS Nano* **2015**, *7*, 7266–7276.

# Chapter 3

## A Facile and Fast Method for Synthesizing Gold Trisoctahedrons

3.1 Preparation of the Gold Trisoctahedrons .....	72
3.1.1 Growth of gold trisoctahedrons with tunable sizes .....	72
3.1.2 The factors for influencing the final morphology of nanostructure .....	78
3.2 Outstanding Properties of Gold Trisoctahedrons .....	88
3.2.1 Refractive index sensitivity .....	88
3.2.2 Surface-enhanced Raman spectroscopy .....	92
3.3 Summary .....	95
References .....	95

The existing correlation between the properties of gold nanostructures (e.g., chemical and optical) and their morphology is fueling the enormous attention and research efforts to prepare gold nanostructures with controllable shapes in the last decades. Especially, nanostructures with high-index facets – at least one of the three Miller indices is larger than one – have attracted a great deal of attention as they possess higher density of atomic kinks, steps, and edges, resulting in higher chemical-reaction activities in comparison with the nanostructures with low-index facets.<sup>[1-2]</sup> Furthermore, nanostructures with sharp tips and edges have much stronger local electromagnetic field around their tips with respect to their flat counterpart, this stronger local electromagnetic field endows nanostructure with higher plasmonic sensitivity and more efficient SERS performance.<sup>[3-4]</sup> Nevertheless, the synthesis of gold nanostructures with high-index facets is significantly challenging since the high-index facets possess high surface energy leading to fast atom deposition rates on these facets and thus easily disappear during growth process. As a result, the nanoparticles tend to have low-index facets, such as {100}, {111}, and {110}, during the process of preparation to minimize the surface energy of nanoparticles.<sup>[5]</sup> Various of gold nanostructures with low-index facets have been reported, including nanocubes,<sup>[6]</sup> nanorods,<sup>[7-8]</sup> octahedrons,<sup>[9]</sup> and rhombic dodecahedrons.<sup>[10]</sup> Consequently, it is much more challenging to prepare nanostructures enclosed by high-index facets.

The rapid development of plasmonic nanostructures makes researchers understand that the morphology of noble metal nanostructures is capable of being controlled through tuning the kinetic and thermodynamic parameters during the process of preparation in liquid.<sup>[11-12]</sup> This understanding allows the appearance of novel methods for synthesizing nanostructures enclosed by high-index facets and various of morphologies, including tetrahedron with {hk0} facets, trapezohedron with {hkk} facets, trisioctahedron with {hhl} facets, and hexooctahedron with {hkl} facets.<sup>[13]</sup> Within the family of gold nanostructures enclosed by high-index facets, trisioctahedrons bounded by 24 triangular high-index facets are considered to be really promising nanostructures for a wide range of applications.<sup>[11, 13]</sup> In 2008, Ma and co-workers first reported a wet-chemical method to synthesis gold trisioctahedrons enclosed by {221} facets.<sup>[1]</sup> Since then, the research on the trisioctahedrons has never stopped. For example, Song *et al* synthesized {331}-faceted trisioctahedrons through using CTAC as the surfactant in seed solution in 2015.<sup>[14]</sup> The Xia group, in 2018, presented the synthesis of trisioctahedrons with tunable size ranging from 20 nm to 80

nm as well as the ability to tune the dihedral angle by changing the reaction temperature.<sup>[15]</sup> However, these existing methods for preparing gold trisoctahedrons are time-consuming or involve many steps, more efforts are still needed to further explore simpler and faster methods that are capable of obtaining gold trisoctahedrons with a wider range of tunable sizes.

In this chapter, I will present a very simple and very fast seed-mediated method to obtain gold trisoctahedrons. In this method, the seed solution can be used immediately after finishing preparation and the following growth process only took 7 min. Furthermore,  $\text{H}_2\text{PtCl}_6$  was used as shape-directing agent to grow gold trisoctahedrons with high purity. The size of the resulting nanostructures can be controlled in a wide range from 39 nm to 268 nm through simply varying the seed amount in the growth solution while keeping other conditions unchanged. The Miller indices of facets for forming gold trisoctahedron are able to be tuned from  $\{441\}$  to the limiting case  $\{110\}$  by improving the reaction temperature. Finally, I also demonstrated that the well-defined tips and edges make the gold trisoctahedrons synthesized with my method exhibit high plasmonic sensitivity and efficient SERS performance.

### 3.1 Preparation of the Gold Trisoctahedrons

In this section, the strategies and experiments for optimizing the synthesis of gold trisoctahedrons with tailoring sizes will be introduced. The synthetic method is a simple one-step seeded growth method as described in Chapter 2.

#### 3.1.1 Growth of gold trisoctahedrons with tunable sizes

Trisoctahedron could be regarded as “pulling out” the centers of the eight triangular faces in an octahedron. Three new faces are generated after “pulling” one face and an octahedron possesses eight faces, hence, gold trisoctahedron has 24 faces. Since all these 24 facets belong to the crystal planes of the  $\langle 110 \rangle$  zone axis family, their Miller indices are  $\{hhl\}$ .<sup>[1]</sup> A complete set of characterization information is obtained for a typical gold trisoctahedron sample, synthesized by my method, including UV/Vis/NIR spectrophotometry spectrum for determining the plasmonic peaks, as well as SEM images, TEM images, and HRTEM images to characterize the morphology and the size. The extinction spectrum of the obtained nanostructure colloid (black line in

Figure 3.1a) exhibits only one plasmonic peak which is located at 607 nm. The successful acquisition of gold trisoctahedrons was clearly demonstrated by SEM imaging, as shown in Figure 3.1b. The low-magnification SEM image indicates that uniform gold trisoctahedrons with a high purity can be obtained, only a few byproducts were found to be truncated bipyramids (Figure 3.1c). Although the contours of some nanostructures do not look like trisoctahedrons at first glance, most of them are able to be matched to the trisoctahedral morphology by taking into account the different orientations of the trisoctahedrons. Figure 3.1d displays the schematic models of ideal trisoctahedrons in different orientations, which can help to identify trisoctahedron nanostructures.

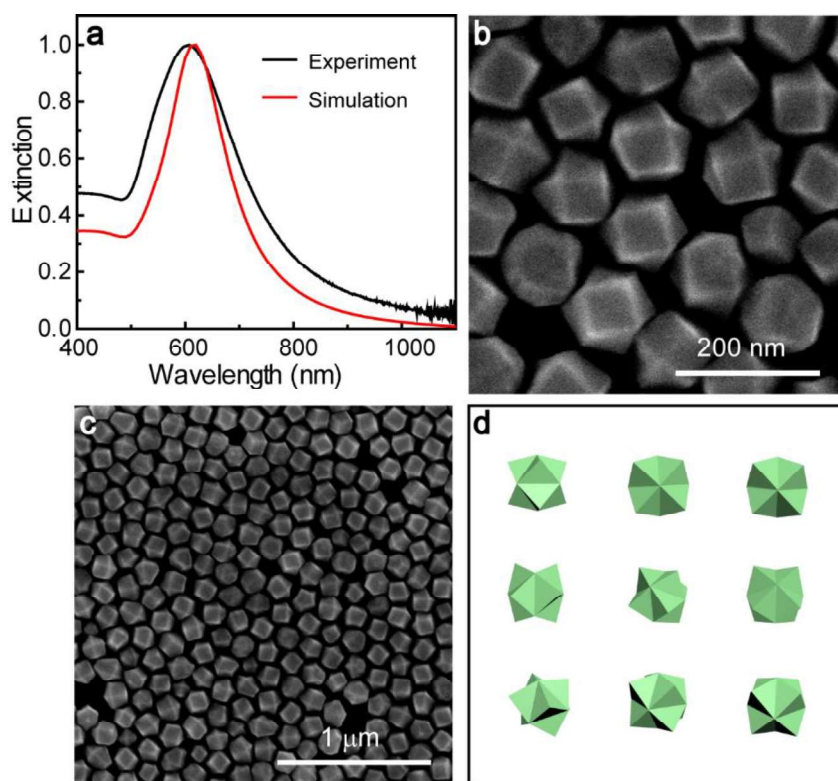


**Figure 3.1** Gold trisoctahedron sample. (a) Normalized extinction spectra of gold trisoctahedrons with size of  $123 \pm 8$  nm recorded on a UV/Vis/NIR spectrophotometer (black line) and calculated results by finite element method simulation (red line), the simulation data is kindly provided by Dr. Alexandre Baron and Mr. Florian Lochon in University of Bordeaux. (b–c) SEM images of gold trisoctahedrons with size of  $123 \pm 8$  nm. (d) The schematics of ideal trisoctahedron structures with several typical orientations.

TEM images were used to obtain more detailed structural information, as illustrated in Figure 3.2a and b. In particular, the average size of this trisoctahedron sample along

the longest axis (see the schematic inserted in Figure 3.2a for definition) was determined from TEM imaging to be  $123 \pm 8$  nm, the wide size distribution comes from the deviation of the projection direction. As for trisoctahedron structure, the Miller indices of the exposed facets can be decided by the projection angles.<sup>[14, 16]</sup> As illustrated in the top right inset in Figure 3.2b, when the gold trisoctahedron is viewed along the  $\langle 110 \rangle$  direction, the angles are defined as  $\alpha$ ,  $\beta$ , and  $\gamma$ , respectively. The relationships between angles and Miller indices follow the equations below<sup>[13, 16]</sup>:

$$\alpha = 2 \arctan \frac{\sqrt{2}h}{h-l} \quad (3.1)$$

$$\beta = 90 - \frac{\alpha}{2} + \frac{\gamma}{2} \quad (3.2)$$

$$\gamma = 2 \arctan \frac{\sqrt{2}h}{l} \quad (3.3)$$

Therefore, the projection angles of trisoctahedron viewed along  $\langle 110 \rangle$  direction were measured from TEM images. Figure 3.2b is a typical TEM image of an individual trisoctahedron oriented along  $\langle 110 \rangle$  axis, the corresponding selected area electron diffraction pattern (bottom right insert) confirms the direction. The  $\alpha$  angle is approximately  $130^\circ$ , which determines the Miller indices of the facets are  $\{331\}$ , and the  $\gamma$  angle is around  $163.3^\circ$  which is close to that of  $\{551\}$  facets ( $163.9^\circ$ ). Furthermore, the Miller indices of facets can be determined by a direct measurement method, analyzing the arrangement of atoms on exposed facets from HRTEM images. Based on the micro-facet notion theory, first reported by Somorjai and co-workers,<sup>[17]</sup> the HRTEM image in Figure 3.2c illustrates that the Miller index of one edge-on facet is  $\{551\}$  since the facets is denoted by  $3(110) \times (111)$ , matching well with the atomic model (Figure 3.2d).

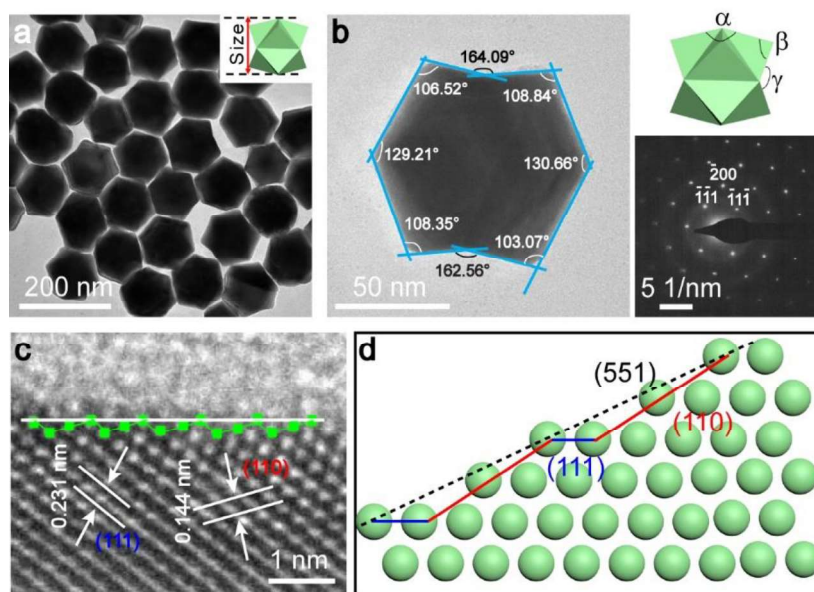


**Figure 3.2** Characterization of the gold trisioctahedrons. (a) The low-magnification TEM image of gold trisioctahedrons with size of  $123 \pm 8$  nm. (b) High-magnification TEM image of a single trisioctahedron with size of 94 nm, recorded along the  $\langle 110 \rangle$  direction; top-right inset: a schematic of an ideal trisioctahedron projected from  $\langle 110 \rangle$  direction; bottom-right inset: the corresponding selected area electron diffraction pattern. (c) HRTEM image of gold trisioctahedron with size of 94 nm, recorded along the  $\langle 110 \rangle$  direction. (d) Two-dimensional atomic model illustrating the high-index (551) facet.

With the morphological parameters of trisioctahedron from experiment measurements, the ideal mode was set to calculate its extinction spectrum by finite element method. The simulation result, plotted as a red line in Figure 3.1a, shows a good agreement with the experiment result. The small differences between simulation and experimental result can be considered as a consequence of the size distribution and the prepared gold trisioctahedrons are not ideal trisioctahedron with very sharp tips (slightly truncated).

The ability to synthetically tailor the LSPR properties is one of the most outstanding features of gold nanostructures, and this can be achieved by controlling the size. The typical strategy to control nanoparticle size is to simply vary the seed amount in the growth solution while keeping other parameters constant with respect to one-step seeded growth.<sup>[18]</sup> The approach used in my study for preparing gold trisioctahedrons is one-step seed-mediated method as well, therefore, the size of gold trisioctahedrons can be easily and well controlled by varying the volume of seed

solution. With my method, the size of the gold trisioctahedrons can be tuned from around 268 nm to 39 nm when the volume of the diluted seed solution in the growth solution was increased from 5  $\mu\text{L}$  to 2 mL. Figure 3.3 shows the SEM and TEM images of gold trisioctahedrons with four different sizes, the average sizes measured from their TEM images are  $268 \pm 22$  nm,  $178 \pm 8$  nm,  $87 \pm 4$  nm, and  $39 \pm 3$  nm, and the volumes of seed solution injected into growth solution for preparing these four sizes of gold trisioctahedrons are 5  $\mu\text{L}$ , 20  $\mu\text{L}$ , 150  $\mu\text{L}$ , and 2 mL, respectively.

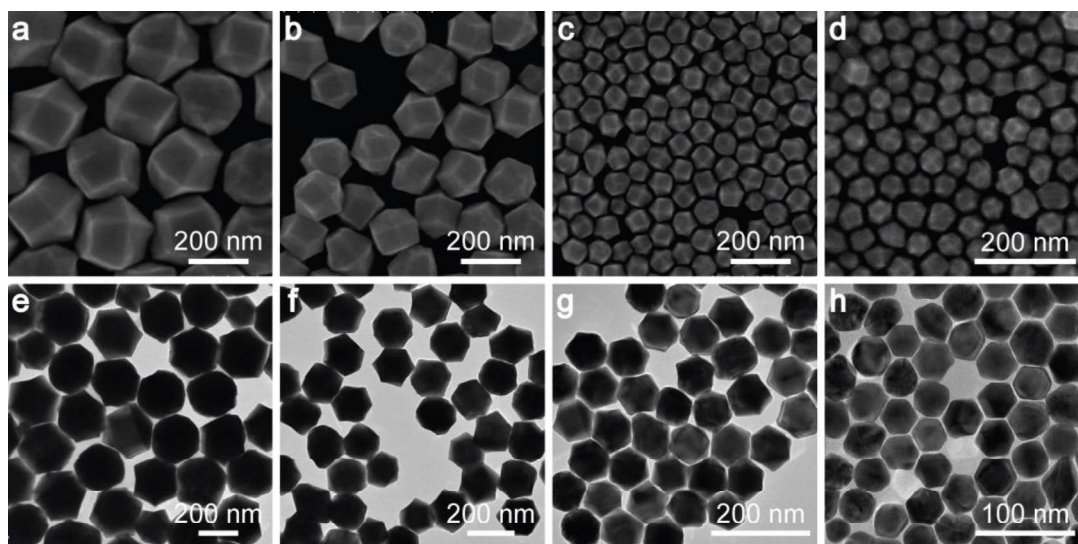


**Figure 3.3** SEM and TEM images of four sizes of gold trisioctahedron samples. (a–d) SEM images of gold trisioctahedrons with various sizes. (e–h) The corresponding TEM images of the gold trisioctahedrons. Their sizes are measured to be  $268 \pm 22$  nm,  $178 \pm 8$  nm,  $87 \pm 4$  nm, and  $39 \pm 3$  nm, respectively.

In order to explore the relationship between the size of gold trisioctahedrons and the volume of the seed solution added into growth solution as well as the relationship of the plasmonic extinction peak of trisioctahedrons with the amount of the seed solution in the growth solution, a set of 13 trisioctahedron samples with different sizes were prepared. Figure 3.4a is a digital photograph of these samples, exhibiting a variation of the colors of these 13 samples ranging from brown to purple and finally red as the amount of seed solution increased from 5  $\mu\text{L}$  to 2 mL. The extinction spectra of these 13 samples (Figure 3.4b) show that the dipolar plasmon peak gradually blue shifts from 923 nm to 532 nm when the volume of seed solution varies from 5  $\mu\text{L}$  to 2 mL. To emphasize this trend, the wavelength of dipolar plasmon peak is plotted as the function of seed volume (Figure 3.4c), observing a dramatic blue shift from 923 nm to 634 nm when the volume changes from 5  $\mu\text{L}$  to 30  $\mu\text{L}$ . However, the wavelength only

changes from 547 nm to 532 nm when the volume of seed solution increases from 500  $\mu\text{L}$  to 2 mL.

Their sizes obtained from TEM imaging are plotted as functions of seed solution volumes in Figure 3.4c as well, it clearly shows that the size of gold trisioctahedrons gradually decreases as the seed solution volume increases. The trend of size changing as the seed solution volume increases is similar with that of peak wavelength changing. Therefore, I also exhibit the variations of dipolar peak as the function of their sizes (Figure 3.4d). A double-linear behavior was observed, with a slope of the fitting line of approximately 0.92 for the small size particles ( $\leq 144$  nm) and a slope of about 2.75 for sizes larger than 178 nm. This large difference is probably related to the variations in the volume of the nanostructures.<sup>[18–20]</sup> The volume of gold trisioctahedron is linearly dependent on the cubic power of its size, therefore, the volume changes quickly as the size change when the particle is large. It is also noticeable that the dipolar peak is wider when the added volume of seed solution is low in the growth solution, it is because the size is larger when the volume of seed solution is low, and therefore more losses of radiation.<sup>[21]</sup> In addition, the size distribution is broader when the growth solution with less volume of seed solution.

It must be pointed out that quadrupole or even multipole excitation can be formed in large nanostructures.<sup>[22]</sup> The extinction spectra in Figure 3.4b apparently illustrate that the quadrupolar mode is formed in large gold trisioctahedrons. There are two peaks in the extinction spectrum for large gold trisioctahedrons, one is dipolar mode and the other one attributes to quadrupolar mode. Take the sample synthesized with 10  $\mu\text{L}$  seed solution as an example, the final size of the gold trisioctahedrons is  $216 \pm 12$  nm. There are two plasmonic peaks in its extinction spectrum, one is located at 760 nm which belongs to the dipolar mode and the other one at 578 nm is quadrupolar mode. In order to certificate the nature of each plasmon mode, finite element method simulation was conducted. The calculated spectra are seen to be in good agreement with the experimental results and elucidate that the peak with lower energy is dipolar mode and the other one located at the area with higher energy is quadrupole mode (Figure 3.4e).

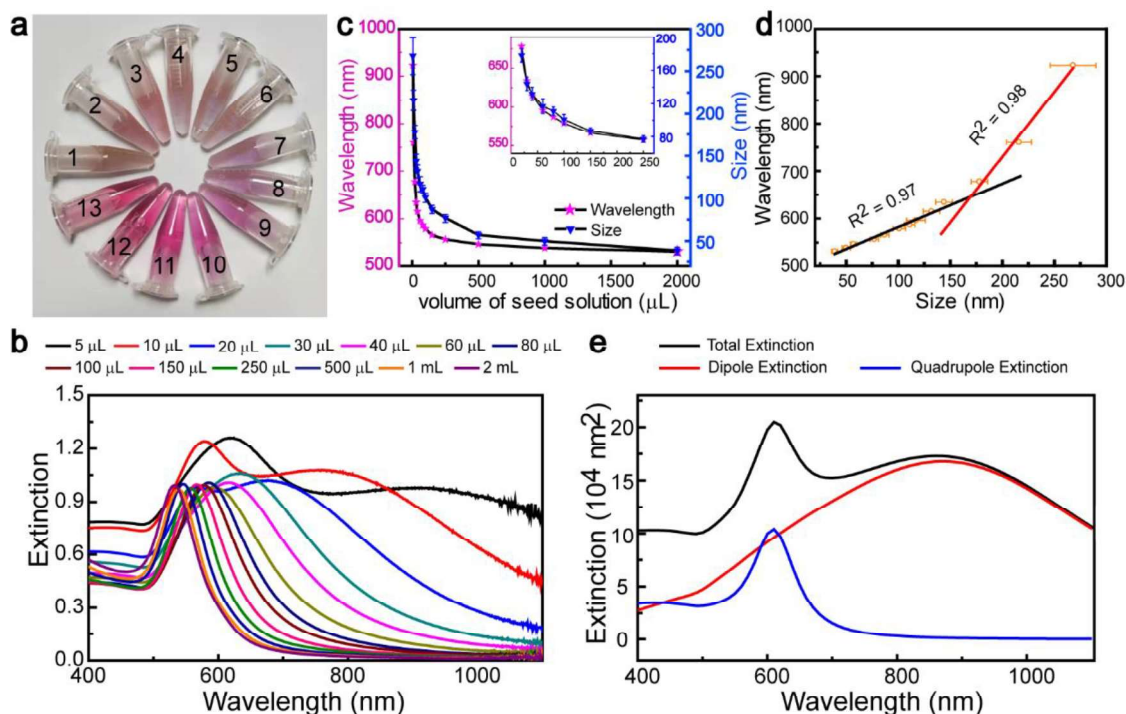


**Figure 3.4** The variations of the products in colloid color, extinction spectra, and size with increasing the seed volume in the growth solution. (a) Digital photograph of 13 samples synthesized with different volume of seed solution in the growth solution. From 1 to 13, the volumes of seed solution are 5  $\mu\text{L}$ , 10  $\mu\text{L}$ , 20  $\mu\text{L}$ , 30  $\mu\text{L}$ , 40  $\mu\text{L}$ , 60  $\mu\text{L}$ , 80  $\mu\text{L}$ , 100  $\mu\text{L}$ , 150  $\mu\text{L}$ , 250  $\mu\text{L}$ , 500  $\mu\text{L}$ , 1 mL, and 2 mL, respectively. (b) Extinction spectra of these 13 samples. (c) Variations of the LSPR peak and size with the volume of seed solution. (d) The relationship between LSPR peak of gold trisioctahedrons with its size. (e) The simulated extinction spectra of gold trisioctahedrons with size of 216 nm by finite element method simulation. The simulation data is kindly provided by Dr. Alexandre Baron and Mr. Florian Lochon in University of Bordeaux.

### 3.1.2 The factors for influencing the final morphology of nanostructure

The morphologies of nanostructures prepared by seed-mediated method are significantly affected by the kinetic parameters like concentration and temperature, as well as thermodynamic factors such as the surfactant and the reduction potential of the employed reduction agent.<sup>[12]</sup> In order to find the optimal growth conditions for obtaining gold trisioctahedrons, sets of experiments were carried out in my study, including the changes of growth temperature, variations in the volume of reduction

agent, different concentrations and types of surfactants, the effects of shape-directing agent, and the variations of the final morphologies as the growth time increases.

### ***Growth temperature***

Following the analogy of a chemical reaction, in the process of the nanostructure growth, the atoms reduced from the precursors can be considered as the reactants of a chemical reaction and the terminal nanostructures are the products of the chemical reaction.<sup>[12]</sup> Therefore, the deposition rate of atoms on the seed is similar with the reaction rate of a chemical reaction, which is highly dependent on the reaction temperature. In a common chemical reaction, the reaction rate follows the rule of Arrhenius equation, that is:

$$v = Ae^{-\frac{E_a}{RT}} \quad (3.4)$$

where  $v$  is the rate constant of a chemical reaction,  $A$  is a pre-exponential factor,  $E_a$  is the activation energy,  $R$  is the universal gas constant, and  $T$  is the absolute temperature. According to this equation, the effects of varying growth temperature on the atom deposition rates can be observed during the process of nanostructure growth. Generally, the stable seeds are bounded by three types of stable facets, including  $\{100\}$ ,  $\{110\}$ , and  $\{111\}$ , and the surface energies on these three different types of facets are different with an order of  $\{110\} > \{100\} > \{111\}$ ,<sup>[23]</sup> leading to the temperature variations having different effects on the deposition rates of different facets. Since the ratios among growth rates of different facets determine the final morphology of a nanostructure, the terminal shape is tremendously dependent on the temperature.

The effects of different growth temperatures have been assessed in a series of experiments. The UV/Vis/NIR spectrophotometry was firstly used to measure the extinction spectra of the resulting products, a slow blue-shift was found when increasing the growth temperature (Figure 3.5a). This behavior is expected since the LSPR property is highly dependent on the size and morphology of nanostructures. SEM and TEM imaging were performed to characterize the sizes and morphologies of the nanostructures obtained at 25 °C, 45 °C, and 95 °C (Figure 3.5b–g, Figure 3.6), respectively. The images clearly show that the nanostructures obtained at 25 °C and 45 °C are tris octahedrons with average sizes of  $113 \pm 6$  nm and  $114 \pm 6$  nm, respectively. In order to find out why the nanostructures obtained at 25 °C and 45 °C

possess different extinction peaks while they have similar morphologies and sizes, the dihedral angles were measured. It is interesting to find that the angles are different, the average dihedral angle of trisioctahedrons obtained at 25 °C is  $161 \pm 3^\circ$  while it is  $163 \pm 3^\circ$  for the trisioctahedrons acquired at 45 °C. The increase of the dihedral angle means that the facet indexes of nanostructures obtained at various temperatures are different. According to the measured angles, the index for the trisioctahedrons obtained at 25 °C is around  $\{441\}$ , however, the index for the trisioctahedrons obtained at 45 °C is approximately  $\{551\}$ . The finite element method simulation results demonstrated that the extinction peak gradually blue shifts as the indices varies from  $\{221\}$  to  $\{661\}$ , which is in agreement with the experimental results, the extinction peak changed from 590 nm to 583 nm when the Miller indices varied from  $\{441\}$  (synthesized at 25 °C) to  $\{551\}$  (prepared at 45 °C).

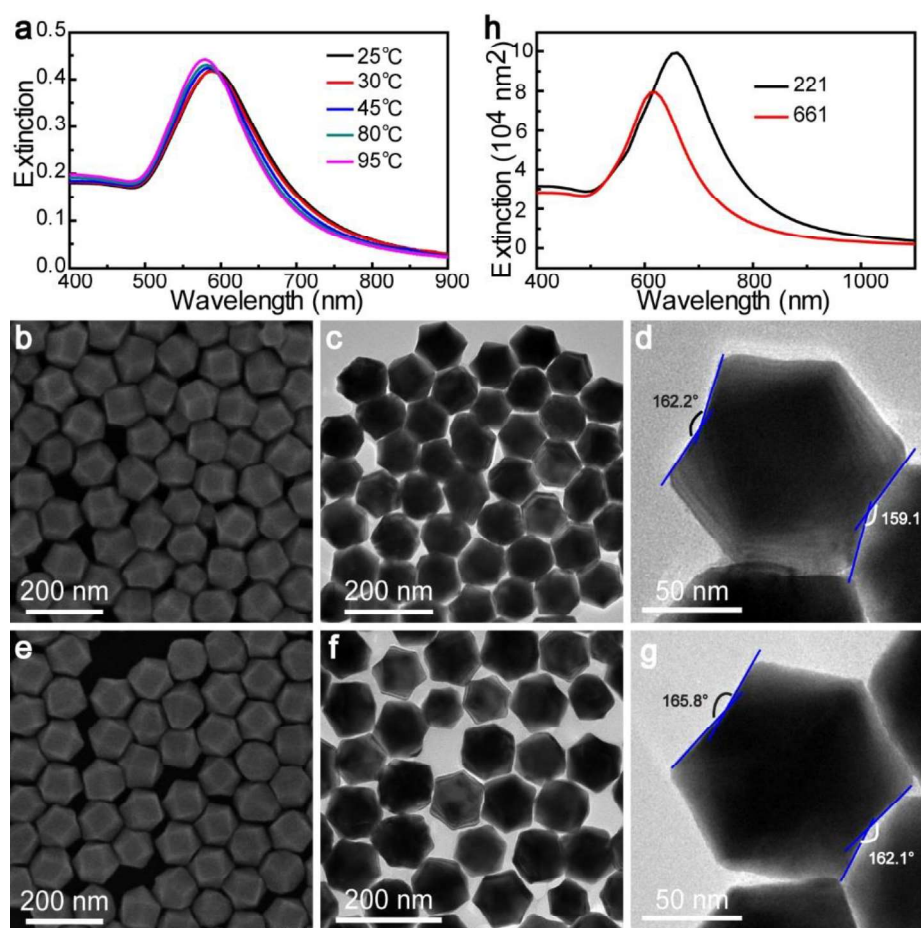


**Figure 3.5** The influence of growth temperature on the final products. (a) Extinction spectra of gold trisioctahedrons obtained at different growth temperature. SEM image (b) and TEM images (c–d) of gold trisioctahedrons obtained at 25 °C. SEM image (e) and TEM images (f–g) of gold trisioctahedrons obtained at 45 °C. (h) Simulated

*extinction spectra of gold trisoctahedrons with facets of  $\{221\}$  and  $\{661\}$ . The simulation data is kindly provided by Dr. Alexandre Baron and Mr. Florian Lochon in University of Bordeaux.*

When the growth temperature increased to 95 °C, the morphology of the obtained nanostructures is rhombic dodecahedron with  $\{110\}$  facets instead of trisoctahedron. In Figure 3.6a and d, the lower-magnification SEM and TEM images are presented to illustrate the orderly distributed gold rhombic dodecahedrons. Most of the nanoparticles follow the orientation that one of the vertices with three facets meet at their obtuse angles is in the center. The higher-magnification SEM and TEM images in Figure 3.6b and e unambiguously illustrate the orientation of gold rhombic dodecahedrons. Other directions were also found during SEM and TEM imaging, for example, the nanostructure with the orientation that one rhombic face is perpendicular with our view (Figure 3.6c and f).

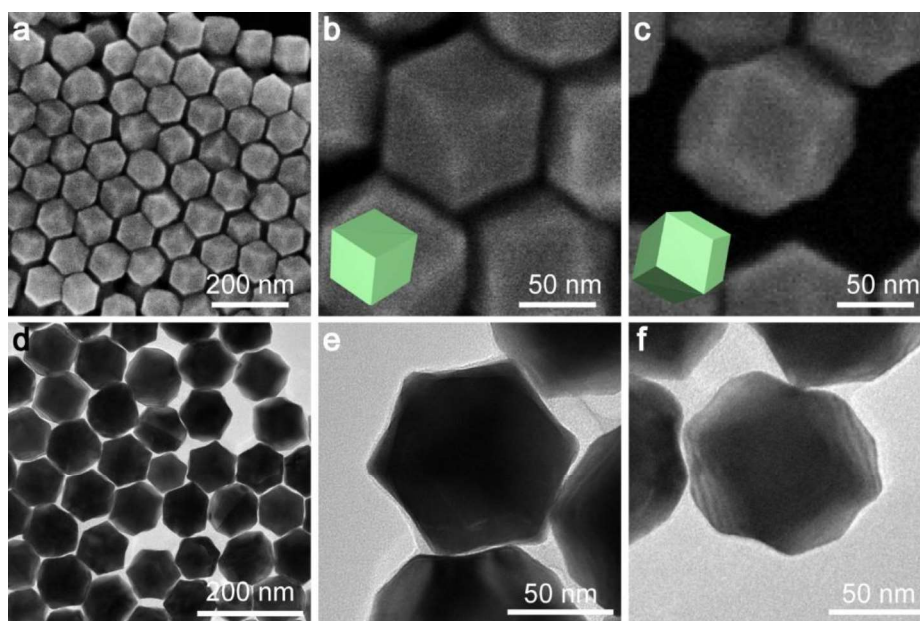


**Figure 3.6** SEM images (a–c), and TEM images (d–f) of nanostructures obtained at 95 °C.

#### **Concentration of ascorbic acid**

The concentration of reducing agent (such as AA) in the growth solution is an important factor for influencing the final nanostructures as well. The reducing rate of gold precursor ( $\text{HAuCl}_4$ ) will increase when the concentration of AA increases, therefore, the deposition rate of gold atoms will rise. To understand how this change in deposition rate affects the final nanoparticle shape and size, a set of experiments

were conducted employing different amount of AA in the growth solution while keeping other conditions the same.

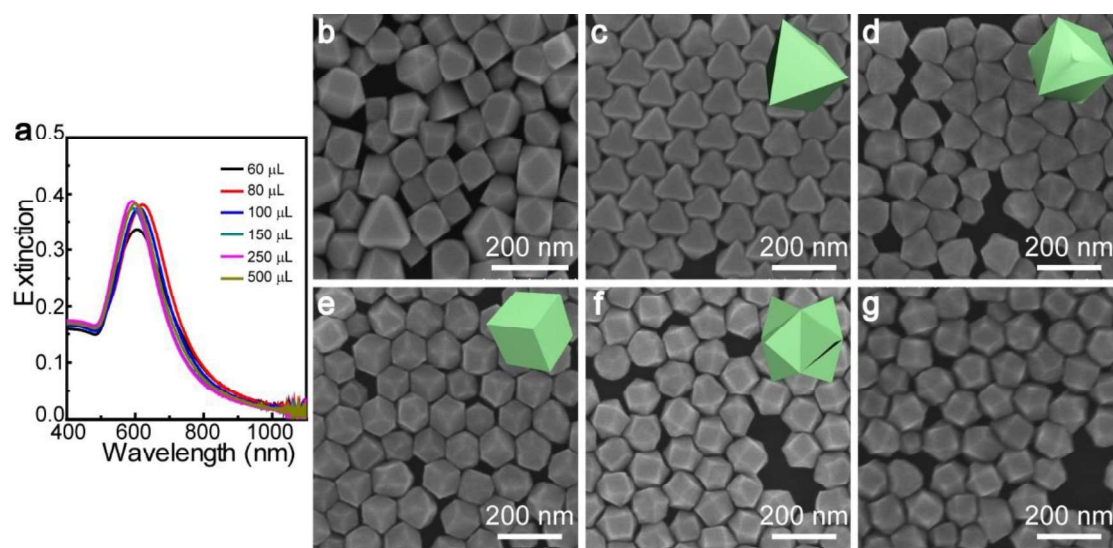


**Figure 3.7** The product variations with varying amounts of reduction agent in the growth solution. (a) Extinction spectra of the nanostructures synthesized with different amount of AA in the growth solution. (b–g) SEM images of gold nanocrystals obtained with 60  $\mu\text{L}$ , 80  $\mu\text{L}$ , 100  $\mu\text{L}$ , 150  $\mu\text{L}$ , 250  $\mu\text{L}$ , and 500  $\mu\text{L}$  of AA in the growth solution, respectively.

The extinction spectra of the resulting gold nanostructure colloids are different, which illustrates that the amount of the AA in growth solution affects the final size or morphology of nanostructures (Figure 3.7a). If only 60  $\mu\text{L}$  of AA was injected into growth solution, the reduction rate of  $\text{HAuCl}_4$  was very slow and thus the gold atoms preferred to deposit on the  $\{110\}$  facets with higher free surface energy in comparison with that of  $\{100\}$  and  $\{111\}$ , resulting in the final morphology was cuboctahedron with six  $\{100\}$  facets and eight  $\{111\}$  facets (Figure 3.7b). The SEM image also illustrates that the obtained cuboctahedron has a wide size dispersity. Furthermore, some other morphologies like octahedron are found in the product. The probable reason is that the concentration of reducing agent is able to cause some atoms to be deposited on  $\{100\}$  facets as well. When increasing the amount of AA solution to 80  $\mu\text{L}$ , most of the obtained nanostructures are gold octahedrons. At this amount of AA, the growth occurred on both  $\{110\}$  and  $\{100\}$  facets, leading to gold octahedron with eight  $\{111\}$  facets formed (Figure 3.7c). Octahedron with a bump on each facet will be formed if keeping increasing the amount of AA, Figure 3.7d is an example when the volume of AA is 100  $\mu\text{L}$ . As the volume of AA was increased to 150  $\mu\text{L}$ , rhombic

dodecahedrons with  $\{110\}$  facets were observed (Figure 3.7e). The interested morphology with very high purity, trisoctahedrons, can be obtained when the AA increased to 250  $\mu\text{L}$  (Figure 3.7f). Further increasing the amount of the AA solution in growth solution to 500  $\mu\text{L}$  did not cause further changes to morphology (Figure 3.7g).

### ***Surfactant***

Surfactant, also named as capping agent, is a key agent in the growth solution for the synthesis of nanostructures and plays essential roles in controlling the terminal shape of the product.<sup>[24]</sup> Indeed, from a kinetic point of view, the surfactant chemisorbed on a facet can slow down or even prohibit the atom deposition onto this facet, and this resulted slower growth rate will lead to this facet accounting for a greater proportion on the final surface. On the other hand, the thermodynamic view indicates that surfactant can alter the distribution of surface free energies and thus selectively stabilize some facets on a nanostructure. Therefore, it is important to select the concentration and type of surfactant.

The use of CTAC as surfactant is beneficial for the formation of trisoctahedrons in the absence of silver ions,<sup>[25]</sup> and therefore it was my first choice to use CTAC as the capping agent to prepare gold trisoctahedrons. After carrying out a set of experiments with different concentration of CTAC, I observed a significant influence of the CTAC concentration on the final shape and size of the resulting nanoparticles, as presented in Figure 3.8. The differences in extinction spectra of the obtained colloid nanostructures illustrate the variability of the obtained nanostructures (Figure 3.8a). It should be pointed out that when the CTAC concentration lower to 1 mM, the gold precursor can be reduced to gold atoms immediately by AA and form nanoparticles directly without seed. Nanoclusters were observed in this directly formed product (Figure 3.8b). When the concentration of CTAC increased to or higher than 5 mM, a certain amount of seed solution needs to be added into growth solution for acquiring nanostructures. SEM imaging showed that gold trisoctahedrons can be obtained when the concentration of CTAC is between 5 mM and 25 mM (Figure 3.8c and d). Gold rhombic dodecahedral structures appeared as the concentration of CTAC increased to 50 mM (Figure 3.8e). Most of the nanostructures in product were rhombic dodecahedron with 100 mM CTAC as surfactant (Figure 3.8f). These results show that CTAC preferentially binds to  $\{110\}$  facets and thus results in the formation of rhombic dodecahedrons with  $\{110\}$  facets. Trisoctahedrons can be formed at low

concentration of CTAC because the low concentration is not enough to stop the growth of  $\{110\}$  facets and the growth on  $\{110\}$  facets can compete with that on  $\{100\}$  and  $\{111\}$  facets. However, the product is not uniform when the concentration of CTAC continued to increase to 250 mM (Figure 3.8g) as the high concentration of CTAC greatly slow down the deposition of atoms onto all facets.

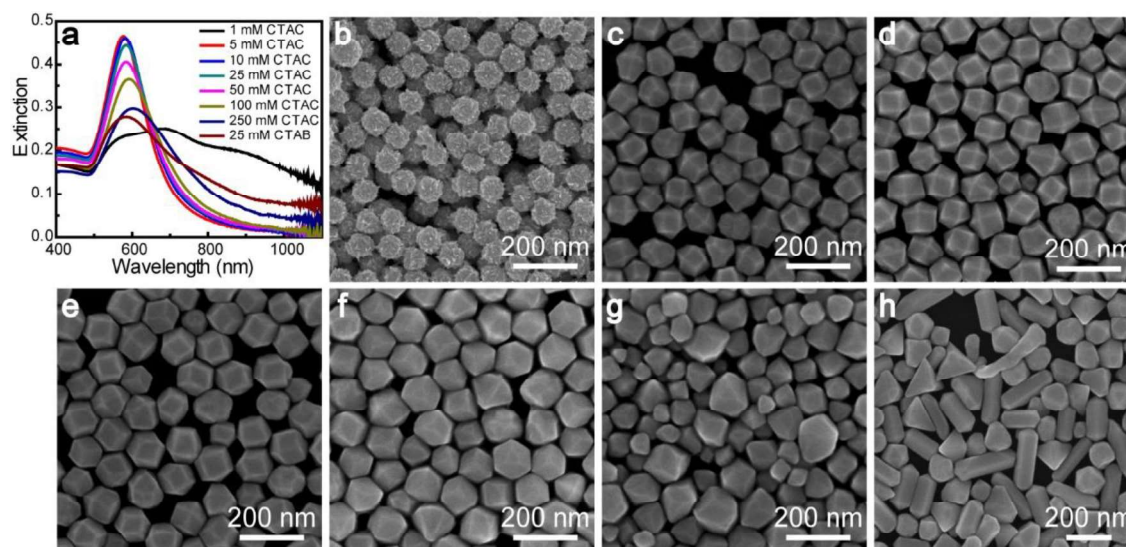


**Figure 3.8** The effect of the surfactants in the growth solution on the final products. (a) Extinction spectra of colloid nanocrystals obtained with different concentrations of CTAC and 25 mM CTAB. (b–g) SEM images of nanostructures grown with 1 mM, 5 mM, 25 mM, 50 mM, 100 mM, and 250 mM of CTAC, respectively. (h) SEM image of nanostructures obtained in the presence of 25 mM CTAB.

CTAB is also a commonly used surfactant for obtaining nanostructures like gold nanorods<sup>[8]</sup> and gold nanobipyramids,<sup>[18]</sup> thus, the effect of replacing CTAC by CTAB in the growth solution on the final nanostructures was also assessed while keeping the other experimental conditions the same. The resulting product, presented in Figure 3.8h, contains rodlike, prism and irregular nanostructures instead of trisoctahedrons, demonstrating that the  $\text{Cl}^-$  ions play a vital role in preparing trisoctahedrons. The difference of products by employing CTAC and CTAB as surfactants is caused by the different affinities of these two surfactants, generally,  $\text{Br}^-$  ions exhibit stronger binding to gold surfaces than  $\text{Cl}^-$  ions.<sup>[23]</sup>

#### ***The function of $\text{H}_2\text{PtCl}_6$ in growth solution***

The introduction of foreign metal ions in the growth solution has been demonstrated to be an effective method to prepare nanostructures with high-index

facets, as they deposit on some facets to slow or stop the further growth of these facets.<sup>[11, 26]</sup> These foreign ions like  $\text{Ag}^+$  are called shape-directing agents, and have been successfully employed to synthesize many types of nanostructures with high surface energy, including gold tetrahedral nanostructures,<sup>[27]</sup> gold concave cubes,<sup>[28]</sup> gold truncated ditetragonal prisms,<sup>[29]</sup> and so on. Interestingly, I found that  $\text{PtCl}_6^{2-}$  can improve the purity of gold trisectahedrons in my study. Only 5  $\mu\text{L}$   $\text{H}_2\text{PtCl}_6$  (0.01 M) in 10 mL growth solution is able to cause a dramatic change in the final results. Figure 3.9a displays the comparison of extinction spectra of the products synthesized with and without  $\text{H}_2\text{PtCl}_6$ , the plasmonic peaks are almost the same for these two products, however, the spectrum intensity is higher for the product prepared without  $\text{H}_2\text{PtCl}_6$  when the wavelength is longer than 700 nm. Further evidence of the impact is obtained via SEM and TEM imaging, demonstrating that there are some bipyramids in the obtained product prepared without  $\text{H}_2\text{PtCl}_6$  (Figure 3.9b and c). Since bipyramids possess longitudinal plasmonic peaks located at the longer wavelength, the bipyramids in the product synthesized without  $\text{H}_2\text{PtCl}_6$  can lead to higher extinction intensity at longer wavelength region. The reason for the higher purity when synthesized with  $\text{H}_2\text{PtCl}_6$  in growth solution is probably because Pt atoms preferentially deposited on the facets with high surface energy and thus block these facets to continue to grow resulting in the formation of nanostructures with high-index facets rather than bipyramid with  $\{111\}$  facets which have low surface energy.

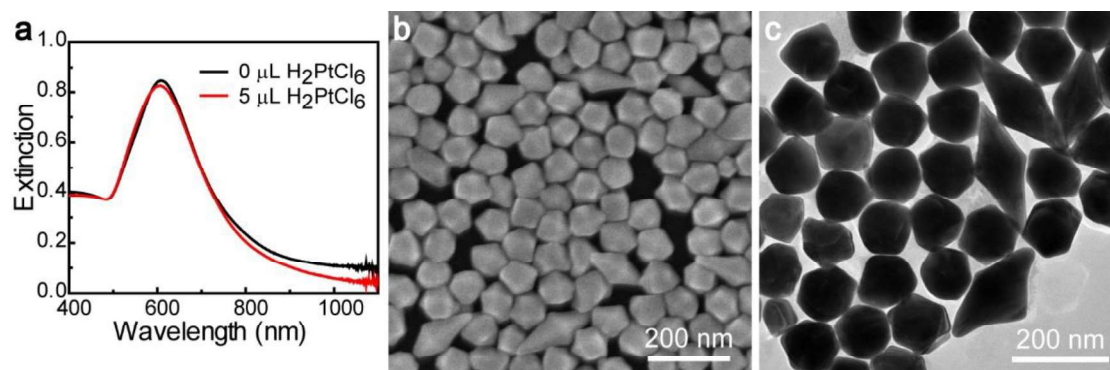


**Figure 3.9** The effect of introducing  $\text{H}_2\text{PtCl}_6$  in the growth solution on the final morphology of the products. (a) Extinction spectra of colloid nanocrystals obtained with and without  $\text{H}_2\text{PtCl}_6$  in the growth solution. SEM (b) and TEM (c) images of nanostructures synthesized without  $\text{H}_2\text{PtCl}_6$  in the growth solution.

***Monitoring the growth process***

In seed-mediated methods, the formation of seed plays an essential role in determining the final morphology of nanostructures. To obtain nanostructures with high purity, it is important to find the optimal formation time for seeds. For example, the seed solution for synthesizing gold nanorods needs to be kept undisturbed at room temperature for around 2 h.<sup>[8]</sup> Another typical example is the seed solution for preparing gold nanobipyramids that needs to be treated for 90 min at 80 °C.<sup>[18]</sup> In my study, I also investigated the change of the final nanostructure as the time of seed formation prolonged. Since the LSPR property of nanostructures is highly sensitive to their morphologies and sizes, UV/Vis/NIR spectrophotometry was used for monitoring the variations of seed solution by recording the extinction spectra (Figure 3.10a). The extinction spectrum changed significantly within the first 30 min and then changed slowly from 30 min to 24 h. I used seed solutions at different reaction times (1 min, 3 h and 24 h) to synthesize gold trisioctahedrons and the results show that longer aging time led to a redshift of the plasmonic peak and a lower peak intensity (Figure 3.10b). The SEM analysis of the samples showed that all the products are gold trisioctahedrons but differ in size (Figure 3.10c–e), which can explain the difference observed in the plasmonic peaks. Compared Figure 3.10e with Figure 3.10c, it is unambiguous that the gold trisioctahedrons obtained with seeds at 24 h is much larger than that obtained with seeds at 1 min. This change is likely related to the decrease of seed number in the seed solution by increasing the reaction time due to the Ostwald ripening effect.<sup>[30]</sup>

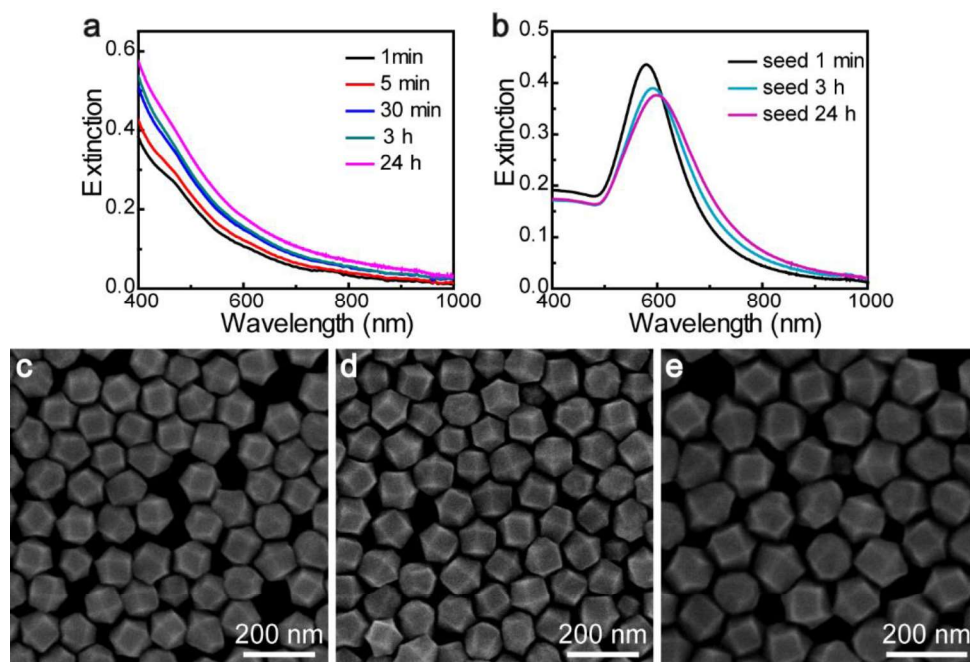


**Figure 3.10** The nanostructures prepared with seed solutions of varying reaction times. (a) Extinction spectra of seed solutions with various reaction times. (b) Extinction spectra of the obtained nanostructures prepared using seeds at different reaction time. (c–e) SEM images of the obtained nanostructures synthesized with the seeds at different reaction time as in (b), the reaction times of seed solutions are 1 min, 3 h, and 24 h, respectively.

One of the key advantages of my method is that the completion of the reaction is achieved in about 7 min. To determine the time of completion, the extinction spectra has been acquired for different reaction times. Presented in Figure 3.11a, a steady redshift over time and a gradual increase of peak intensity can be observed. After 7 min, the spectra at subsequent reaction times perfectly overlap, indicating that the growth process had finished. SEM imaging was performed to explain the variations of extinction spectra as the reaction time prolonged. The growth solution was centrifuged after adding seed solution into growth solution for 20 s, and it took 3 min to centrifuge the growth solution. The resulting product was shown in Figure 3.11b, the SEM image clearly demonstrates that gold trisioctahedrons have already been formed in such short reaction time. As the reaction time increased from 20 s to 7 min, only the size slowly increased, the morphology did not change (Figure 3.11b–d). The variations of acquired nanostructures were illustrated in Figure 3.11e. The gold nanocrystals grew into trisioctahedrons quickly and then became larger and larger.

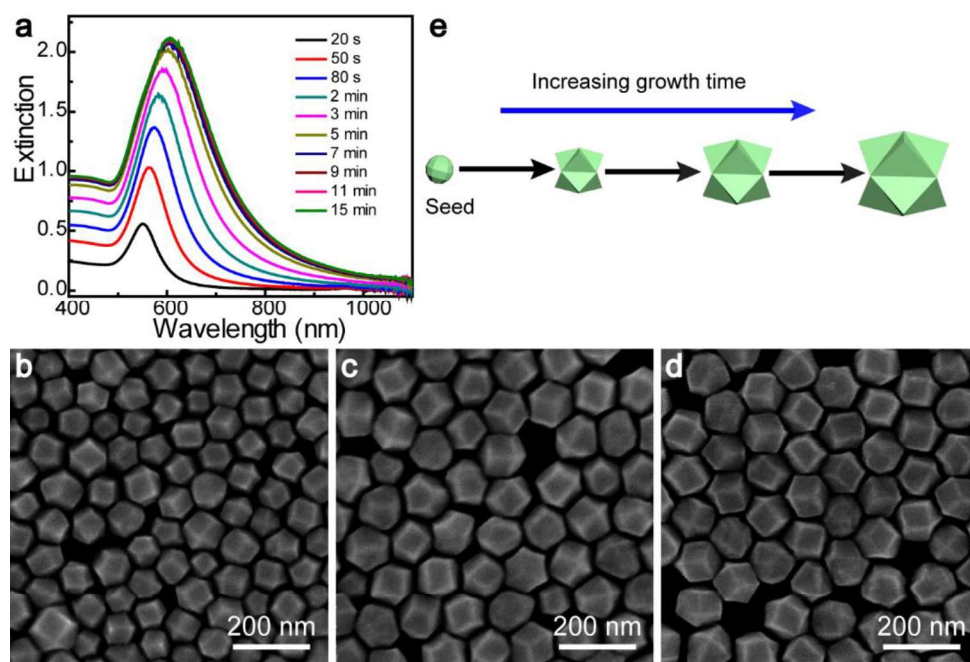


**Figure 3.11** The variations of gold trisioctahedrons as the reaction time prolonging. (a) Extinction spectra recorded during the preparation of gold trisioctahedrons at different growth times. (b–d) SEM images of the obtained products collected at 20 s, 3 min, and 7 min, respectively. It took three minutes to centrifuge each sample. (e) Schematic displaying the growth process of gold trisioctahedron as the reaction time prolonging.

The above description demonstrates that this seed-mediated method for synthesizing gold trisioctahedrons is very fast. The seed can be used immediately after adding sodium borohydride into seed solution, and the entire growth process from seed to final nanostructure only takes 7 min.

## 3.2 Outstanding Properties of Gold Trisioctahedrons

### 3.2.1 Refractive index sensitivity

As mentioned in Chapter 1, the LSPR properties of noble metal nanocrystals are greatly sensitive to the refractive index of the medium surrounding them. Generally, the increase of the index induces a red shift of the plasmonic peak, especially in the nanostructures with sharp tips and edges exhibiting strong sensitivities. This intriguing property endows noble metal nanoparticles with biosensing potential.<sup>[31–32]</sup> Hence, preparing noble metal nanoparticles with high refractive index sensitivity is of

great significance. Gold trisectahedron with 14 sharp tips and 24 edges provides many sensitive sites, and thus will be an interesting candidate for sensing the variation of refractive index. In my study, three samples of gold trisectahedrons with different sizes were prepared for characterizing their sensing abilities. Their plasmonic peaks are located at 605 nm (sample 1), 580 nm (sample 2), 570 nm (sample 3), respectively (Figure 3.12a). Figure 3.12b–d are their corresponding SEM images.

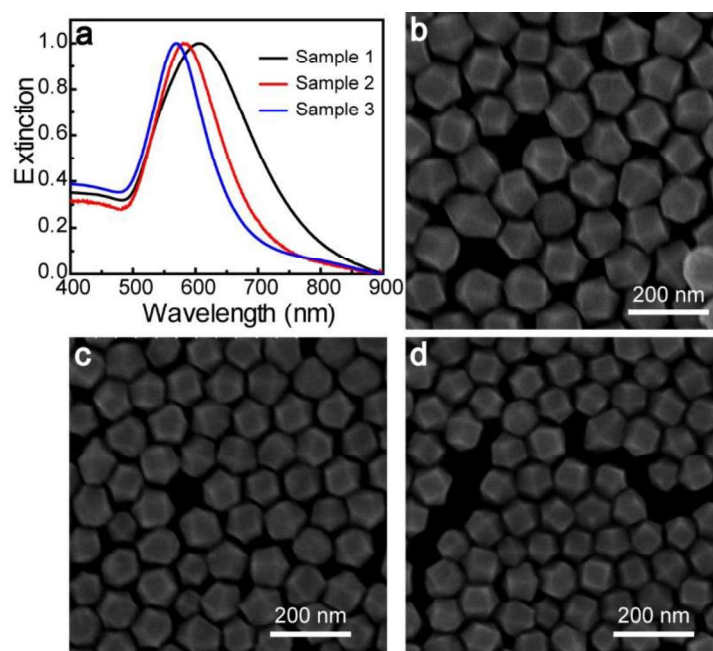


**Figure 3.12** Extinction spectra (a) and SEM images (b–d) of three trisectahedron samples for measuring the refractive index sensitivities, sample 1, sample 2, sample 3, respectively.

Bulk sensitivity measurements were performed by dispersing the gold trisectahedrons into liquid medium with different refractive indices. The refractive index was gradually varied by mixing glycerol with water whose refractive indices are 1.4746 and 1.3334, respectively. The volume percentage of glycerol in the water-glycerol mixtures was varied from 0% to 81% in a step of 9% to produce a gradual increase of refractive index. Figure 3.13a–c display that the extinction spectra of as-prepared three gold trisectahedron samples slowly red shift as the increase in refractive index of surrounding mediums. The variations of the LSPR peak positions were plotted as the function of the refractive index for all the three samples, and all these three trisectahedrons exhibit good linear fits (Figure 3.13d). The refractive index sensitivities determined by the slopes of the fitting lines are 265 nm/RIU, 199 nm/RIU, and 158 nm/RIU for sample 1, sample 2, and sample 3, respectively. Moreover, the

values of  $FOM$  (defined in Chapter 1) are 1.43, 1.53 and 1.38, respectively. These results demonstrate that larger nanoparticles possess higher sensitivity but lower  $FOM$  value because of the broader  $FWHM$  value.

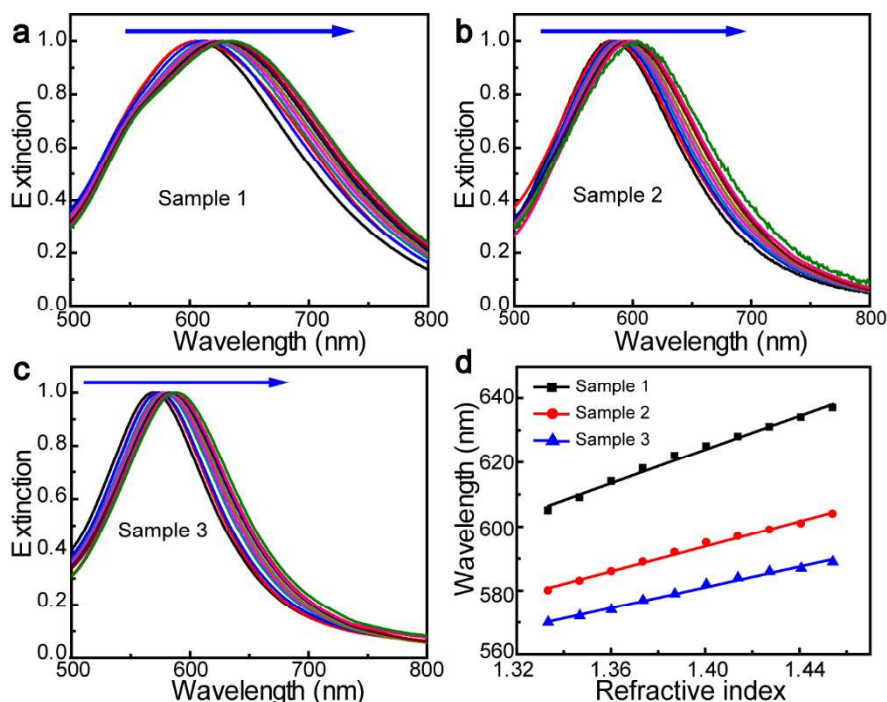


**Figure 3.13** Refractive index sensitivities of different gold trisioctahedrons in water-glycerol mixtures. (a–c) Normalized extinction spectra of the three trisioctahedrons dispersed into water-glycerol mixtures of varying compositions. The blue arrows indicate the direction of increasing refractive index. (d) Dependence of the plasmonic peak shift on the refractive index of surrounding medium for the three trisioctahedron samples.

The refractive index sensitivity of gold nanospheres with a plasmonic peak at 572 nm, having a similar plasmonic peak position with that of sample 3, was tested for comparison. In order to compare the sensitivities, the data of gold nanospheres was plotted together with that of sample 3. Figure 3.14a is the extinction spectra of gold nanospheres and sample 3, the spectrum of nanospheres showing a wider plasmonic peak. The corresponding sizes measured from TEM images are  $103 \pm 3$  nm and  $96 \pm 8$  nm for gold nanospheres and sample 3, respectively, the representative TEM images are shown in Figure 3.14b and c. The result of size difference is in agreement with the view mentioned in Chapter 1 that two nanostructures of different sharpness exhibiting the same plasmonic peak position have different sizes. The above-described method for varying the refractive index of surrounding medium was applied to gold

nanospheres and the positions of the LSPR peaks were measured. The experimental results obtained for gold nanospheres in Figure 3.14d shows the redshift of LSPR peak. The plots of plasmonic peaks as the functions of their surrounding refractive index, shown in Figure 3.14e, demonstrate that gold nanospheres have a lower refractive index sensitivity (141 nm/RIU). Gold trisectahedrons exhibit only slightly higher refractive index sensitivity is likely related to the size since the gold trisectahedrons are about seven nanometers smaller than gold nanospheres although they have similar plasmonic peak positions. In addition, since the plasmonic peak of gold nanospheres is wider, the  $FOM$  value (1.06) is lower. The comparison indicates that gold trisectahedrons are undoubtedly better candidates for plasmonic sensing applications than gold nanospheres.

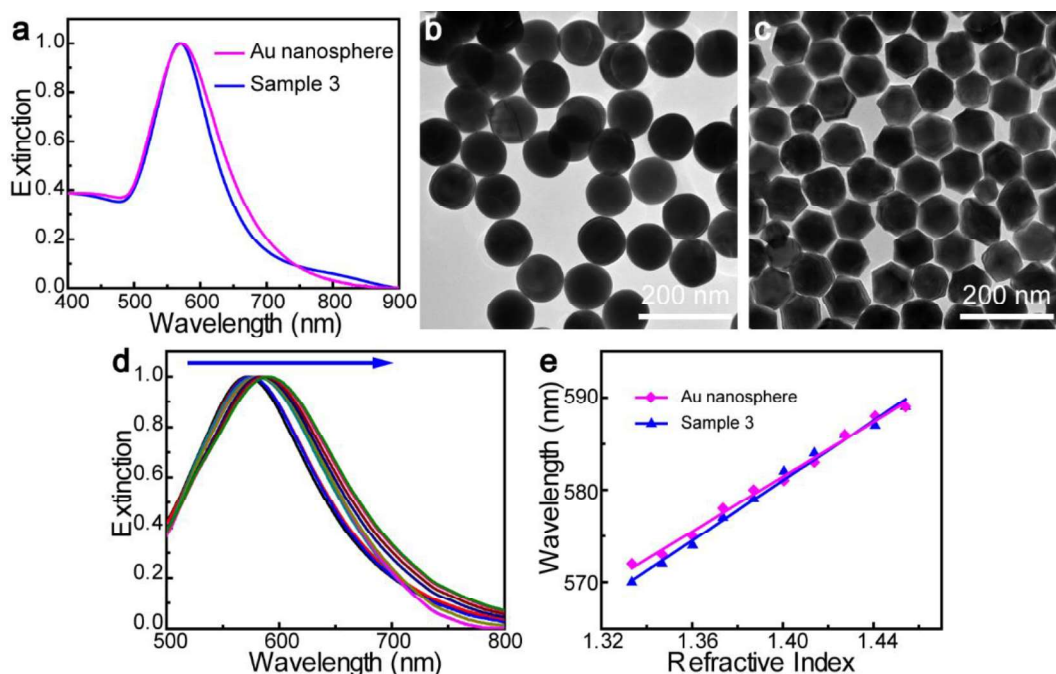


**Figure 3.14** The comparison of the refractive index sensitivities between gold nanospheres and gold trisectahedrons in water-glycerol mixtures. (a) Extinction spectra of gold nanospheres and sample 3 (gold trisectahedrons) dispersed into water, respectively. (b–c) TEM images of gold nanospheres and sample 3 (gold trisectahedrons), respectively. (d) Normalized extinction spectra of gold nanospheres dispersed in water-glycerol mixtures of varying compositions. The blue arrow indicates the direction of increasing refractive index. (e) LSPR peak shift versus refractive index of surrounding medium for gold nanospheres and sample 3 (gold trisectahedrons).

Finite element method simulation was used to calculate the near-field enhancements of an individual gold trisoctahedron and a single nanosphere for confirming that gold trisoctahedron exhibits a higher enhancement of electromagnetic field, thus leading to higher plasmonic sensitivity. In the simulation, a gold trisoctahedron and a gold nanosphere with the same size (56 nm) were applied. The simulation results shown in Figure 3.15 unambiguously demonstrates that the electric field enhancement of gold trisoctahedron is much higher than that of gold nanosphere.

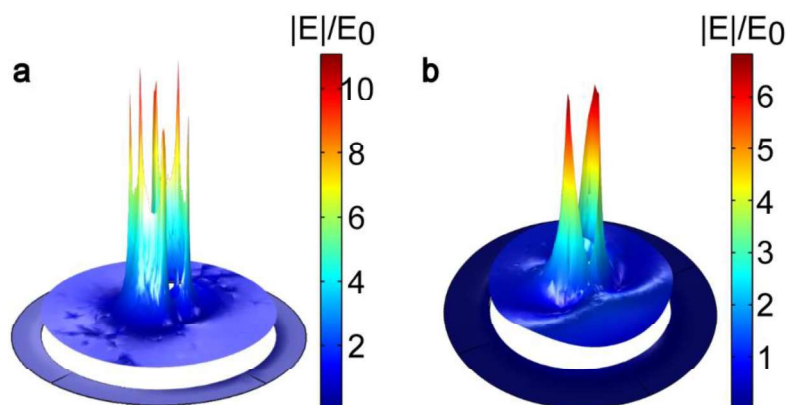


**Figure 3.15** The calculated electric field enhancement contours of an individual gold trisoctahedron (a), and a single gold nanosphere (b) by finite element method. The simulation data is kindly provided by Dr. Alexandre Baron and Mr. Florian Lochon in University of Bordeaux.

### 3.2.2 Surface-enhanced Raman spectroscopy

Gold trisoctahedrons have been reported to exhibit efficient SERS activities because of their well-defined tips, edges, steps and kinks with high free energy on their surfaces as well as their interparticle gaps.<sup>[14, 33]</sup> To attest the SERS efficiency of gold trisoctahedrons, three gold trisoctahedron samples were prepared. The SERS properties of as-prepared gold trisoctahedrons were evaluated by measuring the Raman spectra of 2-NaT adsorbed on the gold trisoctahedrons. Specifically, the colloids of gold trisoctahedrons (10 mL) were firstly washed twice by deionized water to remove the surfactant as much as possible. Then the gold trisoctahedrons were redispersed into deionized water (10 mL) and mixed with 2-NaT molecules dissolved into ethanol (20  $\mu$ L, 0.01M). The resultant mixtures were left at room temperature for at least 2 hours to ensure complete chemisorption. Subsequently, the mixtures were centrifuged to remove the unbounded molecules and redispersed into different volumes of deionized water for measuring SERS spectra. The SERS measurements

were carried out on a Raman microscope (HORIBA, LabRAM HR) equipped with a CCD camera (Synapse, HORIBA JOBIN YVON), a 600 grooves/mm diffraction grating, and a red laser with 633 nm for exciting the samples. The Raman spectra of the aqueous gold trisioctahedrons were collected by employing a quartz cuvette with 1 cm optical length as a container, a laser power of 3 mW, a 10× objective lens (NA = 0.25), and the integration time of 20 s.

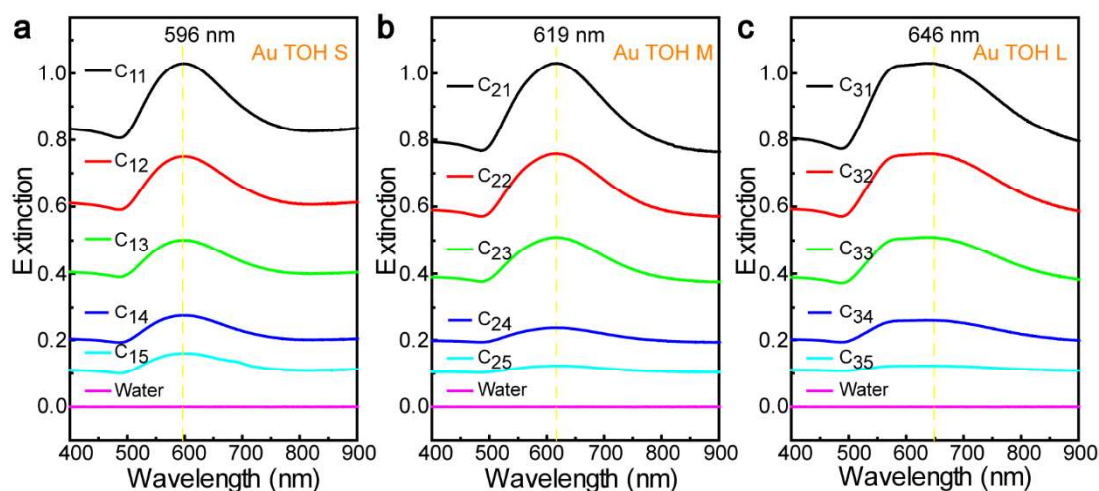


**Figure 3.16** Extinction spectra of different concentrations of three gold trisioctahedron samples adsorbed with 2-NaT molecules for SERS measurements. *C* represents the concentration of gold trisioctahedron particles.

As seen from equation (2.3) in Chapter 2, the intensity of extinction is linearly dependent on the particle concentration for a given nanostructure. Therefore, the particle concentration can be known from the intensity of the extinction peak. Figure 3.16 shows the extinction spectra of varying concentrations of the three gold trisioctahedron samples adsorbed with 2-NaT molecules, the plasmonic peaks being located at 596 nm (Au TOH S), 619 nm (Au TOH M), and 646 nm (Au TOH L), respectively. The Raman spectra of these three samples were measured by the above-described approach. As displayed in Figure 3.17, several characteristic signals were observed in the Raman spectra. Typically, the peaks located at  $1382.8\text{ cm}^{-1}$  and  $1619.2\text{ cm}^{-1}$  are attributed to the ring modes, the C-H bending mode is located at  $1069\text{ cm}^{-1}$ , and the peak at  $769.3\text{ cm}^{-1}$  is dominated by the ring deformation.<sup>[34–35]</sup> It is unambiguously seen that the intensities of these peaks slowly decreased with the decreases of the particle concentrations because of the decrease in the total number of measured molecules. The peak at  $1382.8\text{ cm}^{-1}$  was chosen to investigate the variations of the peak intensity as the change of particle concentration. The integrated area of the

peak was plotted as the function of the peak intensity of extinction spectrum (Figure 3.18). Clearly, the integrated areas of the Raman peak for all the three samples are linearly dependent on the extinction intensities. It appears that Au TOH S has highest Raman signal among these three samples when they have the same extinction intensity. The slope of the fitting line is highest for Au TOH S, which means that the Raman signal of Au TOH S is the most sensitive one with respect to the changes in extinction intensity. This result is probably related with the variations of the particle concentration, because Au TOH S is the smallest particle with smallest cross-section among these three samples,<sup>[36]</sup> it must have the largest particle concentration for a given extinction intensity according to equation (2.3). Among all the SERS measurements, the lowest extinction intensity was 0.0156 for Au TOH L, the cross-section calculated from finite element method simulation is  $9.90 \times 10^4 \text{ nm}^2$ , hence, the lowest particle concentration can be measured is  $3.63 \times 10^8 \text{ NP mL}^{-1}$ .

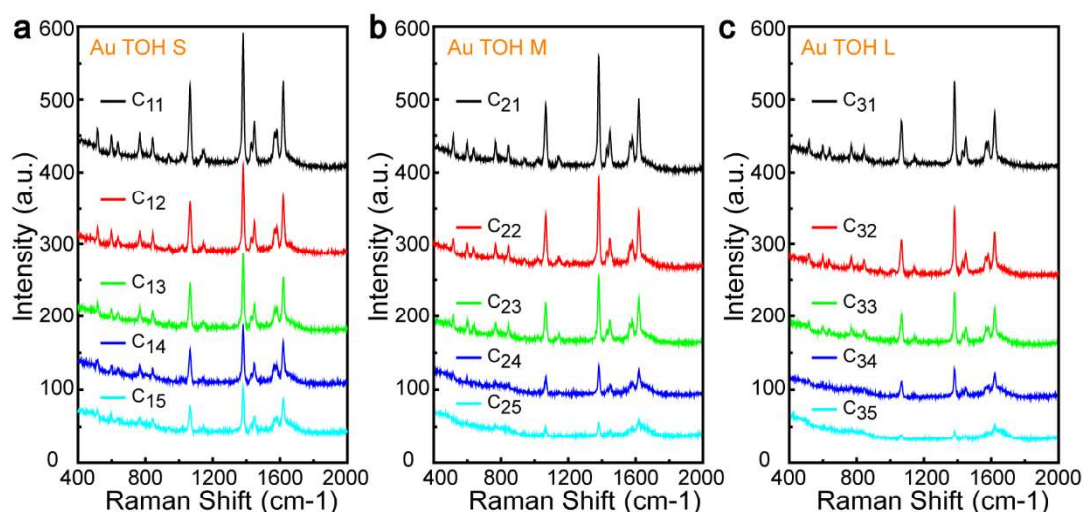


**Figure 3.17** Raman spectra of different concentrations of three gold trisoctahedron samples adsorbed with 2-NaT molecules. C represents the concentration of gold trisoctahedron particles.

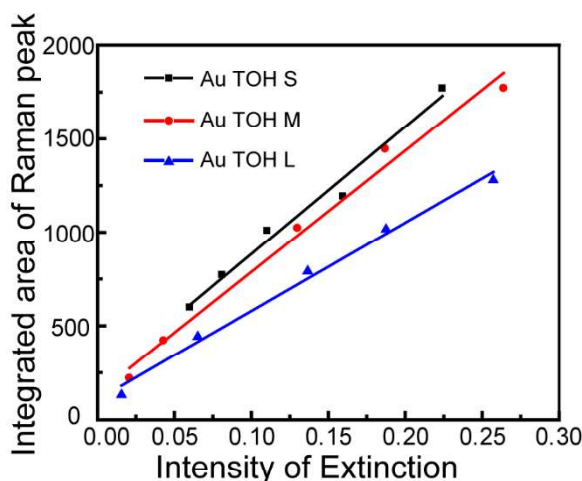


**Figure 3.18** The plots of the integrated area of Raman peak located at  $1382.8\text{ cm}^{-1}$  as a function of the extinction intensity for three trisioctahedron samples.

### 3.3 Summary

In this chapter, I have provided a facile and fast approach for the growth of uniform gold trisioctahedrons with controllable sizes and dihedral angles. The sizes can be tailored by simply controlling the amount of seed solution in the growth solution. By improving the growth temperature, the dihedral can be gradually increased from  $161^\circ$  which means the Miller indices of the facets of the obtained nanostructures can be tuned from  $\{441\}$  to the limit case  $\{110\}$ . Furthermore, sets of optimizing experiments were carried out, including different concentrations of AA, various of concentrations and types of surfactants, and the effect of  $\text{H}_2\text{PtCl}_6$  as the shape-directing agent. Moreover, the experiments of monitoring the growth process demonstrated that the seed solution can be used immediately after injecting sodium borohydride and the following growth process is able to finish in 7 min. The high plasmonic sensitivity and high SERS performance of gold trisioctahedrons caused by the well-defined tips and edges were demonstrated as well. I believe that the facile and fast synthesize method will promote the potential applications of gold trisioctahedrons in plasmonic and catalytic areas.

### References

- [1] Y. Y. Ma, Q. Kuang, Z. Y. Jiang, Z. X. Xie, R. B. Huang, L. S. Zheng, *Angew. Chem. Int. Ed.* **2008**, *47*, 8901–8904.

- [2] Y. J. Xiong, B. J. Wiley, Y. N. Xia, *Angew. Chem. Int. Ed.* **2007**, *46*, 7157–7159.
- [3] Q. Li, X. L. Zhuo, S. Li, Q. F. Ruan, Q. -H. Xu, J. F. Wang, *Adv. Optical Mater.* **2015**, *3*, 801–812.
- [4] J. P. Xie, Q. B. Zhang, J. Y. Lee, D. I. C. Wang, *ACS Nano* **2008**, *12*, 2473–2480.
- [5] J. W. Hong, S. -U. Lee, Y. W. Lee, S. W. Han, *J. Am. Chem. Soc.* **2012**, *134*, 4565–4568.
- [6] C. -Y. Chiu, P. -J. Chung, K. -U. Lao, C. -W. Liao, M. H. Huang, *J. Phys. Chem. C* **2012**, *116*, 23757–23763.
- [7] B. Nikoobakht, M. A. El-Sayed, *Chem. Mater.* **2003**, *15*, 1957–1962.
- [8] A. Gole, C. J. Murphy, *Chem. Mater.* **2004**, *16*, 3633–3640.
- [9] C. C. Li, K. L. Shuford, M. H. Chen, E. J. Lee, S. O. Cho, *ACS Nano* **2008**, *2*, 1760–1769.
- [10] W. X. Niu, S. L. Zheng, D. W. Wang, X. Q. Liu, H. J. Li, S. Han, J. A. Chen, Z. Y. Tang, G. B. Xu, *J. Am. Chem. Soc.* **2009**, *131*, 697–703.
- [11] L. Zhang, W. X. Niu, G. B. Xu, *Nano Today* **2012**, *7*, 586–605.
- [12] Y. N. Xia, X. H. Xia, H. -C. Peng, *J. Am. Chem. Soc.* **2015**, *137*, 7947–7966.
- [13] Z. W. Quan, Y. X. Wang, J. Y. Fang, *Acc. Chem. Res.* **2013**, *46*, 191–202.
- [14] Y. H. Song, T. T. Miao, P. N. Zhang, C. X. Bi, H. B. Xia, D. Y. Wang, X. T. Tao, *Nanoscale* **2015**, *7*, 8405–8415.
- [15] D. Huo, H. M. Ding, S. Zhou, J. Li, J. Tao, Y. Q. Ma, Y. N. Xia, *Nanoscale* **2018**, *10*, 11034–11042.
- [16] Y. Yu, Q. B. Zhang, X. M. Lu, J. Y. Lee, *J. Phys. Chem. C* **2010**, *114*, 11119–11126.
- [17] M. A. Van Hove, G. A. Somorjai, *Surface Science* **1980**, *92*, 489–518.
- [18] A. Sanchez-Iglesias, N. Winckelmans, T. Altantzis, S. Bals, M. Grzelczak, L. M. Liz-Marzan, *J. Am. Chem. Soc.* **2017**, *139*, 107–110.
- [19] X. S. Kou, W. H. Ni, C. -Kuang Tsung, K. Chan, H. -Q. Lin, G. D. Stucky, J. F. Wang, *Small* **2007**, *3*, 2103–2113.
- [20] D. Chateau, A. Liotta, F. Vadcard, J. R. G. Navarro, F. Chaput, J. Lerme, F. Lerouge, S. Parola, *Nanoscale* **2015**, *7*, 1934–1943.
- [21] Q. F. Ruan, L. Shao, Y. W. Shu, J. F. Wang, H. K. Wu, *Adv. Optical Mater.* **2014**, *2*, 65–73.
- [22] B. -J. Liu, K. -Q. Lin, S. Hu, X. Wang, Z. -C. Lei, H. -X. Lin, B. Ren, *Anal. Chem.* **2015**, *87*, 1058–1065.

- [23] M. L. Personick, M. R. Langille, J. Zhang, N. Harris, G. C. Schatz, C. A. Mirkin, *J. Am. Chem. Soc.* **2011**, *133*, 6170–6173.
- [24] Y. F. Shi, Z. H. Lyu, M. Zhao, R. H. Chen, Q. N. Nguyen, Y. N. Xia, *Chem. Rev.* **2021**, *121*, 649–735.
- [25] S. E. Lohse, N. D. Burrows, L. Scarabelli, L. M. Liz-Marzan, *Chem. Mater.* **2014**, *26*, 34–43.
- [26] W. X. Niu, L. Zhang, G. B. Xu, *Nanoscale* **2013**, *5*, 3172–3181.
- [27] T. Ming, W. Feng, Q. Tang, F. Wang, L. D. Sun, J. F. Wang, C. H. Yan, *J. Am. Chem. Soc.* **2009**, *131*, 16350–16351.
- [28] M. L. Personick, M. R. Langille, J. Zhang, C. A. Mirkin, *Nano Lett.* **2011**, *11*, 3394–3398.
- [29] F. Lu, Y. Zhang, L. H. Zhang, Y. G. Zhang, J. X. Wang, R. R. Adzic, E. A. Stach, O. Gang, *J. Am. Chem. Soc.* **2011**, *133*, 18074–18077.
- [30] A. D. Brailsford, P. Wynblatt, *Acta Metallurgica* **1979**, *27*, 489–497.
- [31] S. M. Marinakos, S. H. Chen, A. Chilkoti, *Anal. Chem.* **2007**, *79*, 5278–5283.
- [32] K. M. Mayer, J. H. Hafner, *Chem. Rev.* **2011**, *111*, 3828–3857.
- [33] Q. Xu, W. Liu, L. Li, F. Zhou, J. Zhou, Y. Tian, *Chem. Commun.* **2017**, *53*, 1880–1883.
- [34] M. Roca, A. J. Haes, *J. Am. Chem. Soc.* **2008**, *130*, 14273–14279.
- [35] D. Zhu, Z. Y. Wang, S. F. Zong, H. Chen, P. Chen, Y. P. Cui, *RSC Adv.* **2014**, *4*, 60936–60942.
- [36] M. A. Van Dijk, A. L. Tchebotareva, M. Orrit, M. Lippitz, S. Berciaud, D. Lasne, L. Cognet, B. Lounis, *Phys. Chem. Chem. Phys.* **2006**, *8*, 3486–3495.

# Chapter 4

## A Strategy for Preparing SERS-SICM Probes

4.1 Preparation and Characterization of SERS-SICM Probes .....	101
4.1.1 Single-barrel borosilicate nanopipettes coated with gold nanorods .....	101
4.1.2 Single-barrel borosilicate nanopipettes coated with gold nanostructures of varying sizes and morphologies.....	105
4.1.3 Double-barrel quartz nanopipettes coated with gold nanostructures of varying morphologies. ....	110
4.2 SERS Performance of the SERS-SICM Probes.....	112
4.3 Evaluating the Clean Aperture of the Probe and the Anchoring Stability of Gold Nanostructures with SICM Technique .....	116
4.4 Summary .....	120
References.....	120

SERS is a vibrational spectroscopy technique with many particular advantages, such as label-free, ultrahigh surface sensitivity, fingerprint, non-destructive, multiplex detection, etc.<sup>[1]</sup> Such many unique advantages make the SERS technique a suitable tool for challenging analytical applications, especially relevant for investigating complicated biological systems. The applications of SERS in bioanalytical fields can be exemplified by applying plasmonic nanostructures into cells for the analysis of intracellular content. The general method is to disperse plasmonic nanostructures in the culture medium and most cells can uptake the nanostructures through endocytosis.<sup>[2]</sup> Although this method has been successfully used in optical imaging and spectroscopy, some uncontrollable issues still exist. One problem is the stability of the nanoparticles as the plasmonic nanostructures are prone to aggregation when they are exposed to complex culturing media and the endosomal environment.<sup>[3]</sup> The second issue is the interference signals from the special functionalization.<sup>[4]</sup> Another challenge is to effectively deliver plasmonic nanostructures to the specific compartments in cells.<sup>[5]</sup> Moreover, the toxic problems caused by the bio-persistence of plasmonic nanostructures and their resistance to biodegradation are vital problems that must be solved.<sup>[6]</sup> In order to address the above-described problems, anchoring the plasmonic nanostructures onto a substrate is an effective way.

On the other hand, SICM is a widely used imaging and analytical tool in biological areas, especially with the possibility to study subcellular structures of living cells in physiological conditions.<sup>[7]</sup> As described in Chapter 2, the key component of SICM is a glass nanopipette that serves as a scanning probe. Notably, most of the versatility of the SICM derives from the glass nanopipette, with a macro-sized long tail and a nanosized tapered end, that can be easily fabricated, manipulated, and modified.<sup>[8-10]</sup> Interestingly, the probe can be connected to microinjection systems or electrophysiological setups allowing an on-demand injection and aspiration, thus making it possible to do intracellular measurements and manipulations with high sensitivity and high spatial resolution.<sup>[8, 11]</sup>

The combination of SERS and SICM seems feasible by converting nanopipettes to SERS substrates by decorating plasmonic nanostructures on the outer surface of glass nanopipettes. The resulting nanopipettes covered with plasmonic nanostructures, termed SERS-SICM probes, can have the potential to solve above-mentioned problems during intracellular measurements. In 2009, the first success in decorating the outer surface of the glass nanopipette with plasmonic nanostructures for

intracellular analysis was reported.<sup>[12]</sup> In this case, the glass nanopipettes were firstly modified with molecules which have positively charged terminal NH<sub>2</sub> groups and then decorated plasmonic nanostructures with negative charge on the surface of the modified glass nanopipettes by electrostatic interaction. Until now, several other research works also reported the success of obtaining this kind of plasmonic nanopipettes using the similar method.<sup>[13-15]</sup> However, the nanopipettes pore apertures were blocked to some extent by the plasmonic nanostructures, limiting the further use of the probes to investigate intracellular measurement. Moreover, keeping the apertures open endows the SERS-SICM probes with the potential of concurrently injecting medicines and monitoring the responses of cells. Consequently, it is still a challenging task to prepare SERS-SICM probes with nanostructures of varying sizes and morphologies while ensuring the probe aperture open.

In this study, I demonstrated a strategy to make SERS-SICM probes and provided their top view SEM images to unambiguously show the empty apertures. Specifically, the glass nanopipette was firstly modified with (3-mercaptopropyl) trimethoxysilane (MPMS) molecules which have two functional groups, one is the silanol group that can link with the surface of nanopipette through silanization<sup>[16]</sup> and the other one is thiol group which can form Au-S bond with gold nanostructures.<sup>[17]</sup> The glass nanopipette modified with MPMS was subsequently immersed into a gold nanostructure colloid to further decorate the outer wall. It must be pointed out that a controlled airflow through the pipette and the immersion time of the nanopipette are very important for successfully preparing SERS-SICM probes with the tips open. This method has been assessed by decorating gold nanorods, gold nanospheres, gold trisoctahedrons and gold nanobipyramids on single-barrel borosilicate nanopipettes and double-barrel quartz nanopipettes. Moreover, I also proved the SERS performance of nanopipettes decorated with gold nanorods. Finally, the probes were employed to do SICM imaging or penetrate living cells to further confirm that the inside of the probes is empty. The anchoring stability of nanostructures on the outer surface of glass nanopipette was confirmed by comparing the SEM images of the SERS-SICM probes before and after applications.

## 4.1 Preparation and Characterization of SERS-SICM Probes

In this section, I will present the method for coating the outer surface of nanopipettes with gold nanostructures of varying sizes and morphologies and the key factors for successfully obtaining the SERS-SICM probes with empty tips. I will describe single-barrel borosilicate nanopipettes coated with gold nanorods in Section 4.1.1, single-barrel borosilicate nanopipettes coated with gold nanostructures of varying sizes and morphologies in Section 4.1.2, and double-barrel quartz nanopipettes coated with gold nanostructures of varying morphologies in Section 4.1.3.

### 4.1.1 Single-barrel borosilicate nanopipettes coated with gold nanorods

In my study, borosilicate capillaries (single-barrel) were firstly chosen to fabricate nanopipettes, using a laser-puller with a two-step process (see Chapter 2 for details). Before pulling, the capillaries were firstly processed by the freshly prepared Piranha solution ( $\text{H}_2\text{SO}_4 : \text{H}_2\text{O}_2 = 3 : 1$ ) for 2 h at room temperature, then thoroughly washed with deionized water and 2-propanol, and finally dried in an oven at 80 °C. This piranha solution pre-treatment promotes the presence of hydroxyl groups on the nanopipette surface which are essential for the modification of MPMS molecules on the surface through silanization. In Figure 4.1, a schematic describes the steps to prepare a glass nanopipette decorated with gold nanorods. Specifically, the glass nanopipette which has a hydroxyl-terminated surface was immersed into MPMS ethanol solution (1%, v/v) for 20 min while blowing the pipette with airflow (~6 bars). After washing the pipette with ethanol and drying at room temperature, the pipette was soaked into colloid gold nanorod solution with airflow (~6 bars) blowing the pipette at the same time as well. Both steps were performed at room temperature. The resulting product is a glass nanopipette decorated with a homogeneous layer of gold nanorods on its outer surface.

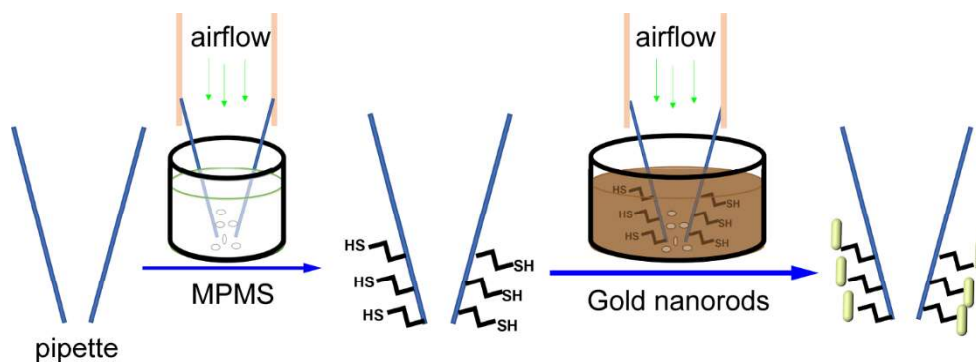


**Figure 4.1** The schematic exhibiting the detailed steps for coating gold nanostructures on the outer surface of a glass nanopipette.

Gold nanorods were firstly chosen as the plasmonic elements in the designing structure because gold nanorods have a relatively large flat surface that can be used to connect with nanopipette. The method for synthesizing gold nanorods was described in Chapter 2. Figure 4.2a and b display the extinction spectrum and SEM image of a typical gold nanorod sample, in this case, presenting the longitudinal plasmonic peak at 788 nm as well as the length and diameter measured from TEM images being  $76 \pm 6$  nm and  $24 \pm 3$  nm, respectively (a typical TEM image is shown in the insert image in Figure 4.2b). Prior to using gold nanorod colloid for decorating the glass nanopipette, the gold nanorods were washed with deionized water twice and diluted to deionized water for reaching an extinction intensity of around 0.5. After immersing the nanopipette into the above colloid for 10 min, the nanopipette was taken out and kept being blown for 2 min to dry it. The obtained nanopipette was firstly characterized by optical microscopy, which can illustrate the cleanliness and integrity of the pipette (Figure 4.2c). SEM imaging was then carried out to show the pipette decorated with gold nanorods (Figure 4.2d–g). Importantly, the low magnification SEM image shows the nanopipette is uniformly coated by gold nanorods (Figure 4.2d), and the higher magnification SEM images acquired corresponding to the frame areas in Figure 4.2d clearly show the morphology and distribution of gold nanorods on the surface of the nanopipette (Figure 4.2e–g). In addition, the top view SEM image of the nanopipette unambiguously shows that the tip of the nanopipette is coated until the very end of the pipette length while leaving the aperture fully exposed and clean (Figure 4.2h), which is very important for the application of the SERS-SICM probes.

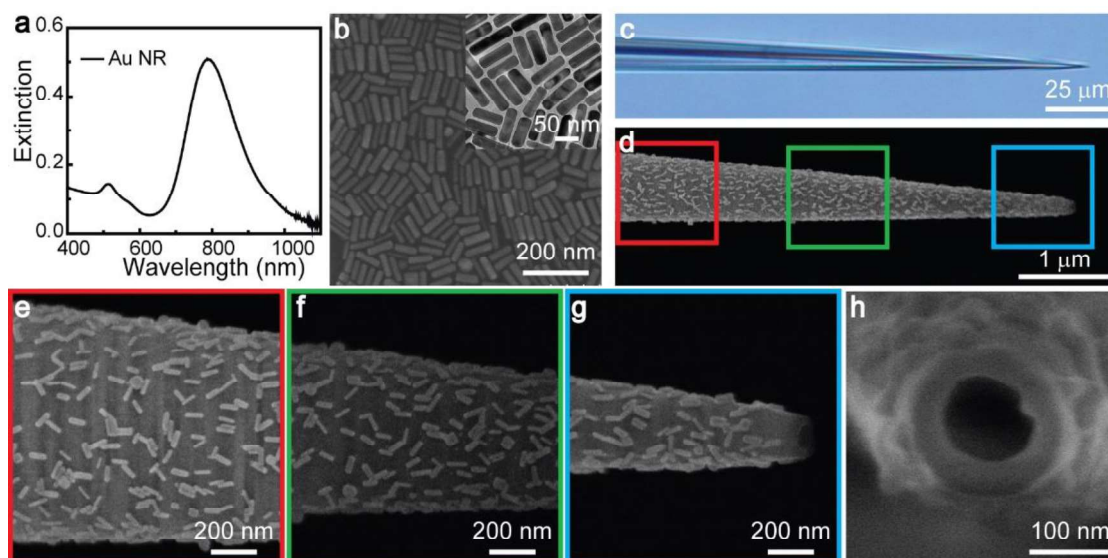


**Figure 4.2** The representation of SERS-SICM probe. (a–b) The extinction spectrum and SEM image of gold nanorods, the top-right insert in b is the corresponding TEM image of gold nanorods. (c–d) The optical micrograph and low magnification SEM image of nanopipette decorated with gold nanorods from side view. (e–g) Magnified SEM images of nanopipette covered by gold nanorods. The SEM images correspond to the areas marked by colored square lines in d. (h) SEM image of plasmonic nanopipette from top view.

The airflow plays an important role in the process of fabricating homogeneously coated nanopipettes with open apertures. If there is no airflow passing through the pipette in the step of silanization, the MPMS molecules were prone to polymerize at the end of the pipette and blocked the pipette, as shown in Figure 4.3a and b. On the second stage of the pipette modification, during the process of decorating the outer surface of nanopipette with gold nanostructures, the airflow is also essential to avoid the gold nanoparticles entering the nanopipette and causing the blockage of the pipette, as seen in Figure 4.3c and d that is the case without the use of airflow. Having a clean and defined aperture on nanopipettes is fundamental in the SICM technique because the mechanism of SICM (mentioned in Chapter 2) is using the current between two QRCEs to control the position of the pipette. In addition, keeping the tip aperture clean opens up the use of such SERS-SICM probes to concurrently deliver drugs into cells and monitor the responses of cells.

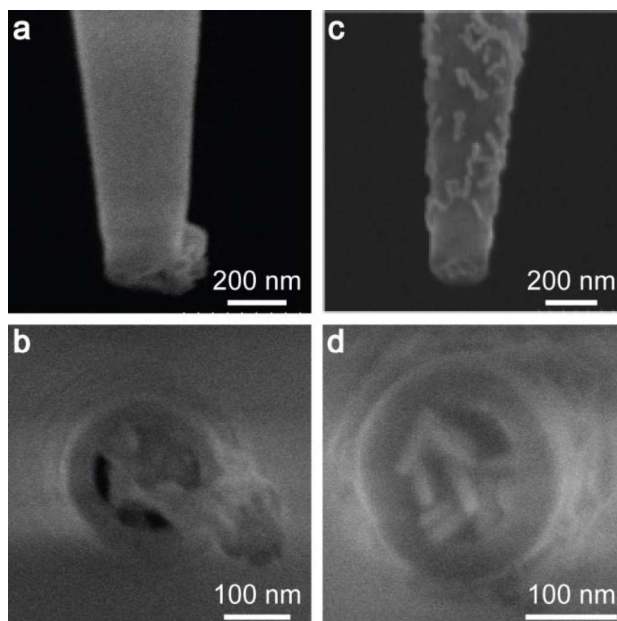


**Figure 4.3** The probes obtained without airflow. (a–b) SEM images of nanopipette after modified MPMS molecules on the surface, without airflow during the modifying process. (c–d) SEM images of nanopipette decorated with gold nanorods, without airflow during the decorating process.

Controlling the density and homogeneity of the nanoparticle coating is fundamental for SERS applications. I observed that the immersing time of nanopipette in the colloid gold solution can be used to control the density of particles. When the immersing time is too short, there are only a few nanoparticles on the nanopipette. Figure 4.4a and b are the SEM images of the nanopipette modified through an immersion time of 2 min, resulting in a nanopipette decorated with only a few nanorods on its surface and the end of the pipette clean. In contrast, when the immersion time was prolonged to 30 min, there are an excess of gold nanorods on the surface and the distribution of gold nanorods is not uniform (Figure 4.4c). Furthermore, the top view SEM image of the nanopipette, shown in Figure 4.4d, proves the presence of some gold nanorods blocking the pore of the nanopipette, despite airflow was still used during this experiment. This emphasizes the importance of controlling the immersion time for obtaining SERS-SICM probes successfully. In addition, varying the concentration of colloid gold nanoparticle solution can also change the densities of gold nanoparticles on the pipette surface. The effect of colloid concentration is similar to that of immersing time: for the same immersing time, the

particle density on the nanopipette surface is low when the colloid concentration is low, and the density will increase with increasing the colloid concentration.

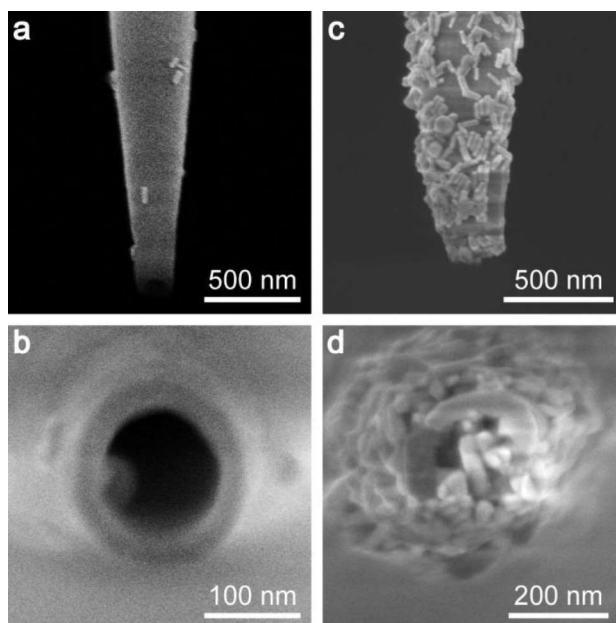


**Figure 4.4** The SERS-SICM probes obtained at different immersing time. (a–b) SEM images of the nanopipette decorated with gold nanorods with immersing time of 2 min. (c–d) SEM images of the nanopipette coated with gold nanorods with coating time of 30 min.

#### 4.1.2 Single-barrel borosilicate nanopipettes coated with gold nanostructures of varying sizes and morphologies.

The ability to create SERS-SICM probes with nanorods of varying sizes was assessed as LSPR performance is significantly dependent on the sizes of the gold nanostructures. Therefore, four gold nanorod samples with different sizes were synthesized. Figure 4.5a shows the extinction spectra of the four gold nanorod samples, with the wavelengths of the longitudinal plasmonic peaks being at 707 nm (Au NR 1), 751 nm (Au NR 2), 801 nm (Au NR 3), and 838 nm (Au NR 4), respectively. SEM and TEM imaging were carried out to characterize the shapes and sizes of the samples. As shown in Figure 4.5 b–i, the lengths of the gold nanorods are  $97 \pm 8$  nm,  $82 \pm 7$  nm,  $71 \pm 6$  nm, and  $63 \pm 7$  nm, the corresponding diameters are  $41 \pm 4$  nm,  $29 \pm 3$  nm,  $20 \pm 2$  nm, and  $16 \pm 2$  nm, respectively (sizes are measured from TEM images).

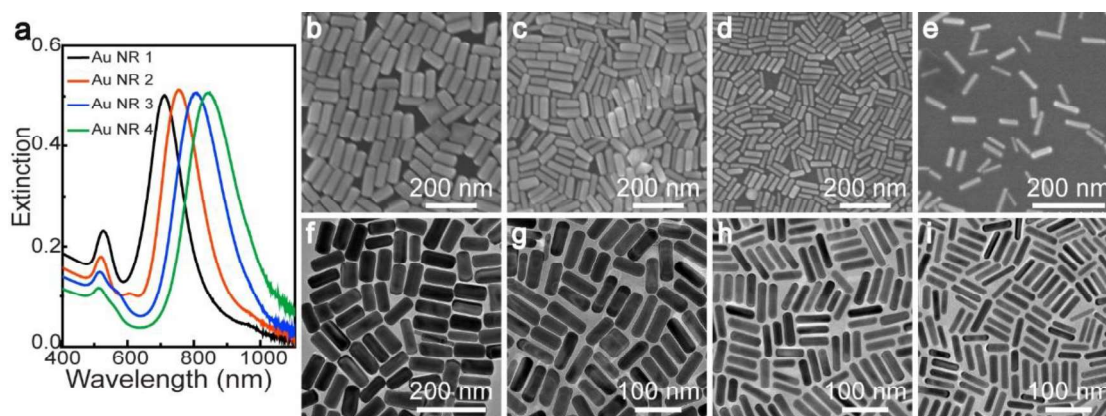


**Figure 4.5** Gold nanorod samples of varying sizes. (a) The extinction spectra of four gold nanorod samples. (b–e) SEM images of four gold nanorod samples, from left to right, they are Au NR 1, Au NR 2, Au NR 3, and Au NR 4, respectively. (f–i) TEM images of the corresponding gold nanorod samples.

Following the method shown in Figure 4.1, the above four gold nanorods were utilized to decorate the single-barrel borosilicate glass nanopipettes using the optimized preparation conditions (i.e. immersion time of 10 min). The SEM images of the resulted nanopipettes clearly prove the successful coverage of glass nanopipettes with gold nanorods (Figure 4.6a–d) while maintaining the apertures of the tip empty and clean after coating gold nanorods (Figure 4.6e–h). The uniformity of the coverage was evaluated for these probes as well, obtaining the corresponding SEM images of nanopipettes at the positions of about 5  $\mu\text{m}$  and 3  $\mu\text{m}$  away from the end of the nanopipettes (Figure 4.7). The SEM images unambiguously confirm these uniformities and illustrate the shape of nanorods, and the size of nanorods on different nanopipettes is different. Therefore, these experiments confirm the reproducibility of preparing the SERS-SICM probes and reinforce the suitability of the method to fix gold nanorods with various of sizes on the outer surface of borosilicate nanopipette with single barrel successfully.

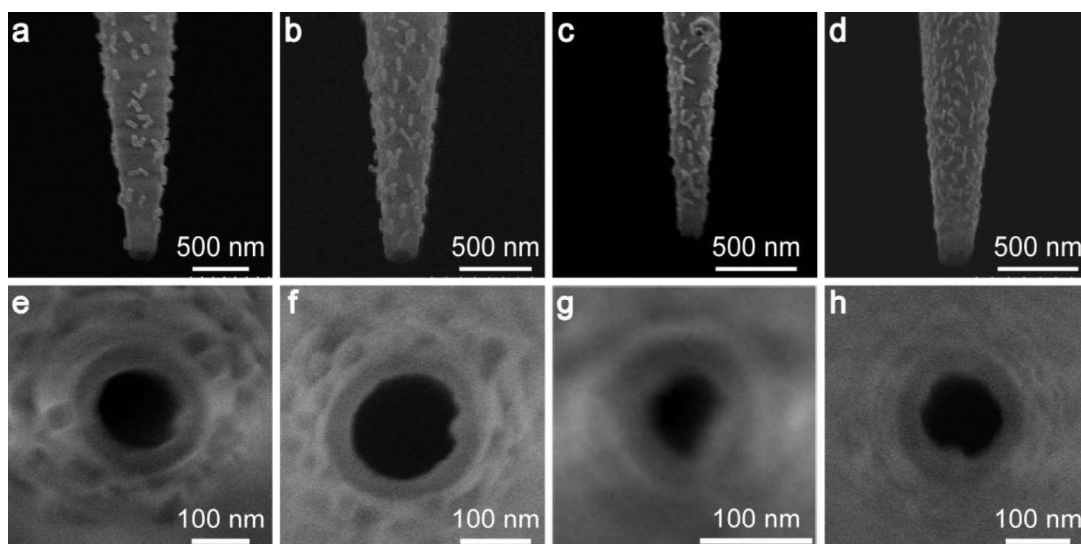


**Figure 4.6** SEM images of the SERS-SICM probes decorating with gold nanorods of varying sizes. (a–d) The side view SEM images of nanopipettes fixed with gold nanorods of varying sizes, from left to right, the pipette is decorated with Au NR 1, Au NR 2, Au NR 3, and Au NR 4, respectively. (e–h) The SEM images of the corresponding nanopipettes from top view.

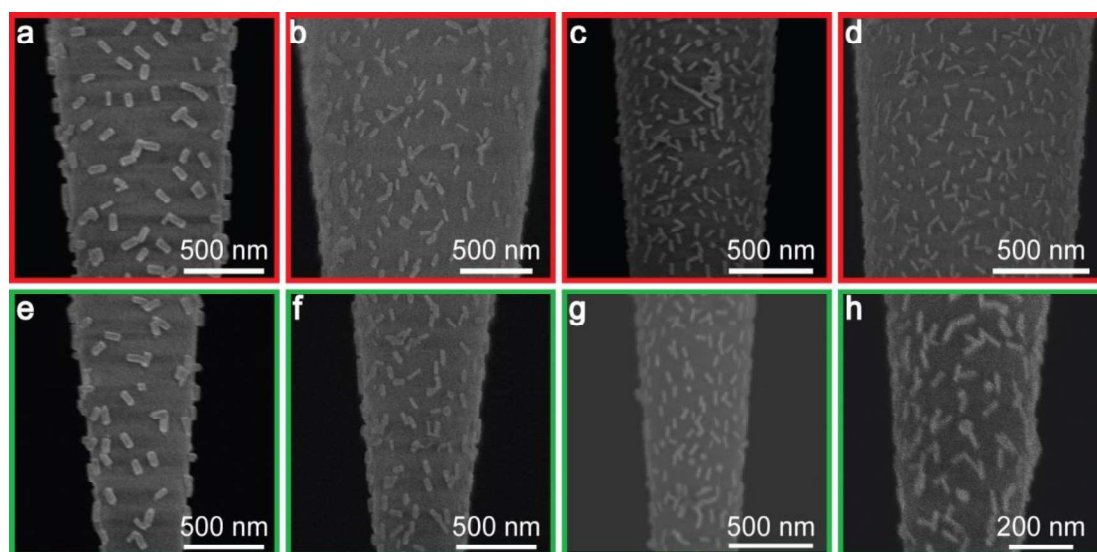


**Figure 4.7** The side view SEM images of nanopipettes decorated with gold nanorods of varying sizes about 5  $\mu\text{m}$  (a–d) and 3  $\mu\text{m}$  (e–h) away from the end of the corresponding nanopipettes. The SERS-SICM probes correspond to the nanopipettes in Figure 4.6.

In addition to gold nanorods with different sizes, the other morphologies of gold crystals were synthesized for decorating on the surface of borosilicate nanopipette as well since the shape of the nanostructure is also a key factor to largely influence the

LSPR properties. For example, gold trisoctahedrons with well-defined tips and edges exhibit much stronger local electromagnetic field in comparison with gold nanospheres, as illustrated in Chapter 3. According to the seed-mediated method mentioned in Chapter 2, gold nanospheres, gold trisoctahedrons and gold nanobipyramids were synthesized. The extinction spectra of these gold nanostructures are presented in Figure 4.8a, the dipolar peaks of gold nanospheres and trisoctahedrons are located at 536 nm and 576 nm, respectively, and the dipolar longitudinal peak wavelength of gold nanobipyramids is 819 nm. The extinction intensities were also tuned to around 0.5 by diluting the gold colloids with deionized water after washed. Their morphologies and sizes were characterized by SEM and TEM imaging (Figure 4.8b–g). Their sizes measured from TEM images are  $55 \pm 2$  nm,  $101 \pm 6$  nm, and  $101 \pm 4$  nm by  $35 \pm 2$  nm, respectively.

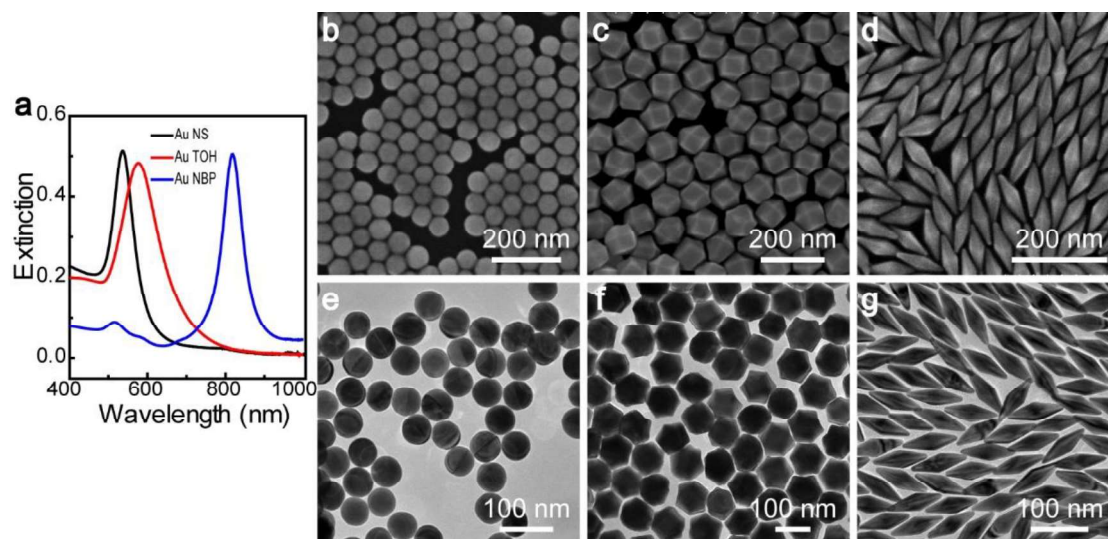


**Figure 4.8** The extinction spectra (a), SEM images (b–d), and TEM images (e–g) of gold nanospheres, gold trisoctahedrons, and gold nanobipyramids.

I used the above-described method to cover the outer surfaces of borosilicate nanopipettes with these three different types of nanostructures. The SEM imaging showed that all these three types of gold nanostructures can be anchored on the outer surface of the glass nanopipettes (Figure 4.9a–c) while ensuring the nanopipette apertures are not blocked by gold nanostructures or polymers formed from the polymerization of MPMS molecules (Figure 4.9d–f). Moreover, the SEM images of SERS-SICM probes at approximately 5  $\mu\text{m}$  and 3  $\mu\text{m}$  away from the end of the nanopipettes clearly show the shapes of gold nanospheres, trisoctahedrons and nanobipyramids as well as confirm the excellent homogeneous distributions of these

nanostructures (Figure 4.10). It must be noted that the time of immersing nanopipette into the gold colloids was different for different samples. Specifically, the immersing time was 30 min when the nanopipette was soaked into colloid gold nanosphere or gold trisoctahedron solution, and 20 min for placing the nanopipette into colloid gold nanobipyramid solution. The difference in the required immersing time is likely related to the existent difference in the interaction area between the nanostructure and the nanopipette surface. The nanorod possesses a relatively larger anchoring area, requiring lower time for ensuring to obtain a nanopipette with a good decoration. In addition, the density of gold trisoctahedrons on the outer surface of nanopipettes is much lower than other types of nanostructures, it is possibly because that gold trisoctahedron has much more well-defined edges and tips in comparison with other nanostructures and therefore it takes more time to fix trisoctahedrons on the nanopipette.

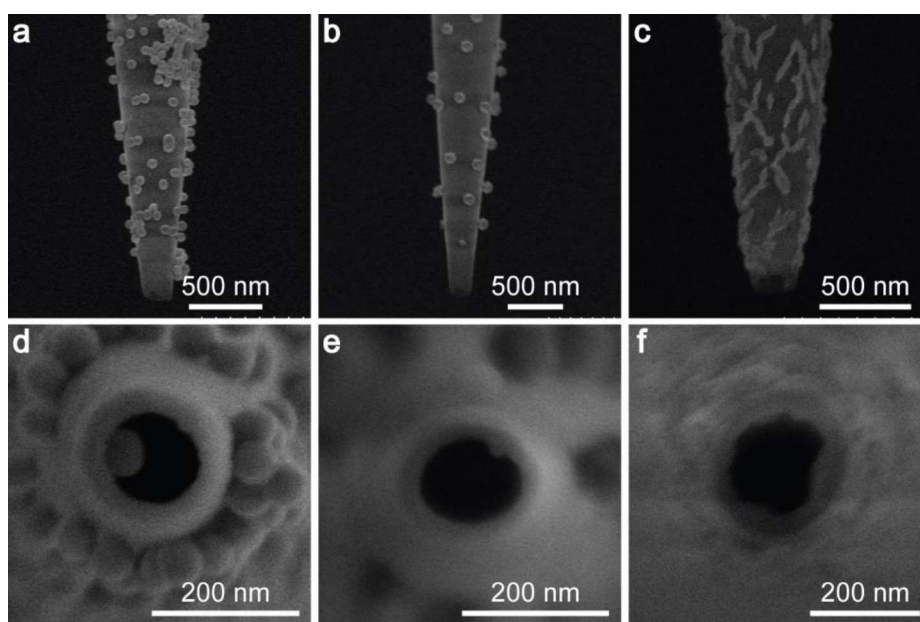


**Figure 4.9** SEM images of nanopipettes fixed with gold nanospheres, gold trisoctahedrons, and gold nanobipyramids, respectively, from side view (a–c) and top view (d–f).

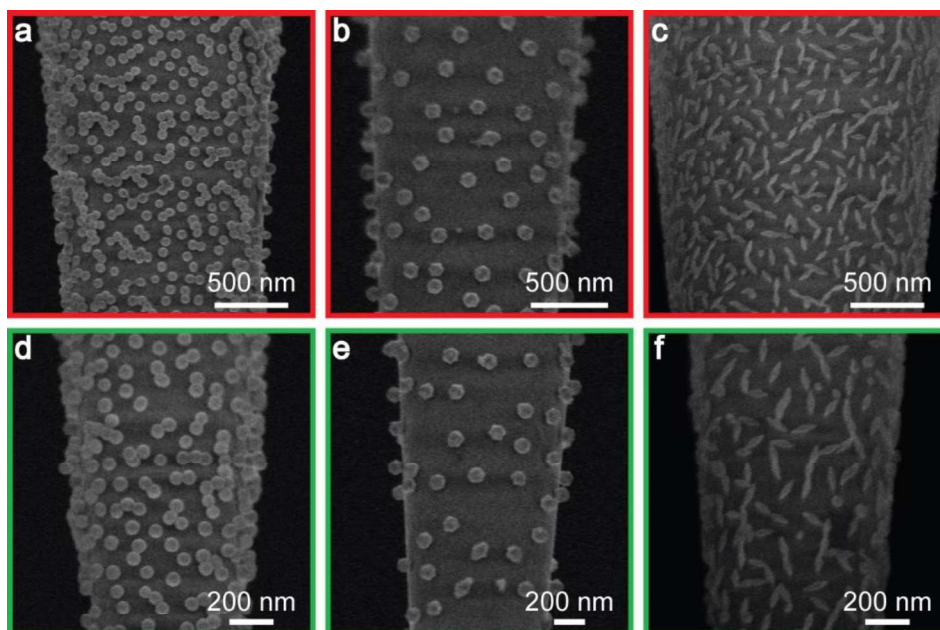


**Figure 4.10** SEM images of nanopipettes fixed with gold nanospheres, gold trisoctahedrons, and gold nanobipyramids, respectively, at the positions of about 5  $\mu\text{m}$  (a–c) and 3  $\mu\text{m}$  (d–f) away from the end of the nanopipettes. The SERS-SICM probes correspond to the nanopipettes in Figure 4.9.

#### 4.1.3 Double-barrel quartz nanopipettes coated with gold nanostructures of varying morphologies.

There are a broad variety of commercial capillaries that can be used to fabricate nanopipettes by laser-puller, ranging from single barrel to double barrels and even multiple barrels. The obtained double-barrel or multi-barrel nanopipettes can be applied in much more complex measurements.<sup>[7, 18]</sup> Moreover, the capillaries can be made of different materials, including borosilicate and quartz. Quartz capillaries are especially suitable for the fabrication of very small nanopipettes and quartz nanopipettes have the advantage of lower leakage currents.<sup>[10, 19]</sup> Therefore, I tried to anchor gold nanostructures onto the outer surface of quartz nanopipettes (double-barrel), obtained by pulling double-barrel quartz capillaries (the pulling parameters and SEM images of double-barrel quartz nanopipettes are presented in Chapter 2). Following the same process of decorating borosilicate nanopipettes, the double-barrel quartz capillaries were treated with freshly prepared Piranha solution before pulling, the obtained quartz nanopipettes were subsequently modified with MPMS solution, and finally covered by gold nanostructures of varying morphologies. The resulting nanopipettes were assessed via SEM imaging to determine the success in the coating,

the uniformity of the particle decoration along pipette length as well as the cleanliness of the apertures. As shown in Figure 4.11–4.12, the results are similar to the ones obtained for borosilicate glass capillaries, observing no significant differences. We conclude the use of MPMS molecules as linkers with the help of airflow is a robust method for preparing various of SERS-SICM probes.

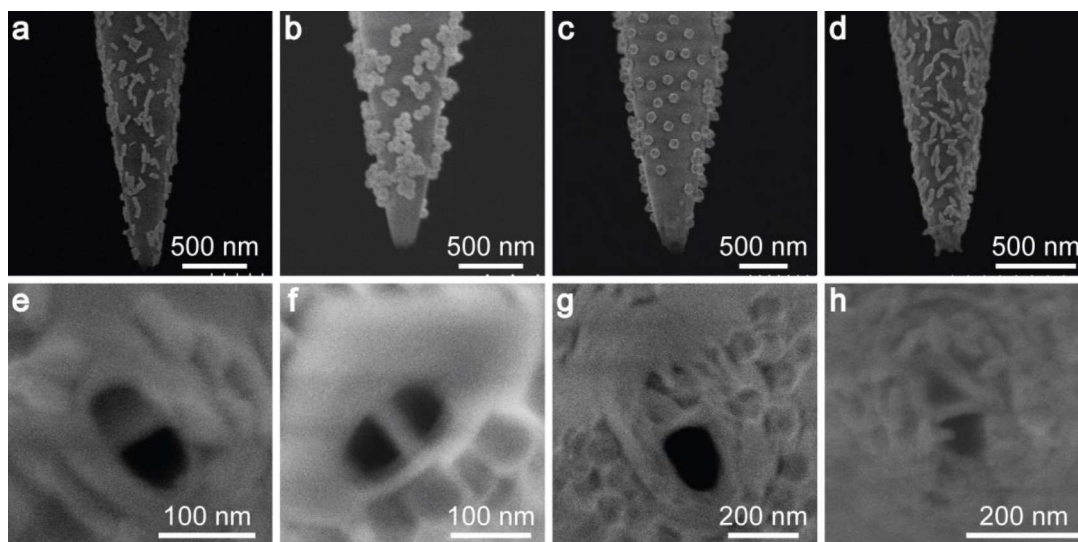


**Figure 4.11** SEM images of double-barrel quartz nanopipettes fixed with gold nanorods, gold nanospheres, gold trisoctahedrons, and gold nanobipyramids, respectively, from side view (a–d) and top view (e–h).

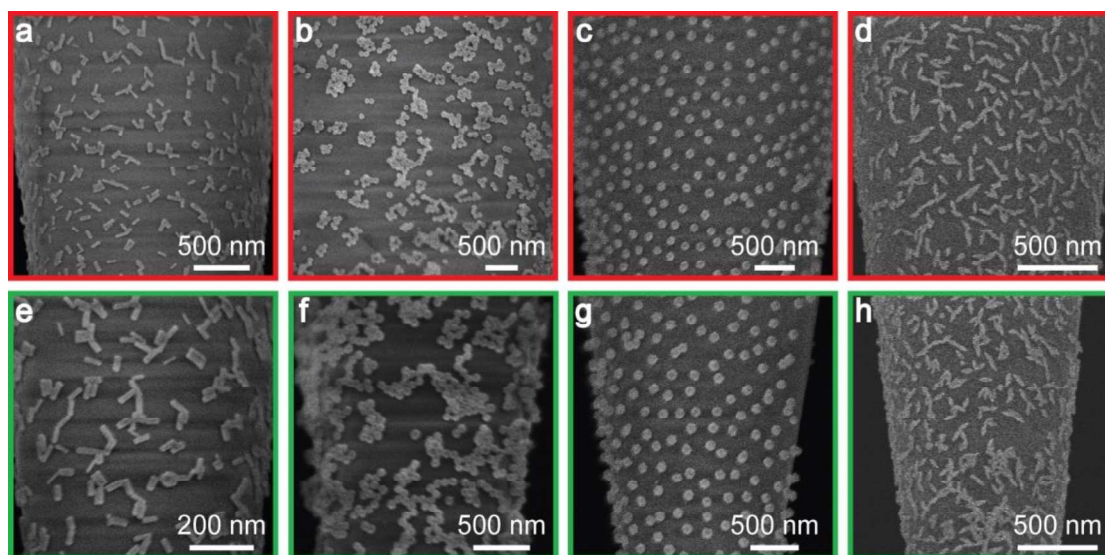


**Figure 4.12** SEM images of quartz nanopipettes fixed with gold nanorods, gold nanospheres, gold trisoctahedrons, and gold nanobipyramids, respectively, at the positions of about 5  $\mu\text{m}$  (a–d) and 3  $\mu\text{m}$  (e–h) away from the end of the nanopipettes. The SERS-SICM probes correspond to the nanopipettes in Figure 4.11.

## 4.2 SERS Performance of the SERS-SICM Probes

Glass nanopipettes decorated with gold nanostructures have the potential to largely enhance the Raman scattering signals, and the SERS performances of such SERS-SICM probes were measured and confirmed in my study. Several glass nanopipettes anchored with gold nanorods for Raman measurements were prepared (the employed nanorods are the ones presented in Figure 4.2), as shown in Figure 4.13. Among the SEM images, Figure 4.13a–c show the single-barrel borosilicate nanopipettes coated with gold nanorods and Figure 4.13d–f present the double-barrel quartz nanopipettes anchored with gold nanorods. The SERS performances were demonstrated by the detection of three commonly used Raman-active molecules, including R6G, 4-MBT, and 2-NaT. Thus, the above obtained SERS-SICM probes were immersed into different solutions of R6G in water ( $10^{-7}$  M), 4-MBT in ethanol ( $10^{-4}$  M), and 2-NaT in ethanol ( $10^{-4}$  M), respectively, for overnight. Followed by cleaning the nanopipettes immersed into 4-MBT and 2-NaT solutions with ethanol to remove the excess molecules. Their SERS properties were then measured after drying at room temperature.

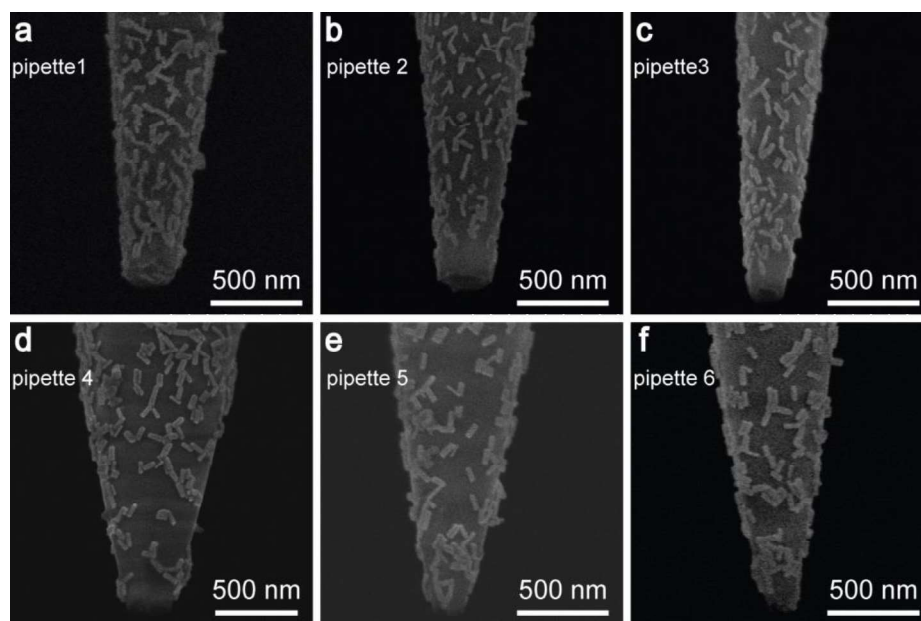


**Figure 4.13** SEM images of SERS-SICM probes for SERS measurements. (a–c) Single-barrel borosilicate nanopipettes decorated with gold nanorods. (d–f) Double-barrel quartz nanopipettes coated by gold nanorods.

The utilized Raman setup was the same as described in Chapter 3. A laser with the excitation wavelength of 633 nm was used at a power of 0.28 mW and the collection

time was 20 s. The laser was firstly focused on the tips of the plasmonic nanopipettes with a 100× objective lens (NA = 0.90), as shown in Figure 4.14.

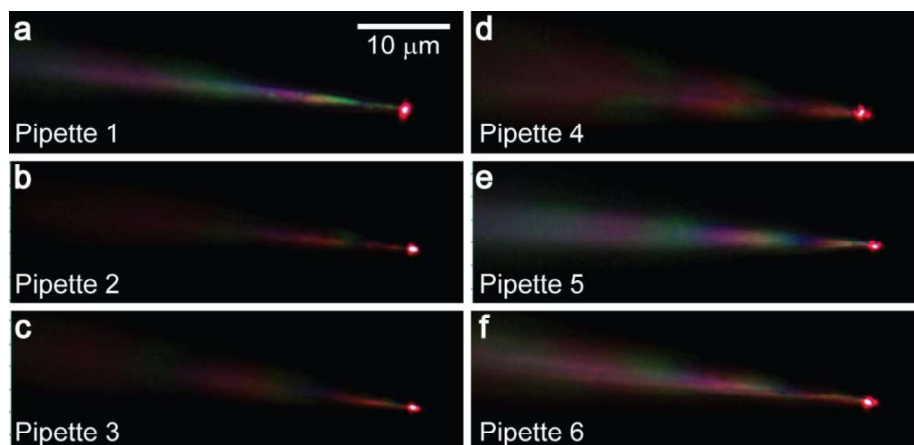


**Figure 4.14** The optical micrographs of SERS-SICM probes with 633 nm laser focusing on the tip.

The recorded Raman signals are shown in Figure 4.15, the characteristic signals of the corresponding molecules can be observed unambiguously. As for the Raman spectra of the SERS-SICM probes adsorbed with R6G molecules, the peak located at  $611\text{ cm}^{-1}$  is due to the in-plane bend of the xanthene ring, the signal positioned at  $770\text{ cm}^{-1}$  is assigned by the out-of-plane bending mode of the C-H band, the peak at  $1186\text{ cm}^{-1}$  is attributed to the stretching mode of the C-O-C band, the peak at  $1306\text{ cm}^{-1}$  is assigned to in-plane bending mode of the N-H band, and the peaks at  $1358\text{ cm}^{-1}$ ,  $1502\text{ cm}^{-1}$  and  $1637\text{ cm}^{-1}$  belong to the stretching modes of aromatic benzene rings.<sup>[20–22]</sup> With regard to the Raman spectra of the SERS-SICM probes bonded with 4-MBT molecules, the strong Raman signal at  $1069\text{ cm}^{-1}$  can be assigned to a combination of the breathing mode of phenyl ring, the stretching mode of C-S, and the in-plane bending mode of C-H, the signals at  $1174\text{ cm}^{-1}$  and  $1376\text{ cm}^{-1}$  are contributed by the in-plane vibrations of phenyl ring, while the stretching mode of phenyl ring is located at  $1575\text{ cm}^{-1}$ .<sup>[23–24]</sup> The assignment of the strong Raman signals, located at  $761\text{ cm}^{-1}$ ,  $1061\text{ cm}^{-1}$ ,  $1372\text{ cm}^{-1}$  and  $1613\text{ cm}^{-1}$ , in the spectra of the SERS-SICM probes adsorbed with 2-NaT molecules has been discussed in Chapter 3. The assignment of the Raman signals for the three types of Raman-active molecules are summarized in Table 4.1. The observed differences in the intensities of Raman signals among these samples are probably attributed to the following factors: (a) the inherent difference in the Raman cross-sections of different molecules; (b) the difference in the measured surface areas due to the different sizes of the nanopipettes; (c) the slight difference in

the densities of the nanorods on the outer surface of the nanopipettes; as well as (d) the difference in excited gap modes.

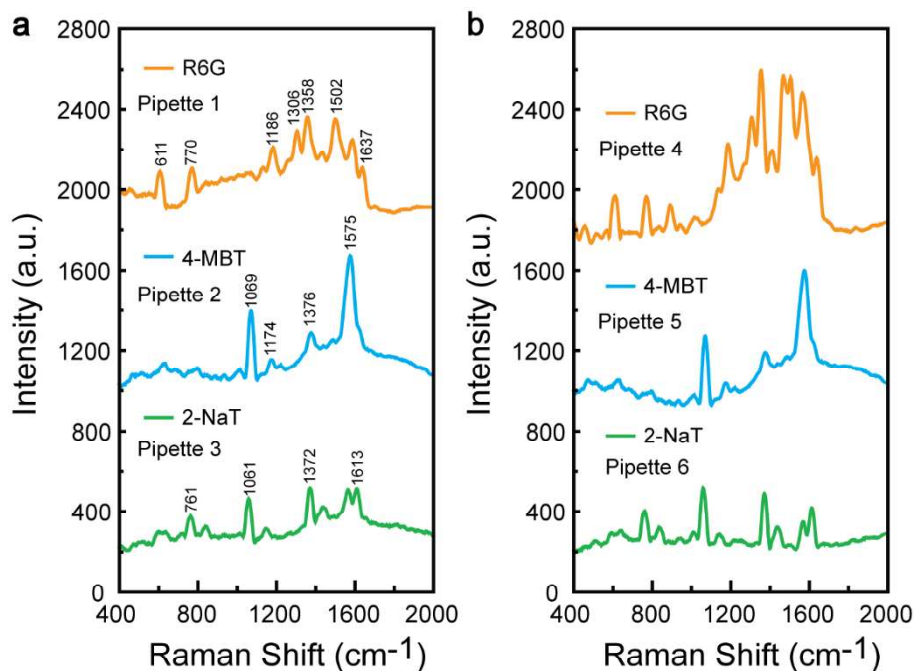


**Figure 4.15** The Raman spectra of the SERS-SICM probes adsorbed with detection molecules measured from the tips.

**Table 4.1** The assignment of the Raman signals for the detected three types of Raman-active molecules (R6G, 4-MBT, and 2-NaT).

Molecule	Raman Peak (cm <sup>-1</sup> )	Mode
Rhodamine 6G (R6G)	611	In-plane bend of the xanthene ring
	770	Out-of-plane bend of the C-H band
	1186	Stretching mode of the C-O-C band
	1306	In-plane bend of the N-H band
	1358	Stretching mode of aromatic benzene rings
	1502	
1637		
4-methylbenzenethiol (4-MBT)	1069	A combination of the breathing mode of phenyl ring, the stretching mode of C-S, and the in-plane bending mode of C-H
	1174 1376	In-plane vibrations of the phenyl ring
	1575	Stretching mode of the phenyl ring
2-naphthalenethiol (2-NaT)	761	The ring deformation
	1061	The C-H bending
	1372 1613	Stretching mode of the ring

Additionally, the Raman responses of the SERS-SICM probes adsorbed with detection molecules at the position of around  $5\ \mu\text{m}$  away from the tip were measured. As expected, the peaks in the Raman spectra have the same positions as those measured from the tips but show much higher intensities (Figure 4.16). The higher intensities arise from the fact that more molecules are detected since the surface areas are larger at the positions of around  $5\ \mu\text{m}$  away from the tips.

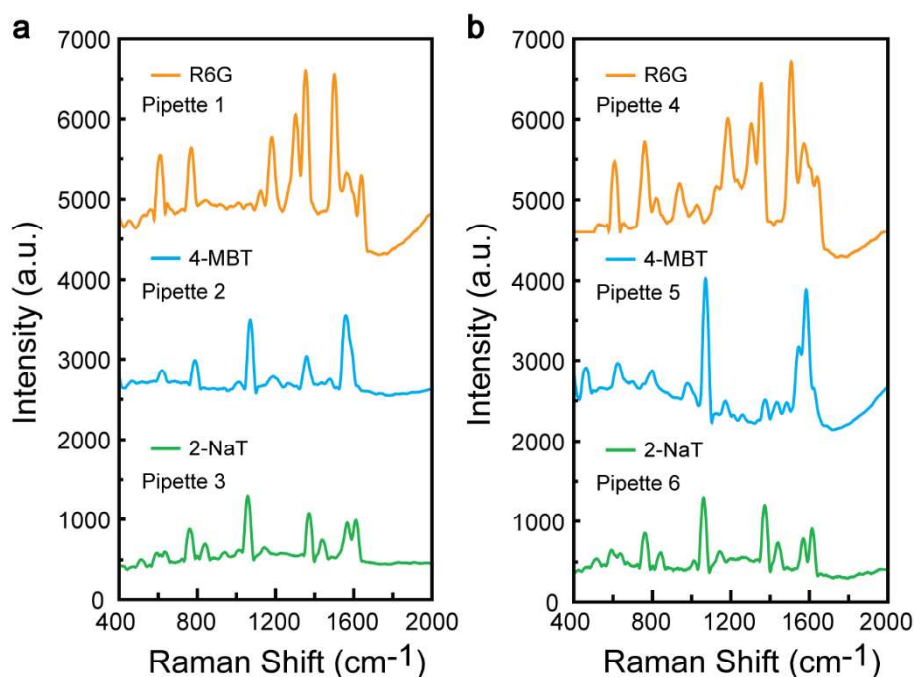


**Figure 4.16** The Raman spectra of the SERS-SICM probes adsorbed with detection molecules measured from the positions of around  $5\ \mu\text{m}$  away from the tips.

Moreover, the Raman signals of bare nanopipettes covered by the above three types of Raman-active molecules were measured as well. The nanopipettes without any decoration, including borosilicate and quartz ones, were immersed into 0.01M R6G, 0.01 M 4-MBT, and 0.01 M 2-NaT for 2 h, respectively, and then these nanopipettes were dried at room temperature. During the collecting of Raman responses, no Raman peak was observed even with high laser power (3 mW). Figure 4.17 shows the typical Raman spectra that collected on the bare nanopipettes. These results clearly illustrate that the gold nanostructures on the nanopipette can highly enhance the Raman signals.

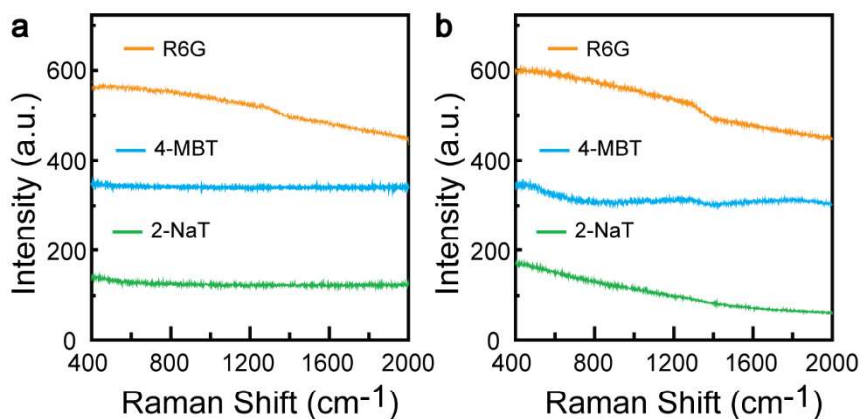


**Figure 4.17** The Raman spectra of the bare borosilicate nanopipettes (a) and quartz nanopipettes (b) coated with Raman-active molecules.

### 4.3 Evaluating the Clean Aperture of the Probe and the Anchoring Stability of Gold Nanostructures with SICM Technique

As mentioned above, keeping the apertures open is essential for the potential applications of these obtained SERS-SICM probes. A suitable approach to confirm the empty inside of the nanopipette is applying it in the SICM technique. There will not be a current between the two QRCEs if the pipette is blocked, however, the current is the base for using SICM technique. Thus, the probe cannot use to the SICM technique if its inside is blocked. Moreover, the robustness of the anchored plasmonic nanostructures on the outer surface of glass nanopipette is also important. The possibility that the plasmonic nanostructures do not remain attached to the nanopipette during application can be a major disadvantage that must be assessed. Therefore, it is important to challenge the blockage of the probe and the strength of adhesion, especially during the AC modulation of SICM imaging or when the nanopipette penetrates the living cells towards inner cell analysis.

The SERS-SICM probe prepared as in Section 4.1.1 was employed in SICM imaging of Madin-Darby Canine Kidney (MDCK) living cells. Specifically, a single-barrel borosilicate nanopipette covered with gold nanorods was used as imaging probe (Figure 4.18a–c). The pipette and the MDCK cells were immersed in a Dulbecco's modified eagle medium (DMEM) solution (0.15 M) enriched with N-2-hydroxyethylpiperazine-N'-2-ethane sulfonic acid (HEPES, 0.02 M), and fitted with two Ag/AgCl wires acting as QRCEs, one was inside the pipette and the other was in

the bath solution. A 0.1 V bias was applied between these two Ag/AgCl wires to drive an ionic current that was used to track tip-sample distance.

SICM imaging of living cells was carried out employing the so-called hopping mode<sup>[25]</sup> in which the topographic information of the surface is obtained by carrying out an array of individual probe approaches to form a topographic map of the surface. During the process of imaging, the approaching rate, the retracting rate, and the lateral scanning rate were 30  $\mu\text{m/s}$ , 40  $\mu\text{m/s}$  and 35  $\mu\text{m/s}$ , respectively. A 50  $\mu\text{m} \times 70 \mu\text{m}$  topographic image of the MDCK living cell with a 1  $\mu\text{m}$  lateral hopping distance was obtained. Figure 4.18d clearly shows the morphology of the MDCK living cell, which is comparable to the optical micrograph (the insert image in Figure 4.18d). The success of obtaining SICM topographic image confirms that the inside of the probe is not blocked. After obtaining the SICM image, the probe was cleaned with deionized water and dried at room temperature for SEM imaging and the SEM images were presented in Figure 4.18e–g. The comparison of the SEM images before and after SICM imaging illustrates that most of the particles are robustly fixed on the pipette. Only a few at the end of the tip were lost, which is probably because the applied voltage during the imaging process may drive the particles with weak adhesion to move.<sup>[26]</sup>

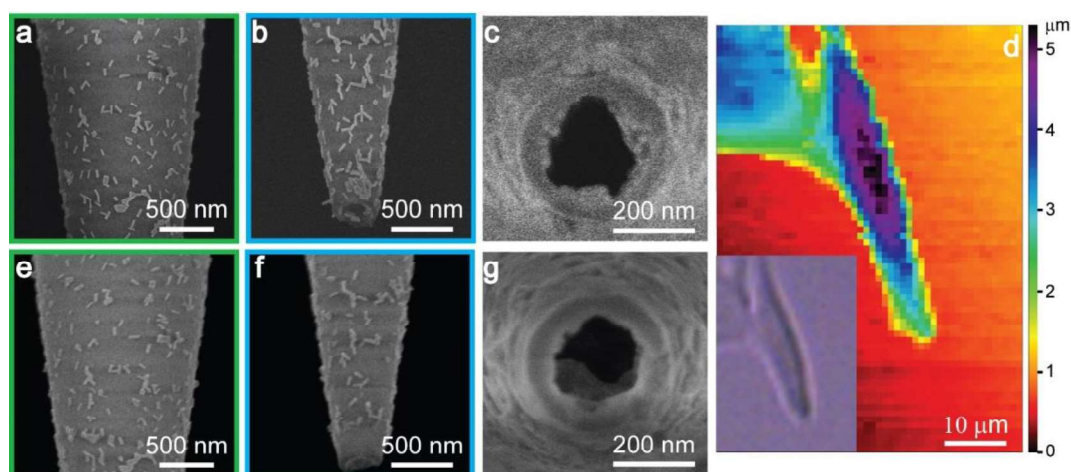


**Figure 4.18** SEM images of the SERS-SICM probe before and after doing SICM imaging, and the SICM map of a living cell. (a–c) SEM images of SERS-SICM probe for SICM imaging. (d) SICM topographic image of the MDCK living cell, the left bottom insert is the corresponding optical micrograph. Miss Martina Papa kindly helped me do the SICM imaging of living cells. (e–g) SEM images of SERS-SICM probe after SICM imaging.

Moreover, the anchoring stability was also measured by inserting the SERS-SICM probe into a MDCK living cell. A schematic diagram of the probe approaching and penetrating a cell is shown in Figure 4.19a. In this case, the current changes, including DC change and AC variation, were recorded during the process of the approach and penetration (Figure 4.19b and c). As expected for a regular SICM approach curve, the DC experienced a decay when the distance between the tip and the cell membrane became comparable with the pipette size (region I). Once the probe is in the vicinity of the cell membrane, the further approach resulted in a different trend in the DC approach curve (region II). A slight increase in the DC curve was seen because the probe penetrated the membrane of the cell and thus the resistance between the two QRCEs decreased abruptly.<sup>[27–28]</sup> After the nanopipette inserted into cell, the slow decrease of the current (region III) is probably because the cell membrane slightly sealed around the orifice and the complicated intracellular environment.<sup>[27]</sup> When the probe continued to approach, a dramatic decrease in the current can be seen (region IV), which is due to the distance between the probe and the bottom membrane decreasing to comparable with the size of the probe. This penetration process was also followed with the AC current, that was used as a feedback parameter to stop the approach and withdraw the probe (Figure 4.19c).

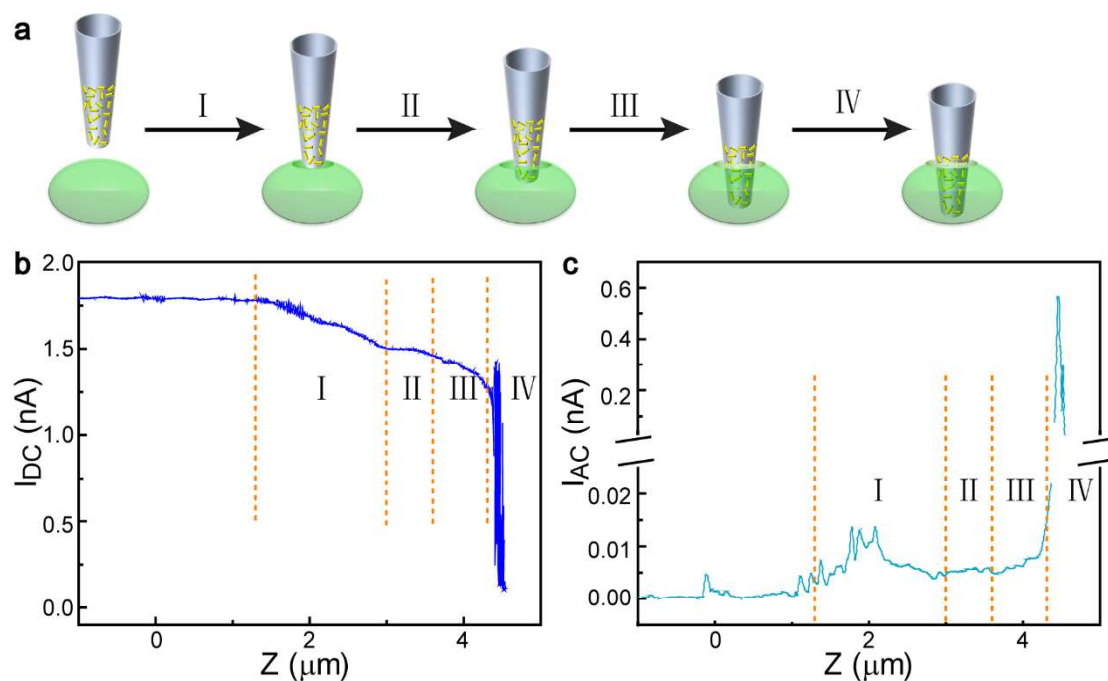


**Figure 4.19** The living cell penetration with a SERS-SICM probe. (a) A schematic diagram of the process of the SERS-SICM probe approaching and penetrating a cell. (b) The change of the DC curve during the process of the SERS-SICM probe

*approaching and penetrating a cell. (c) The corresponding AC variation. Miss Martina Papa kindly helped me do the experiment of penetrating living cells.*

To assess the mechanical stability of the anchored nanoparticles, the probe was removed from the SICM microscope, immersed in deionized water overnight, and finally left in air for drying. Subsequently, the nanopipette was imaged with SEM to confirm the particles still remained at the nanopipette. By comparing the SEM images of the nanopipettes before (Figure 4.20a and b) and after (Figure 4.20c and d) the probe penetration experiment, it is unambiguous that the gold nanorods are still on the outer surface of the nanopipette. The red arrows in Figure 4.20b and d clearly indicate that the gold nanorods stably maintain at the original positions. Therefore, the plasmonic nanostructures can be stably fixed on the glass nanopipettes with the method introduced in this Chapter. I believe that this robust method for covering plasmonic nanostructures on the outer surface of the glass nanopipettes is meaningful for the application research of the plasmonic nanostructures.

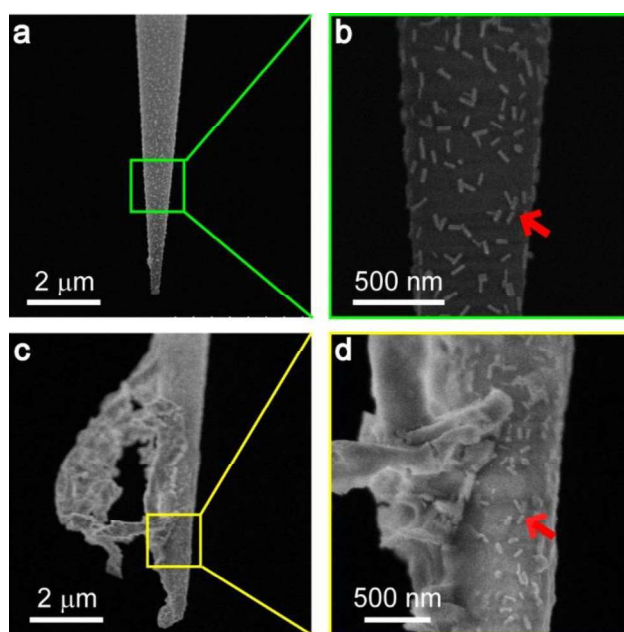


**Figure 4.20** SEM images of the SERS-SICM probe before and after inserting into a cell. (a–b) SEM images of the SERS-SICM probe before inserting into a cell. b corresponds to the area marked with green square lines in a. (c–d) SEM images of the corresponding SERS-SICM probe after penetration. d corresponds to the area marked with yellow square lines in c.

## 4.4 Summary

In this work, I have developed a facile and robust strategy for producing SERS-SICM probes by coating the outer surface of glass nanopipettes with a homogeneous and robust layer of gold nanostructures while maintaining the tip apertures open. The suitability of this method was evaluated by employing four types of gold nanostructures, including gold nanorods with different sizes, gold nanospheres, gold trisoctahedrons, and gold nanobipyramids. Moreover, to confirm the applicability of the method to a diverse variety of commercial capillaries, the method was tested using borosilicate capillaries (single-barrel) and quartz capillaries (double-barrel). Homogeneous gold nanostructure coatings were obtained by enhancing the chemical functionalities of the glass surfaces and controlling the deposition times. The SERS performances of the SERS-SICM probes were examined using three different molecules, including R6G, 4-MBT, and 2-NaT, obtaining strong Raman signals. Finally, the SERS-SICM probes were tested in real conditions, carrying out successfully AC-modulated hopping mode SICM imaging of living cells in physiological conditions. The coating proved to be highly robust not only to the SICM imaging conditions, but also to the insertion through a living cell membrane and the intracellular environment. Overall, in this chapter the results illustrate the fabrication and characterization of SERS-SICM probes and pave the way to extending the analytical capabilities of SICM topographic imaging to a complementary three-dimensional mapping of chemicals using SERS as analytical technique. Indeed, it has been reported that the plasmonic glass nanopipettes modified with Raman reporter molecules can be used to quantify the oxygen levels in hypoxic single cells and tumors,<sup>[14]</sup> cause and detect the variations of the intracellular temperature with laser illumination,<sup>[29]</sup> as well as analyze the pH change of the endosomal environment.<sup>[15]</sup>

## References

- [1] C. Zong, M. X. Xu, L. -J. Xu, T. Wei, X. Ma, X. -S. Zheng, R. Hu, B. Ren, *Chem. Rev.* **2018**, *118*, 4946–4980.
- [2] S. Behzadi, V. Serpooshan, W. Tao, M. A. Hamaly, M. Y. Alkawareek, E. C. Dreaden, D. Brown, A. M. Alkilany, O. C. Farokhzad, M. Mahmoudi, *Chem. Soc. Rev.* **2017**, *46*, 4218–4244.

- [3] S. J. Soenen, W. J. Parak, J. Rejman, B. Manshian, *Chem. Rev.* **2015**, *115*, 2109–2135.
- [4] V. A. Kickhoefer, M. Han, S. Raval-Fernandes, M. J. Poderycki, R. J. Moniz, D. Vaccari, M. Silvestry, P. L. Stewart, K. A. Kelly, L. H. Rome, *ACS Nano* **2009**, *3*, 27–36.
- [5] J. Mosquera, I. Garcia, L. M. Liz-Marzan, *Acc. Chem. Res.* **2018**, *51*, 2305–2313.
- [6] X. W. Ma, Y. Y. Wu, S. B. Jin, Y. Tian, X. N. Zhang, Y. L. Zhao, L. Yu, X. -J. Liang, *ACS Nano* **2011**, *5*, 8629–8639.
- [7] C. Zhu, K. X. Huang, N. P. Siepser, L. A. Baker, *Chem. Rev.* **2021**, *121*, 11726–11768.
- [8] H. -L. Liu, J. Cao, S. Hanif, C. Yuan, J. Pang, R. Levicky, X. -H. Xia, K. Wang, *Anal. Chem.* **2017**, *89*, 10407–10413.
- [9] A. Page, D. Perry, P. R. Unwin, *Proc. R. Soc. A* **2017**, *473*, 20160889.
- [10] T. Takami, B. H. Park, T. Kawai, *Nano Convergence* **2014**, *1*, 17.
- [11] S. -Y. Yu, Y. -F. Ruan, Y. -L. Liu, D. -M. Han, H. Zhou, W. -W. Zhao, D. C. Jiang, J. -J. Xu, H. -Y. Chen, *ACS Sens.* **2021**, *6*, 1529–1535.
- [12] E. A. Vitol, Z. Orynbayeva, M. J. Bouchard, J. Azizkhan-Clifford, G. Friedman, Y. Gogotsi. *ACS Nano* **2009**, *3*, 3529–3536.
- [13] J. -F. Masson, J. Breault-Turcot, R. Faïd, H. -P. Poirier-Richard, H. Yockell-Lelievre, F. Lussier, J. P. Spatz, *Anal. Chem.* **2014**, *86*, 8998–9005.
- [14] T. D. Nguyen, M. S. Song, N. H. Ly, S. Y. Lee, S. -W. Joo, *Angew. Chem. Int. Ed.* **2019**, *58*, 2710–2714.
- [15] J. Guo, A. S. Rubfiaro, Y. H. Lai, J. Moscoso, F. Chen, Y. Liu, X. W. Wang, J. He, *Analyst*, **2020**, *145*, 4852–4859.
- [16] R. E. Ozel, G. Bulbul, J. Perez, N. Pourmand, *ACS Sens.* **2018**, *3*, 1316–1321.
- [17] F. Tielens, E. Santos, *J. Phys. Chem. C* **2010**, *114*, 9444–9452.
- [18] Y. Shao, P. He, Z. Y. Yu, X. Liang, Y. H. Shao, *J. Electroanal. Chem.* **2022**, *908*, 116089.
- [19] C. A. Morris, A. K. Friedman, L. A. Baker, *Analyst* **2010**, *135*, 2190–2202.
- [20] S. A. Ghopry, M. Alamri, R. Goul, B. Cook, S. M. Sadeghi, R. R. Gutha, R. Sakidja, J. Z. Wu, *ACS Appl. Nano. Mater.* **2020**, *3*, 2354–2363.
- [21] T. T. B. Quyen, W. -N. Su, K. -J. Chen, C. -J. Pan, J. Rick, C. -C. Chang, B. -J. Hwang, *J. Raman Spectrosc.* **2013**, *44*, 1671–1677.
- [22] S. Shim, C. M. Stuart, R. A. Mathies, *ChemPhysChem* **2008**, *9*, 697–699.

- [23] P. H. C. Camargo, L. Au, M. Rycenga, W. Y. Li, Y. N. Xia, *Chem. Phys. Lett.* **2010**, *484*, 304–308.
- [24] C. Zhuang, Y. F. Xu, N. S. Xu, J. X. Wen, H. J. Chen, S. Z. Deng, *Sensors* **2018**, *18*, 3458.
- [25] P. Novak, C. Li, A. J. Shevchuk, R. Stepanyan, M. Caldwell, S. Hughes, T. G. Smart, J. Gorelik, V. P. Ostanin, M. J. Lab, G. W. J. Moss, G. I. Frolenkov, D. Klenerman, Y. E. Korchev, *Nat. Methods* **2009**, *6*, 279–281.
- [26] T. Li, X. L. He, K. L. Zhang, K. Wang, P. Yu, L. Q. Mao, *Chem. Sci.* **2016**, *7*, 6365–6368.
- [27] R. R. Pan, K. K. Hu, R. Jia, S. A. Rotenberg, D. C. Jiang, M. V. Mirkin, *J. Am. Chem. Soc.* **2020**, *142*, 5778–5784.
- [28] M. Simonis, A. Sandmeyer, J. Greiner, B. Kaltschmidt, T. Huser, S. Hennig, *Sci. Rep.* **2019**, *9*, 5480.
- [29] D. N. Ngo, V. T. T. X. Ho, G. Kim, M. S. Song, M. R. Kim, J. Choo, S. -W. Joo, S. Y. Lee, *Anal. Chem.* **2022**, *94*, 6463–6472.

# Chapter 5

## The Design of TERS-SICM Probes

5.1 Anchoring Plasmonic Nanostructures at the Pipette Apex .....	125
5.1.1 Synthesizing gold nanoparticles at the pipette end .....	125
5.1.2 Attaching as-prepared gold nanoparticles on nanopipette by a linker .....	129
5.2 Stability .....	133
5.3 Summary .....	135
References .....	135

TERS as a new technique with a very high spatial resolution for the study of interfacial phenomena has been introduced in detailed in Chapter 1. The majority of TERS technologies have been performed in ambient air or ultrahigh vacuum but only a few worked in liquid where they highlighted the difficulty to carry out TERS experiments due to the lack of stable plasmonic tips and the optical complexity of the liquid-air interface.<sup>[1-4]</sup> However, the possibility to utilise this powerful technique in relevant scientific and technological fields like electrochemistry and biology drives the efforts to investigate the measurement of TERS in liquids.<sup>[5]</sup> Towards this direction, the idea of using SICM as an alternative to AFM or STM for moving the probe in TERS seems an interesting approach since the SICM technique is a very suitable technique with nanometer resolution for studying biological and physical interfaces in liquids.<sup>[6-7]</sup>

A fundamental part of the development of SPM related techniques is the design and fabrication of probes. Particularly, the probes in the TERS technique must possess plasmonic properties at the very end of the sharp tips. In Figure 5.1, I present a schematic of a proposed setup for doing TERS in liquid with a specially modified double-barrel SICM nanopipette. In this case, one barrel is filled with electrolyte and therefore employed to precisely control the position of the nanopipette, the other barrel is modified with a plasmonic nanoparticle to serve as an LSPR element under the appropriate laser illumination.

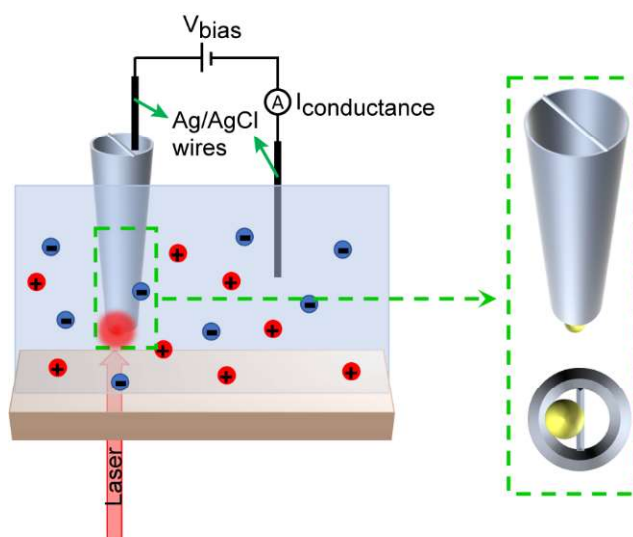


**Figure 5.1** Schematic illustrating the proposed design system for doing bottom illumination TERS in a SICM configuration.

In this chapter, different approaches have been considered to produce nanopipettes with plasmonic features at the tapered end to fulfill the requirements for applications in TERS and SICM techniques, the obtained nanopipettes are named TERS-SICM probes. Firstly, the direct growth of gold nanostructures at the end of nanopipette by the seed-mediated method was carried out. The second strategy is based on the method for pipette modification described in Chapter 4, using MPMS as the linker to decorate the pre-synthesized gold nanoparticles on a nanopipette. The advantages of this second approach are the fine control on the geometry and crystal quality of nanostructure which strongly influence the plasmonic property. Importantly, the mechanical stability of gold nanoparticle on the pipette end was challenged by carrying out SICM mapping with the obtained TERS-SICM probes. The TERS-SICM probe has the potential to apply to a broader range of applications, beyond TERS.

## **5.1 Anchoring Plasmonic Nanostructures at the Pipette Apex**

In this section, I will present two methods for decorating gold nanostructure at the end of one barrel to obtain TERS-SICM probes, which can be used to do TERS in liquid. The method to directly grow nanostructure at the nanopipette will be introduced in Section 5.1.1, and the other method that modifying as-prepared nanostructures with well-confined sizes and morphologies on the tip by a bifunctional molecule as linker will be described in Section 5.1.2.

### **5.1.1 Synthesizing gold nanoparticles at the pipette end**

Following seed-mediated methods for preparing gold nanostructures, the proposed procedure is to physically separate the components for preparing the growth solution into two parts, one part of the components was injected inside the pipette and subsequently immersed the nanopipette in the bath containing the other part of components. It is expected that the reaction occurs in the vicinity of the pipette end since the two parts of the components will gradually mix.<sup>[8-9]</sup>

To evaluate this strategy for TERS-SICM probe fabrication, attempts were carried out using the conditions of synthesizing gold nanobipyramid described in Chapter 2. I first considered adding the growth solution without reducing agent but mixed with a certain amount of seed solution into one of the barrels of a double-barrel pipette,

followed by immersing the nanopipette into a bath solution containing the reduction agent (0.1 M, AA) to trigger the reaction, as shown in Figure 5.2a. The nanopipette was kept in the AA solution at room temperature for five hours, then taken out and cleaned with deionized water. After leaving the pipette in the air overnight for drying, the resulting architectures were thoroughly examined by SEM imaging employing two different imaging modes, collecting secondary and back-scattered electrons to form images, respectively. Firstly, the SEM image of collecting secondary electrons from the side view shows that one barrel of the nanopipette possesses gold nanoparticle (Figure 5.1b). The further characterization was performed by collecting the back-scattered electrons during SEM imaging, which clearly exhibited that one barrel of the probe is empty and the other barrel is with gold particle (Figure 5.2c, the brightest part is gold particle due to the larger atomic number of gold atom). The top view SEM image of the obtained TERS-SICM probe (Figure 5.1d) also illustrates that gold nanostructure was formed in one barrel of the nanopipette while the other barrel is empty, which is very important for SICM application. The procedure was tested on larger double-barrel pipettes as well. In this case, the gold deposit is formed at the end of the pipette but as an aggregate of particles (Figure 5.2e and f).

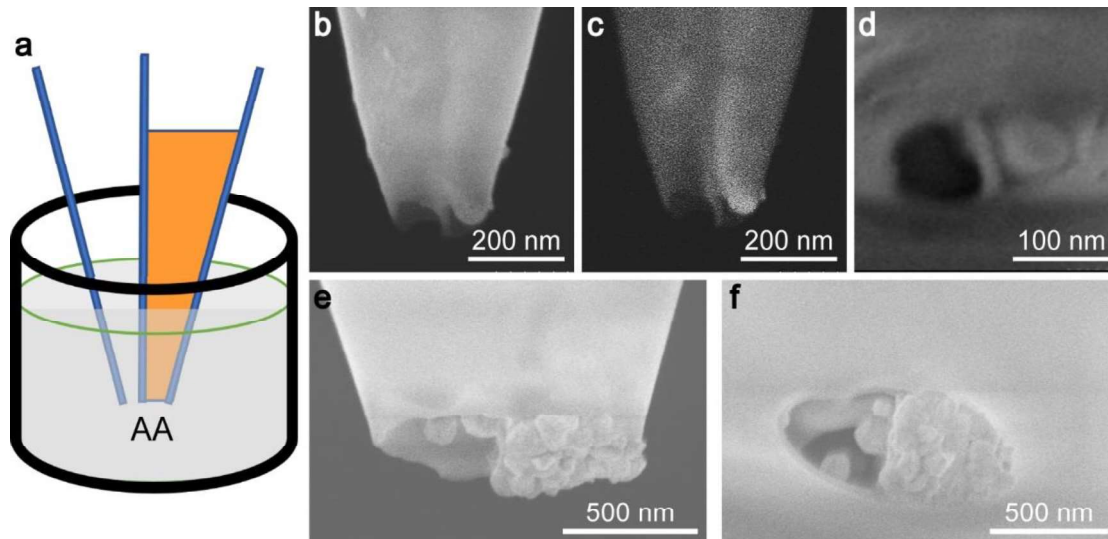


**Figure 5.2** The preparation schematic and SEM images of TERS-SICM probes via *in-situ* synthesis at nanopipette apex. (a) Schematic of preparing gold nanostructure at the end of one barrel of a nanopipette. The orange colour inside of the nanopipette represents the growth solution without AA but mixed with a certain number of seeds. (b–d) The SEM images of obtained nanopipette with gold nanostructure from side view and top view, c is obtained by collecting the back-scattered electrons. (e–f) The

*SEM images of obtained nanopipette with gold nanostructures, the size of the nanopipette is large.*

Despite the simplicity of the procedure, there is an important lack of control over the deposition location of gold nanoparticles along the pipette length, which is fundamental for TERS applications. As exemplified with SEM images in Figure 5.3, some gold nanoparticle depositions could be observed, however, those are formed inside the barrel and the distances between the depositions and the end of the pipettes are random. The pipettes obtained were unsuitable for our final goal, since the gold depositions are not exposed at the end of the nanopipettes, resulting in any TERS measurements being unfeasible. Several factors can be responsible for these variations in the position of gold nanoparticle deposition, such as concentration gradients inside the pipette, potential air bubbles or gaps when filling the pipette, diffusion of the AA solution into the pipette, just to name a few. All the above-mentioned factors are very hard to control. For example, attempts for improving the possibility of the growth from the pipette end were performed by leaving the filled pipettes vertically in the air for a period of time before immersing them into AA solution to ensure the growth solution inside the pipette reach the end of the pipette. However, the reproducibility of the results was still low.

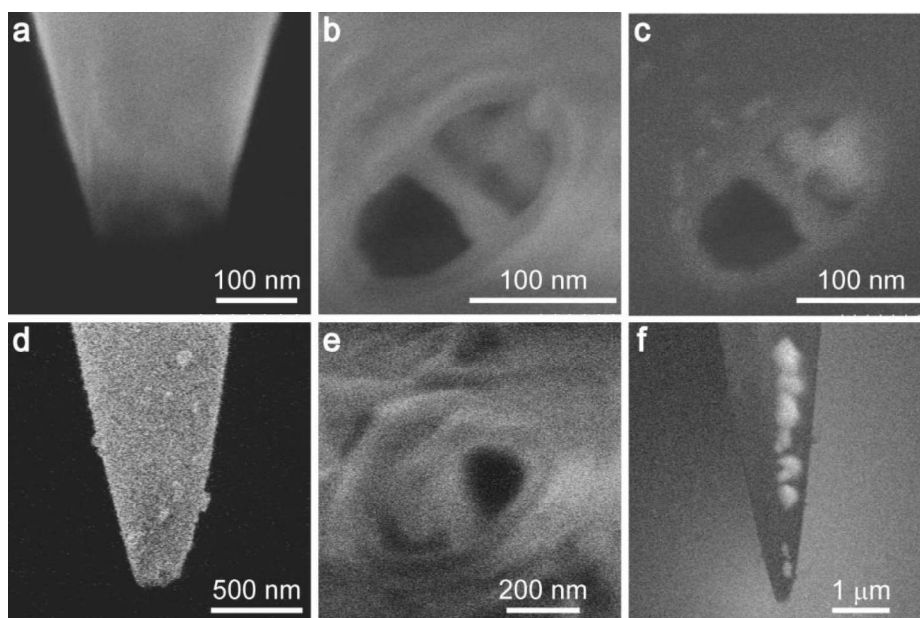


**Figure 5.3** SEM images of the obtained nanopipettes with gold nanostructures, which were prepared through injecting the mixture of seed solution and growth solution without AA into one barrel of the pipette and then immersing the pipette into AA

solution. *a–c* corresponds to one pipette and *d–f* corresponds to the other pipette. *c* and *f* are obtained by collecting the back-scattered electrons to highlight the gold depositions.

The effect of switching the components was also assessed, backfilling AA solution into the nanopipette and subsequently putting the pipette with AA solution into the mixture of growth solution and seed solution. In this case, the ease of the reducing agent to diffuse within the bath solution as well as the larger amount of gold precursor can facilitate the formation of large gold deposits in the vicinity of the pipette aperture, in a very uncontrollable manner. In Figure 5.4, a few SEM images of the obtained pipettes are presented to exemplify the large irregular gold structure formed at the end blocking the barrels. The reason for obtaining various morphologies is probably related to the reduction rate of gold precursors and the concentration gradients of reagents existing in this synthesis, that are strongly dependent on the diffusion rate. In the general bulk synthesis, well-defined morphologies can be obtained as the concentration of reagents are well controlled by mixing the solution thoroughly.<sup>[10]</sup>

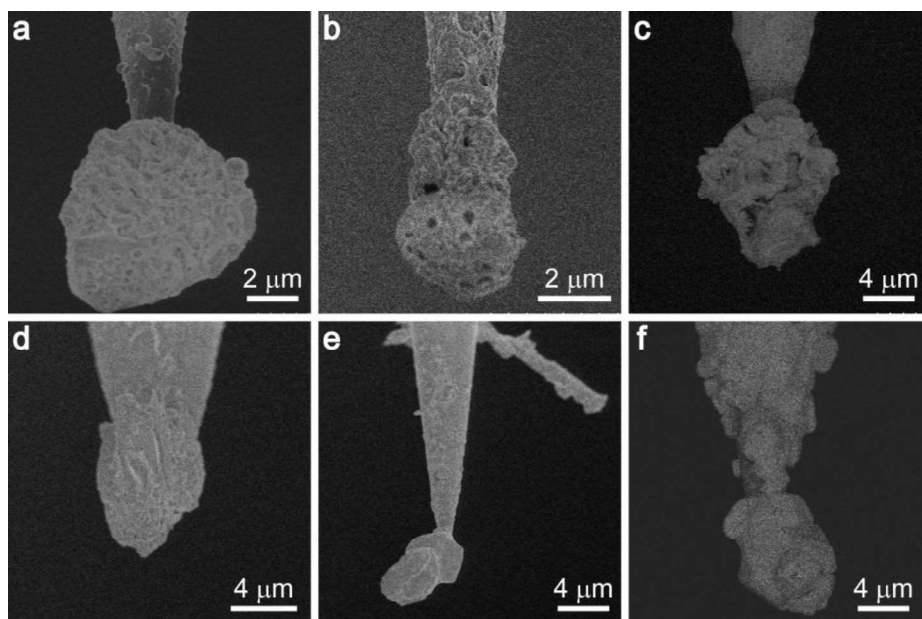


**Figure 5.4** SEM images of obtained nanopipettes with gold structures, which were prepared via injecting AA into one barrel of the pipette and then immersing the pipette into the mixture of seed solution and growth solution without AA. The method for obtained these pipettes were the same.

### 5.1.2 Attaching as-prepared gold nanoparticles on nanopipette by a linker

The advantages of being able to attach an externally synthesized nanoparticle at the end of a pipette are numerous<sup>[11-12]</sup>: a broad variety of synthetic methods to obtain nanoparticles with high control on shape and size, as seen in previous chapters; high crystal quality; easy tunability of plasmonic properties based on size; broad range of materials, etc.

Based on the developed method for decorating the outer surface of glass nanopipettes (borosilicate and quartz) with gold nanoparticles described in Chapter 4, I have assessed the use of bifunctional molecules as linkers to attach gold nanostructures at the end of the pipette. The method proposed is similar as the one used in Chapter 4, starting with a treatment of the quartz capillaries (double barrel) with freshly prepared piranha solution for 2 h at room temperature, followed by a thoroughly rinse with deionized water and isopropanol, and finally dried at 80 °C oven. After pulling the capillaries to nanopipettes with the desired dimension, the nanopipettes were immersed into a 1% (v/v) MPMS solution in ethanol for 20 min at room temperature while blowing the pipettes with airflow (~6 bars). The presence of the airflow can avoid the blockage of the pipette aperture and the modification of the inner wall (see Chapter 4, Section 4.1.1). Then the nanopipettes were cleaned by ethanol and let dry at room temperature. At this point, the last step was immersing these nanopipettes modified with thiol groups into gold nanoparticle colloids without airflow through the pipettes, which is beneficial to the attachment of the gold nanoparticles at the end of the pipette apertures.

For the first assessment, gold nanospheres were chosen due to their isotropic property, which simplifies the decoration of nanopipette aperture. Indeed, for this procedure, it is fundamental that the nanopipette aperture and nanostructure possess similar sizes for achieving a single nanoparticle attachment through a complete and robust blockage of the pore. Since the diameter of the double-barrel quartz nanopipette pulled by the program mentioned in Chapter 2 is around 170 nm, the diameter of the nanosphere has been selected to be slightly smaller than the size of one barrel, to ensure one single gold nanoparticle anchors at the end of one barrel without much protrusion and does not diffuse inside the pipette. Therefore, gold nanospheres with sizes around 70 nm and the plasmonic peak located at 544 nm were synthesized (Figure 5.5a and b for extinction spectrum and SEM images of the

sample). Once confirmed the right combination of dimensions, the modification of the pipette with a single nanosphere was achieved by following the above-described procedure. The SEM imaging (Figure 5.5c and d) confirmed the attachment of one single gold nanosphere at one barrel of a double-barrel pipette, while keeping the second barrel open and clean. Furthermore, the particle is only partially protruding, fulfilling the SICM technique requirements that one-diameter distance of tip-sample clearance.<sup>[13]</sup>

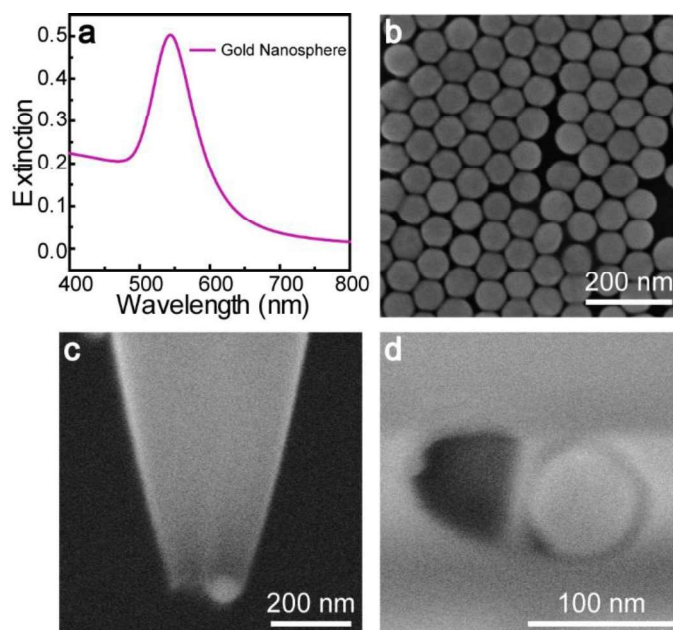


**Figure 5.5** The representative TERS-SICM probe obtained using MPMS molecules as linkers. (a–b) The extinction spectrum and SEM image of gold nanospheres. (c–d) SEM images of obtained plasmonic nanopipette from side view and top view.

Selecting the right ratio between nanoparticle size and nanopipette aperture dimension is key for the quality of the TERS-SICM probe, this has been demonstrated by extending the procedure to other gold nanostructures, such as gold trisectahedron, gold nanorod, and gold nanobipyramid. Among them, gold trisectahedron is an especially interesting structure for the preparation of TERS-SICM probes, as its high symmetry can avoid the requirement of forcing the particle attachment to the preferential direction. Moreover, its significant number of sharp tips will confer to the TERS-SICM probe a higher plasmonic performance<sup>[14]</sup> and higher spatial resolution.<sup>[15]</sup> The nanostructures like gold nanorod and gold nanobipyramid generally possess two plasmonic peaks, respectively, including a longitudinal mode and a transverse mode, with the advantage of the longitudinal plasmonic peak can be tuned

from visible to near infrared region. Therefore, the successful achievement of immobilizing different types of gold nanostructures at the end of one barrel can largely broaden their application.

Following the same procedure as above-described, TERS-SICM probes with other nanostructures were prepared, the employed nanostructures include gold trisoctahedrons and gold nanorods shown in Figure 4.8 and Figure 4.5 (Au NR 2) in Chapter 4, as well as gold nanobipyramids with the longitudinal plasmonic wavelength positioned at 764 nm and the size is approximately 70 nm by 30 nm presented in Figure 5.6. SEM imaging of the resulting nanopipettes illustrated that one barrel of one pipette is with gold nanostructures and the other barrel is open for the applications with SICM technique (Figure 5.7), which demonstrates that this procedure is applicable to many types of nanostructures for preparing TERS-SICM probes. Additionally, the images show that the probes with gold trisoctahedron or gold nanorod only possess one single gold nanoparticle at the end while the probe with nanobipyramids has several particles at the end. These results serve to emphasize again the importance in the size of nanoparticle and pipette aperture. In order to anchor only one nanorod or nanobipyramid at the end of one barrel, it is better to use the pipette whose size is comparable with the transverse size of nanoparticle.

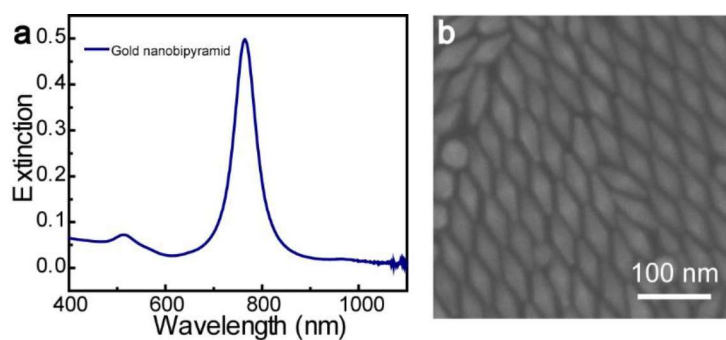


**Figure 5.6** The extinction spectrum (a) and SEM image (b) of gold nanobipyramids.

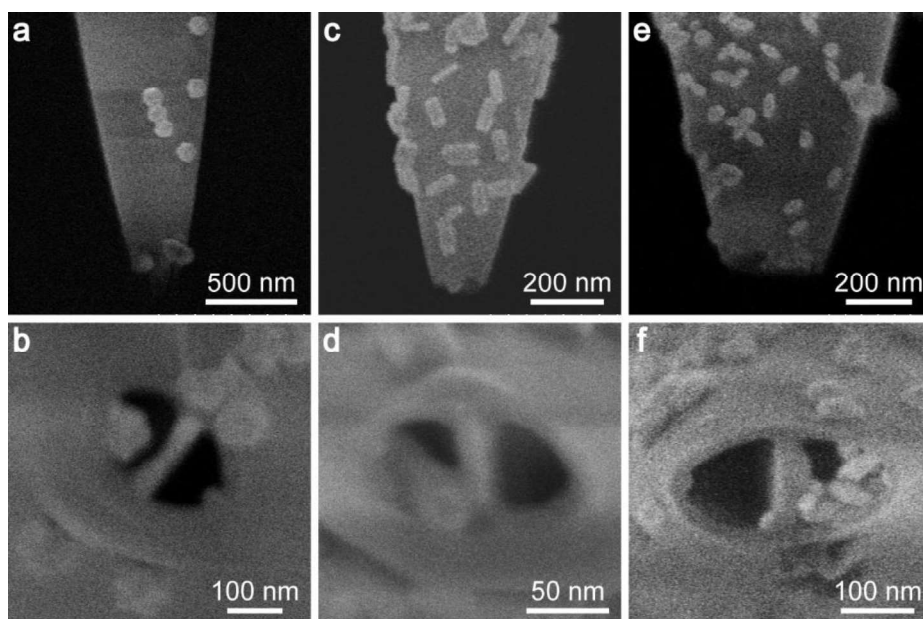


**Figure 5.7** SEM images of obtained TERS-SICM probes with varying gold nanostructures. Gold trisoctahedrons (a–b), gold nanorods (c–d), and gold nanobipyramids (e–f) from side view (top row) and top view (bottom row).

For the anisotropic nanostructures, it is hard to control the orientation of the nanostructure at the end of the barrel. Taking gold nanorod as an example, it can be not only anchored almost vertical to the diameter of the tip, shown in Figure 5.7c–d, but also placed horizontal with the tip end, as shown in Figure 5.8a, or randomly oriented as shown in Figure 5.8b. Controlling the orientation of the nanostructure is difficult but has a significant impact on the LSPR operation properties and spatial resolution of the probe. Additionally, since the two barrels of the nanopipette are same, it is possible to obtain nanopipette with both of the barrels blocked by gold nanoparticles (Figure 5.8c–f).

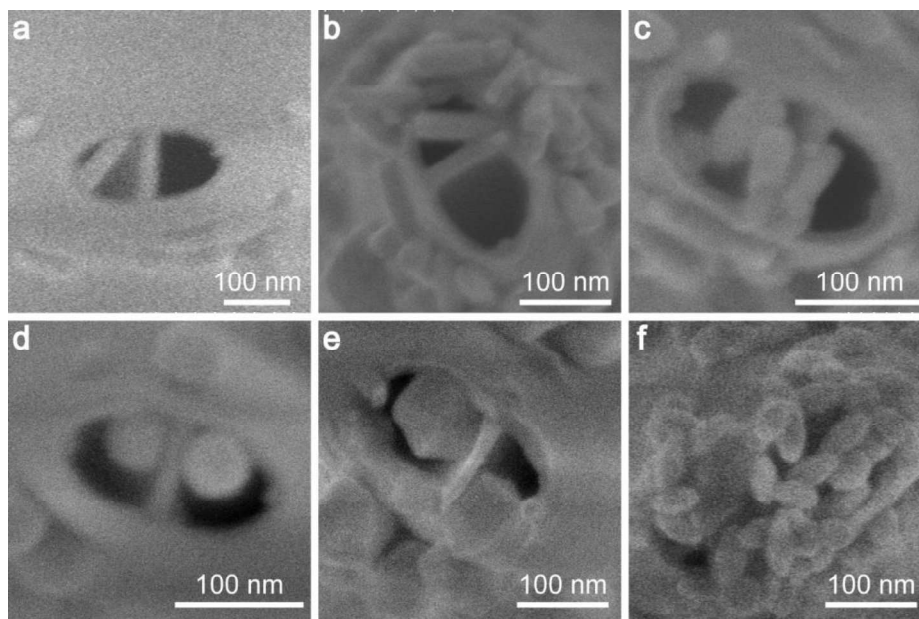


**Figure 5.8** SEM images of TERS-SICM probes with nanoparticles at random positions, obtained using bifunctional molecules as linkers to fix prepared nanoparticles. (a–c) The SEM images of nanopipette with gold nanorods from top view. (d–f) The SEM images of nanopipettes with gold nanospheres, gold trisoctahedrons, and gold nanobipyramids, respectively.

## 5.2 Stability

It is essential to ensure the modified probe with attached nanoparticle is mechanically robust enough to guarantee its ultimate application. As the nanopipette keeps oscillating during the process of the SICM imaging in AC scanning mode, applying the obtained TERS-SICM probe in SICM imaging is a suitable way to evaluate the anchoring stability of gold nanoparticle. Hence, a TERS-SICM probe was employed in SICM mapping of a silicon oxide surface to confirm the anchoring stability of the nanoparticle can withstand the imaging conditions. In this case, the probe with several gold nanospheres at the end of one barrel and one gold nanosphere located in the other barrel was chosen, shown in Figure 5.9a and b. Furthermore, the imaging conditions were selected as mechanically challenging: surface tracking at constant distance mode and employing AC z-modulation as feedback control (more details of this scanning conditions are given in Chapter 2). The area of  $10\ \mu\text{m} \times 5\ \mu\text{m}$  was raster scanned with a lateral scanning rate of  $0.5\ \mu\text{m}/\text{s}$  for collecting 32 lines of the whole map and 64 points per line. The resulting SICM image is presented in Figure 5.9c as topographic map of  $64 \times 32$  pixels. Just after SICM imaging, the probe

was carefully removed from the SICM setup, cleaned in deionized water and left in the air overnight for drying. Further SEM imaging was carried out on the TERS-SICM probe to check whether the gold nanoparticles are still maintained on the pipette or not (Figure 5.9d–e). Compared with the previous images, most of the nanoparticles remained, except for two nanospheres (marked with red arrows 1 and 2 in Figure 5.9b) located on top of the ensemble and a third one (marked with a red arrow 3 in Figure 5.9b) located at the interior of the other barrel employed for controlling the probe position. The two particles labelled 1 and 2 were detached because the gold nanospheres did not contact with any linker group on the surface of the nanopipette, thus, there is no strong bond to fix the two nanospheres. The detachment of the particle with label 3 is because of the weak adhesion of the particle to the pipette inner surface (no modification with thiol group is present), which resulted detaching either due to the mechanical vibration of the AC mode or due to the presence of an electrical bias.<sup>[16]</sup> Moreover, being able to successfully obtain an SICM image also confirms that the barrel for controlling probe position is clean and can be used in the applications with SICM technique. We therefore confirmed that using MPMS as a linker can firmly fix gold nanostructures on the quartz nanopipettes and those probes can potentially be suitable for TERS-SICM.

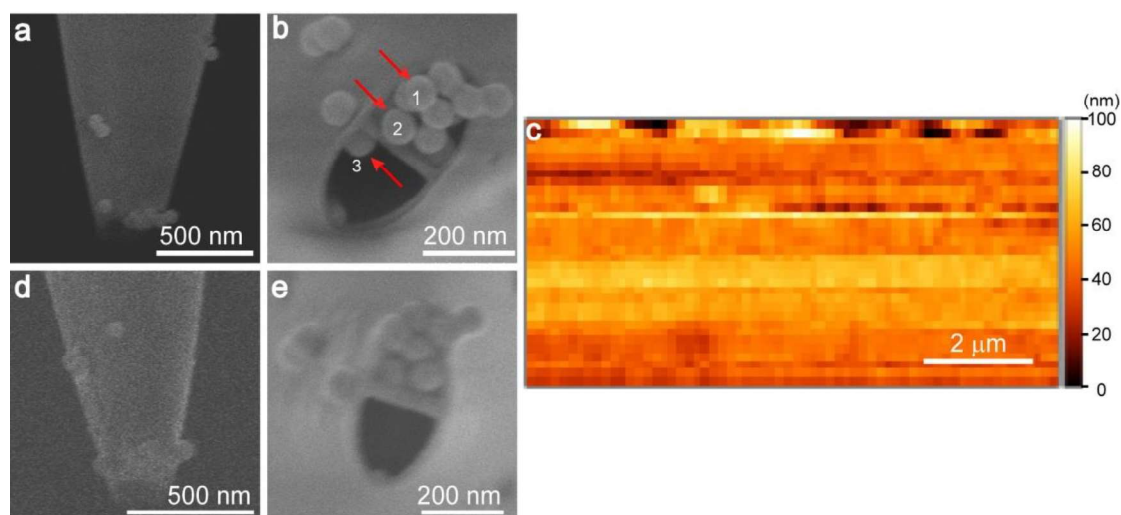


**Figure 5.9** SICM imaging using TERS-SICM probe. (a–b) SEM images of nanopipette attached with gold nanospheres using MPMS as a linker from side and top view. (c) Topography image of a relatively flat surface recorded by SICM setup with AC mode. (d–e) SEM images of the nanopipette after doing SICM corresponding in a and b.

### 5.3 Summary

In this chapter, I have presented the design of TERS-SICM probes, a double-barrel pipette with one of the barrels decorated with a metal structure that fulfils the requirements for carrying out TERS and the other barrel is empty for the combination with SICM technique. Two strategies for preparing the TERS-SICM probes were presented in this chapter. The first approach is to directly grow the gold nanostructure by in-situ reducing gold precursor on the pipette based on the seed-mediated method for synthesizing gold nanoparticles. Although the expected TERS-SICM probes could be obtained through this method, it is hard to control the size and morphology of the gold nanostructure on the pipette. The second strategy, based on the attachment of the off-situ prepared gold nanoparticles, has the advantage of a well-defined morphology and size of the particle. The mechanical stability of the gold nanostructures on the pipette was tested by doing SICM mapping with AC scanning mode, proving the robust anchor of gold nanostructures and the suitability of the probe as a SICM scanning probe. The main drawback of the method is the lack of control in the attachment at only one barrel, as this occurs randomly. The yield of the plasmonic nanopipette with only one barrel fixed gold nanostructures is very low, being more likely to have both of the two barrels blocked. To improve the success rate of the method, it can be interesting to track the attachment (and therefore blocking) of the two barrels by inserting electrodes, as doing in SICM. An abrupt change in conductance current would indicate the blockage of one of the pipette barrels,<sup>[16]</sup> and then retracting the pipette from the colloidal solution. Therefore, the method is promising yet needs to improve.

### References

- [1] N. M. Sabanes, L. Driessen, K. F. Domke, *Anal. Chem.* **2016**, *88*, 7108–7114.
- [2] N. Kumar, W. Su, M. Vesely, B. M. Weckhuysen, A. J. Pollard, A. J. Wain, *Nanoscale*, **2018**, *10*, 1815–1824.
- [3] T. Touzalin, A. L. Dauphin, S. Joiret, I. T. Lucas, E. Maisonhaute, *Phys. Chem. Chem. Phys.* **2016**, *18*, 15510–15513.
- [4] N. Kumar, C. S. Wondergem, A. J. Wain, B. M. Weckhuysen, *J. Phys. Chem. Lett.* **2019**, *10*, 1669–1675.

- [5] T. Schmid, B. -S. Yeo, G. Leong, J. Stadler, R. Zenobi, *J. Raman Spectrosc.* **2009**, *40*, 1392–1399.
- [6] C. -C. Chen, Y. Zhou, L. A. Baker, *Annu. Rev. Anal. Chem.* **2012**, *5*, 207–228.
- [7] C. Zhu, K. Huang, N. P. Siepser, L. A. Baker, *Chem. Rev.* **2021**, *121*, 11726–11768.
- [8] J. -M. Yang, L. Jin, Z. -Q. Pan, Y. Zhou, H. -L. Liu, L. -N. Ji, X. -H. Xia, K. Wang, *Anal. Chem.* **2019**, *91*, 6275–6280.
- [9] R. Gao, Y. -L. Ying, Y. -J. Li, Y. -X. Hu, R. -J. Yu, Y. Lin, Y. -T. Long, *Angew. Chem. Int. Ed.* **2018**, *57*, 1011–1013.
- [10] M. R. Langille, M. L. Personick, J. Zhang, C. A. Mirkin, *J. Am. Chem. Soc.* **2012**, *134*, 14542–14554.
- [11] J. Cao, H. -L. Liu, J. -M. Yang, Z. -Q. Li, D. -R. Yang, L. -N. Ji, K. Wang, X. -H. Xia, *ACS Sens.* **2020**, *5*, 2198–2204.
- [12] T. Quast, S. Varhade, S. Saddeler, Y. -T. Chen, C. Andronescu, S. Schulz, W. Schuhmann, *Angew. Chem. Int. Ed.* **2021**, *60*, 23444–23450.
- [13] C. -C. Chen, Y. Zhou, L. A. Baker, *Annu. Rev. Anal. Chem.* **2012**, *5*, 207–228.
- [14] D. Huo, H. M. Ding, S. Zhou, J. Li, J. Tao, Y. Q. Ma, Y. N. Xia, *Nanoscale* **2018**, *10*, 11034–11042
- [15] T. Deckert-Gaudig, A. Taguchi, S. Kawata, V. Deckert, *Chem. Soc. Rev.* **2017**, *46*, 4077–4110.
- [16] T. Li, X. L. He, K. L. Zhang, K. Wang, P. Yu, L. Q. Mao, *Chem. Sci.* **2016**, *7*, 6365–6368.

# Chapter 6

## Conclusion and Outlook

In this thesis, I have described my works on plasmonic nanostructures, including the synthesis of gold trisoctahedrons by a facile and fast seed-mediated method, the preparation of SERS-SICM probes by decorating gold nanostructures on the surface of a glass pipette, and the preparation of TERS-SICM probes by fixing a single gold nanoparticle at the end of a double-barrel glass pipette.

Gold nanocrystals with intriguing LSPR properties have already been widely applied in many areas including chemical/biochemical sensing, spectroscopy, nanomedicine, solar energy harvesting, photocatalysis. Since the LSPR properties are highly dependent on sizes, shapes and compositions, it is of great importance to develop methods to prepare colloid gold nanostructures with special morphologies in high uniformity and high purity. Towards this goal, I have successfully explored a facile and fast seed-mediated method to obtain gold trisoctahedrons. The seed solution can be used after finishing preparation without stabilization time and it only takes 7 min for the growth of gold trisoctahedrons from seeds. The size of gold trisoctahedrons can be deliberately tailored from 39 nm to 268 nm. As a result, the dominant plasmon resonance wavelength can be precisely and synthetically varied from 533 nm to 923 nm, which broadens the applications. In addition, the Miller indices of the facets can also be varied, ranging from {441} to the limit case {110}, by increasing the growth temperature. Interestingly, gold trisoctahedron composed of 24 high-index facets, 24 edges, and 14 sharp tips exhibits great plasmonic performance which brings up an opportunity to act as an excellent structure for broadening the applications of gold nanostructures. I have therefore investigated their plasmonic sensitivities and SERS performances, showing that they possess higher plasmonic sensitivities and higher *FOM* values than those of gold nanospheres as well as the detectable particle concentration can be lower to  $3.63 \times 10^8$  NP mL<sup>-1</sup> in SERS measurements.

The potential of SERS as an analytical technique has been demonstrated over the years. In order to expand the scope of its applications, researchers attempted to combine the SERS technique with a number of other techniques, especially with scanning probe microscopies like SICM. The combination of SERS and SICM paves the way to in-situ biological investigations in cells. In my work, I have described a simple yet successful strategy to decorate the outer surface of glass nanopipettes (key component of the SICM technique) with gold nanostructures like gold nanorods, gold nanospheres, gold trisoctahedrons, and gold nanobipyramids employing bifunctional molecules (MPMS) as linkers. The obtained probes are named SERS-SICM probes. The diverse applications of SICM mainly lie in the variety of nanopipettes, thus I demonstrated the suitability of the method on different kinds of nanopipettes, single-barrel borosilicate nanopipettes and double-barrel quartz nanopipettes. Notably, the successfully obtained SERS-SICM probes always maintain the pipette apertures open, which is fundamental in controlling the position of the pipette in SICM technique. The plasmonic properties of obtained SERS-SICM probes were confirmed by measuring the Raman spectra of three types of molecules (R6G, 4-MBT, and 2-NaT) using Raman spectroscopy. Moreover, the suitability and fixation stability of the nanoparticles were proved by performing SICM imaging and the insertion of the pipette into living cells. All the results showed that the obtained plasmonic nanopipettes have the potential to be applied in the challenging field of investigating living cells.

Broadening the applicability of anchoring nanostructures on nanopipettes, I proposed a procedure for obtaining TERS-SICM probes, a nanopipette with one single gold nanostructure at the apex for performing TERS in liquids. In the designed probe, the employed nanopipette possesses two barrels, one barrel is empty which can be used to control the pipette position while the other barrel is attached a single nanoparticle that can provide plasmonic property for TERS measurements. In my experiments, I proposed two different methods to prepare this design structure, one is to in-situ synthesize nanoparticles on the pipette apex and the other one is to attach already synthesized nanoparticles. Although I successfully obtained the desired TERS-SICM probes employing both methods, I encountered difficulties mainly with the reproducibility and success rate. The first way is difficult to control the position, size and morphology of the gold nanostructures in the barrel. The second method provides high control on the size and morphology of gold nanostructure at the end of

the barrel, which is very important for applications. Additionally, the anchoring stability of the gold nanostructure at the end of the barrel was assessed by scanning a surface in SICM mode with an obtained TERS-SICM probe. The excellent results show that the designed probe will become a promising new system for the future development of measuring TERS in liquids.

I believe that the research work described in this thesis will contribute to the development of the rational design and various applications of gold nanoparticles. In my first work, the method I developed in the synthesis of gold trisoctahedron can be the starting point to explore fast and facile methods to obtain other nanostructures, for example, nanorods. Indeed, the size or the aspect ratio of gold nanorods is limited in a certain value, despite some recent works on regrowth methods, it is still challenging to obtain large gold nanorods or gold nanorods with high aspect ratio. In my work, I observed large gold nanorods when I used CTAB as surfactants in the growth solution. Based on this result, I believe that the purely large gold nanorods can be successfully obtained in a fast and facile method by slightly changing the synthesizing conditions. Since the preparing method is a seed-mediated method, the size and aspect ratio could be easily changed by tuning the amount of seed solution in the growth solution.

On the other hand, my research work on the fabrication of plasmonic scanning probes are setting the path towards the coupling of Raman spectroscopy with pipette-based scanning probe microscopies, such as SICM based SERS-SICM and TERS-SICM. I believe there are still many efforts needed to further investigate the preparation of plasmonic nanostructures, increase preparation success rate for a broaden application and even commercialization. Promisingly, the outstanding results obtained on SERS performances, the robust anchor, and the ability to penetrate living cells point towards the potential application for analyzing living cells by combing Raman spectroscopy with SICM technique, for example, using this plasmonic nanopipette to measure the level of oxygen in hypoxic single cell.

The above-mentioned aspects are some highly intriguing examples for further investigations and applications. Even though there will be lots of difficulties and challenges during the process of carrying out experiments, I am strongly convinced that the difficulties and challenges can be overcome. I optimistically expect that the new techniques, combing SICM with Raman spectroscopy, can be applied in the real-world, not only in the lab.

# Résumé de la thèse

Dans ce manuscrit de thèse, j'ai décrit mes travaux sur les nanostructures plasmoniques, notamment la synthèse de trisoctaèdres d'or par une méthode simple et rapide à base de précurseurs, la fabrication de sondes SERS-SICM en recouvrant de nanostructures d'or la surface d'une pipette en verre, ainsi que la fabrication de sondes TERS-SICM en fixant une nanoparticule d'or unique au bout d'une pipette en verre à double fût.

Les nanocristaux d'or aux propriétés LSPR prometteuses ont déjà été largement utilisés dans de nombreux domaines, tels que la détection chimique ou biochimique, la spectroscopie, la nanomédecine, la conversion de l'énergie solaire et la photocatalyse. Leurs propriétés dépendant fortement de leurs tailles, formes et compositions, il est donc hautement important de développer des méthodes de fabrication de nanostructures d'or colloïdales avec des morphologies particulières possédant une grande uniformité et pureté. Dans ce but, j'ai exploré avec succès un procédé simple et rapide à base de précurseurs pour préparer des trisoctaèdres d'or. La solution de précurseurs peut être utilisée après avoir terminé sa préparation sans délai de stabilisation ; cela ne prend que 7 min pour la croissance de trisoctaèdres d'or à partir des précurseurs. La taille des trisoctaèdres d'or peut être variée intentionnellement de 39 nm à 268 nm en contrôlant la quantité des précurseurs dans la solution de croissance. En conséquence, la longueur d'onde dominante de la résonance plasmonique peut être modifiée de manière précise et synthétique de 533 nm à 923 nm, ce qui élargit le domaine des applications. De plus, les indices de Miller des facettes peuvent également être variés, en augmentant la température de croissance, de {441} jusqu'au cas limite {110}. Fait intéressant, les trisoctaèdres d'or composés de 24 facettes, de 24 arêtes et de 14 pointes acérées présentent de performances plasmoniques remarquables, ce qui offre la possibilité d'élargir le domaine d'applications des nanostructures d'or. J'ai donc étudié leurs sensibilités plasmoniques et leurs performances SERS, en montrant qu'ils possèdent des sensibilités plasmoniques et des valeurs de FOM plus élevées que celles des nanosphères d'or. De surcroît, la concentration de particules détectables peut être inférieure à  $3.63 \times 10^8 \text{ NP.ml}^{-1}$  dans les mesures SERS.

Le potentiel du SERS en tant que technique analytique a été démontré au fil des années. Afin d'étendre son application, les chercheurs ont essayé de combiner la technique SERS avec de nombreuses autres techniques, en particulier avec les microscopies à sonde à balayage telles que la SICM. La combinaison du SERS et de la SICM ouvre la voie à des études biologiques in situ dans les cellules. Dans mon manuscrit, j'ai décrit une stratégie à la fois simple et opérationnelle pour recouvrir la surface externe de nanopipettes de verre (composants clés de la technique SICM) avec des nanostructures en or telles que des nanotiges, des nanosphères, des trisoctaèdres et des nanobipyramides, en utilisant des molécules bifonctionnelles (MPMS) comme liant. Les sondes ainsi fabriquées sont nommées sondes SERS-SICM. Les diverses applications de la SICM résultent principalement de la grande variété de nanopipettes. Ainsi, j'ai démontré l'adéquation de cette approche sur différentes nanopipettes : des nanopipettes en borosilicate à fût unique et des nanopipettes en quartz à double fût. En particulier, les sondes SERS-SICM ainsi fabriquées ont toujours les ouvertures de leurs pipettes dégagées, ce qui est fondamental pour le contrôle de la position de la pipette par la technique SICM. Les propriétés plasmoniques des sondes SERS-SICM ont été confirmées en mesurant les spectres de trois types de molécules (R6G, 4-MBT et 2-NaT) par la spectroscopie Raman. De plus, l'adéquation des sondes et la stabilité de fixation des nanoparticules ont été démontrées en effectuant de l'imagerie SICM, ainsi que par l'insertion de la pipette dans des cellules vivantes. Tous les résultats ont montré que les sondes SERS-SICM fabriquées ont le potentiel d'être appliquées dans le domaine exigeant de l'étude de cellules vivantes.

En élargissant l'applicabilité de l'ancrage de nanostructures sur les nanopipettes, j'ai proposé une procédure pour la fabrication d'une sonde TERS-SICM, c.-à-d. une nanopipette avec une seule nanostructure en or à sa pointe, afin de pratiquer le TERS dans les liquides. Dans la sonde ainsi conçue, la nanopipette utilisée possède deux fûts. L'un des fûts, vide, est utilisé pour contrôler la position de la pipette alors que sur l'autre fût est attachée une nanoparticule unique qui fournit la capacité plasmonique nécessaire pour les mesures TERS. Dans mes expériences, j'ai proposé deux méthodes différentes pour obtenir cette structure ; une utilisant la synthèse in situ de nanoparticules sur la pointe de la pipette et une autre, basée sur la fixation locale de nanoparticules déjà synthétisées. Bien que j'aie réussi à fabriquer des sondes TERS-SICM en utilisant les deux méthodes, j'ai rencontré des difficultés principalement au niveau de la reproductibilité et du taux de réussite. Avec la première méthode, il est

difficile de contrôler la position, la taille et la morphologie des nanostructures en or dans le fût. La deuxième méthode permet un contrôle accru de la taille et de la morphologie de la nanostructure à l'extrémité du fût, ce qui est très important. De plus, la stabilité d'ancrage de la nanostructure en or à l'extrémité du fût a été évaluée en cartographiant une surface en mode SICM avec une sonde TERS-SICM fabriquée. Les excellents résultats montrent que la sonde ainsi conçue deviendra un nouvel élément clé prometteur dans le développement actuel du TERS dans les liquides.

J'ose espérer que mes travaux de recherche décrits dans ce manuscrit de thèse contribueront au développement de la conception rationnelle de sondes TERS-SICM, de même qu'à celui des diverses applications des nanoparticules en or. Je m'attends avec optimisme à ce que la nouvelle technique du TERS-SICM, combinant la SICM avec la spectroscopie Raman, puisse être appliquée non seulement dans des recherches en laboratoire mais également dans des applications de la vie réelle.

**Titre :** Nanostructures Plasmoniques pour des Applications de la Spectroscopie Raman à Exaltation.

**Mots clés :** Nanostructures d'or, nanopipette, microscopie à conductance ionique, spectroscopie Raman

**Résumé :** Les nanostructures d'or ont attiré une attention considérable au cours des dernières décennies en raison de leurs propriétés exceptionnelles résultant des résonances plasmoniques de surface localisées, que sont les modes d'oscillation cohérente d'électrons libres confinés dans des nanostructures. Ces propriétés extraordinaires sont fortement corrélées à la taille, à la morphologie et à la composition des nanostructures, ainsi qu'à la fonction diélectrique du milieu qui les entoure, ce qui permet aux nanocristaux d'or d'être appliqués dans un large éventail de domaines tels que la détection plasmonique et la spectroscopie Raman.

Cette thèse est un effort pour le

développement des investigations et des applications des nanostructures d'or. Tout d'abord, une méthode facile et rapide à médiation par graine a été développée pour synthétiser des trisoctaèdres d'or qui présentent d'excellentes performances plasmoniques. Deuxièmement, la préparation de sondes SERS-SICM en décorant des nanostructures d'or à la surface d'une pipette en verre ouvre la voie à des investigations biologiques in-situ dans les cellules. De plus, les sondes TERS-SICM ont été conçues en fixant une seule nanoparticule d'or à l'extrémité d'une pipette en verre à double corps, qui a le potentiel d'effectuer la spectroscopie Raman exaltée à pointe dans un liquide.

**Title :** Plasmonic Nanostructures for Enhanced Raman Spectroscopy Applications.

**Keywords :** Gold nanostructures, nanopipette, scanning ion conductance microscopy, Raman spectroscopy

**Abstract :** Gold nanostructures have drawn considerable attention in recent decades due to their outstanding properties arising from the localized surface plasmonic resonances, which are the coherent oscillations of free electrons confined in nanostructures. These extraordinary properties are strongly correlated with the size, morphology, and composition of the nanostructures as well as the dielectric function of the medium surrounding them, which enables gold nanocrystals to be applied in a wide range of fields, such as plasmonic sensing and Raman spectroscopy.

This thesis is an effort to the development of the investigations and applications of gold

nanostructures. Firstly, a facile and fast seed-mediated method was developed to synthesize gold trisoctahedrons which exhibit excellent plasmonic performance. Secondly, the preparation of SERS-SICM probes by decorating gold nanostructures on the surface of a glass pipette paves the way to in-situ biological investigations in cells. Moreover, the TERS-SICM probes were designed by fixing a single gold nanoparticle at the end of a double-barrel glass pipette, which has the potential to perform tip-enhanced Raman spectroscopy in liquid.